Doctoral Thesis
博士論文

Implicit large-eddy simulations of low-Reynolds-number transitional flows using a high-order flux reconstruction approach

高次精度流束再構築法を用いた低レイノルズ数遷移流れの陰的ラージ・エディ・シミュレーションに関する研究

国立大学法人　横浜国立大学大学院
環境情報学府

Vilem Skarolek
スカロレク　ヴィレム

March, 2016

Abstract

The present work aims to obtain a greater insight into the performance and capabilities of the method developed with a high-order flux reconstruction approach for an implicit large-eddy simulation of transitional flows at low Reynolds numbers. The flux reconstruction scheme is examined with regard to feasibility, efficiency, and accuracy on two test cases, the Taylor–Green vortex problem and transitional flow over a wing SD7003, which were posed in the First and Second International Workshops on the high-order computational fluid dynamics method held in 2012 and 2013.

The correction function used in the flux reconstruction scheme is the Radau polynomial, which is equivalent to the discontinuous Galerkin scheme. A time-accurate implicit lower/upper symmetric Gauss–Seidel solution algorithm for the application of the flux reconstruction scheme to complex unsteady flows is developed, and it is found to be able to produce comparable results to the explicit Runge–Kutta scheme while achieving better computational efficiency. The effects of eddy viscosity calculated using the wall-adapting eddy viscosity model are evaluated and compared to no sub-grid scale modelling.

First, the Taylor–Green vortex problem is considered at Reynolds number of 1,600. Simulations are carried out with polynomials of degree $p = 1, 2, 3, 4, 5, 7$ resulting in up to eight-order-accurate flux reconstruction scheme. Domains involving from 64^3 to 256^3 degrees of freedom covers severely under-resolved to well-resolved scenarios. At polynomial orders $p = 5, 7$, stronger instabilities appear in the solution as the mesh resolution decreases. The dissipation added by the sub-grid model seems to have a stabilizing effect—to some degree—on the solution at high polynomial orders.

Secondly, the transitional flow over a SD7003 wing at Reynolds number of 60,000 is examined. Simulations are carried out at $\alpha = 4^\circ$ and 8° with polynomials of degree $p = 1, 2, 3$ resulting in second-, third-, and fourth-order-accurate flux reconstruction schemes, respectively. Two structured hexahedral O-grid domains that differ in the grid resolution in a circumferential direction on the upper surface of the wing are considered, with a maximum of 2,000,000 degrees of freedom for the fourth-order ($p = 3$) simulations on the finer domain. The eddy viscosity added through the sub-grid-scale model is found to have little effect on the solution. The results are validated by comparison with many reference data obtained from various high-order schemes using time-accurate explicit/implicit methods. The results agree reasonably well. The method developed with FR can be a reliable tool for ILES for low Reynolds number flows.

Acknowledgements

First, I would like to express my sincere gratitude to my supervisor Associate Professor Koji Miyaji for his guidance throughout my research work, for his support and encouragement as well as for his patience. His guidance helped me in all the time of research. I could not have imagined having a better advisor and mentor for my Ph.D. study.

Besides my advisor, my sincere thanks also goes to Professor Seiya Ueno and Associate Professor Takehiro Higuchi for their insightful comments and encouragement during my research.

Furthermore, I thank my fellow labmates for the stimulating discussions, for the sleepless nights we were working together before deadlines, and for all the fun we have had in the last three years. Special thanks go to Taito Sato, Yuichi Ishibashi and Daichi Toratani for the friendship we share, as well as their support on academic and day-to-day matters during my stay in Japan.

I am very grateful to the government of Japan for the Monbukagakusho: MEXT (Ministry of Education, Culture, Sports, Science and Technology), which made possible for me to live and study in Japan. Truly an experience of a lifetime.

Last but not the least, I would like to thank my family: my mother, brother and sister for for their love and continuous support.

Table of Contents

List of Tables

List of Figures

Nomenclature

Abbreviations

CD	compact difference method
CFD	computational fluid dynamics
CFL	Courant-Friedrichs-Lewy
CPU	central processing unit
CTU	convective time unit
DES	detached-eddy simulation
DG	discontinuous Galerkin method
DNS	direct numerical simulation
DOFs	degrees of freedom
FD	finite difference method
FR	flux reconstruction method
FV	finite volume method
GL	Gauss–Legendre points
ILES	implicit large-eddy simulation

LES large-eddy simulation

LGL Legendre–Gauss–Lobatto points

LSB laminar separation bubble

LU-SGS lower-upper symmetric Gauss–Seidel

NS Navier–Stokes equations

RANS Reynolds-averaged Navier–Stokes

RK Runge–Kutta method

SD spectral difference method

SGS subgrid-scale

WALE wall-adapting local eddy-viscosity

Symbols

α angle of attack

Δ local mesh size width

γ specific heat ratio, $\gamma = 1.4$ for air

ξ, η, ζ coordinates in a standard cubic element

a speed of sound

c airfoil chord

E, F, G flux vectors (viscous and inviscid)

J Jacobian matrix of coordinate transformation

M Mach number

N order of accuracy of flux reconstruction scheme

p polynomial degree

Pr Prandtl number, $Pr = 0.72$ for air

Q vector of conservative variables

Re freestream Reynolds number

S reference area

t^* nondimensional time, $t^* = tU_\infty/c$

u, v, w velocity in x,y,z direction

U_∞ freestream velocity

x, y, z Cartesian coordinates

x_r reattachment location

x_{sep} separation location

Other

C_D drag coefficient, $D/(\frac{1}{2}\rho_\infty U_\infty^2 S)$

C_f skin friction coefficient, $\tau_w/(\frac{1}{2}\rho_\infty U_\infty^2)$

C_L lift coefficient, $L/(\frac{1}{2}\rho_\infty U_\infty^2 S)$

C_p pressure coefficient, $(p - p_\infty)/(\frac{1}{2}\rho_\infty U_\infty^2)$

Δt^* nondimensional time step size

ω_z spanwise vorticity, $\omega_z = \frac{\partial v}{\partial x} - \frac{\partial u}{\partial y}$

$\overline{u'v'}$, $\overline{u'^2}$ Reynolds stress components

f^* nondimensional frequency, $f^* = fc/U_\infty$

TKE turbulent kinetic energy, $TKE = \frac{1}{2}\left(\overline{u'^2} + \overline{v'^2} + \overline{w'^2}\right)$

Subscripts

∞ freestream condition

sgs turbulent subgrid-scale quantities

Superscripts

$+$ wall units

$-$ time- and spanwise-mean quantities

c corrected value

com common value

inv inviscid term

visc viscous term

Chapter 1

Introduction

Today, with the increase of the practical importance of low Reynolds number flows, which are 2–3 orders of magnitude lower than the flight Reynolds number of 50 million for large transport aircraft, the importance of research into low Reynolds number flows is also increasing. Figure 1.1 illustrates a wide range of Reynolds numbers. Contemporary application examples at low Reynolds number include small windmills, micro gas turbines for power generation, micro-aerial vehicles known as drones, and long-endurance reconnaissance airplanes, which fly at very high-altitude. For example, according to the aerospace forecast published by the Federal Aviation Administration (FAA) for the years 2010–2030,[1] currently some 100 U.S. companies, academic institutions, and government organizations are developing over 300 types of unmanned aerial systems. It has been estimated by the FAA that 15,000 unmanned units will be employed by 2020 and 30,000 units by 2030, many of them probably designed for operation at low Reynolds number flows. The interested reader is referred to handbook [1] for further information on unmanned aerial vehicle (UAVs).

The Reynolds number assumed for such applications ranges from 10^4 to 10^5. The flow around an airfoil under this condition is characterized by a laminar-separation bubble (LSB). Such a flow has an unsteady three-dimensional nature, where initial acoustic or

[1] Federal Aviation Administration (FAA), *FAA Aerospace Forecast: Fiscal Years 2010–2030*, http://www.faa.gov/data_research/aviation/aerospace_forecasts/2010-2030/media/2010ForecastDoc.pdf (Retrieved: 5 June, 2015)

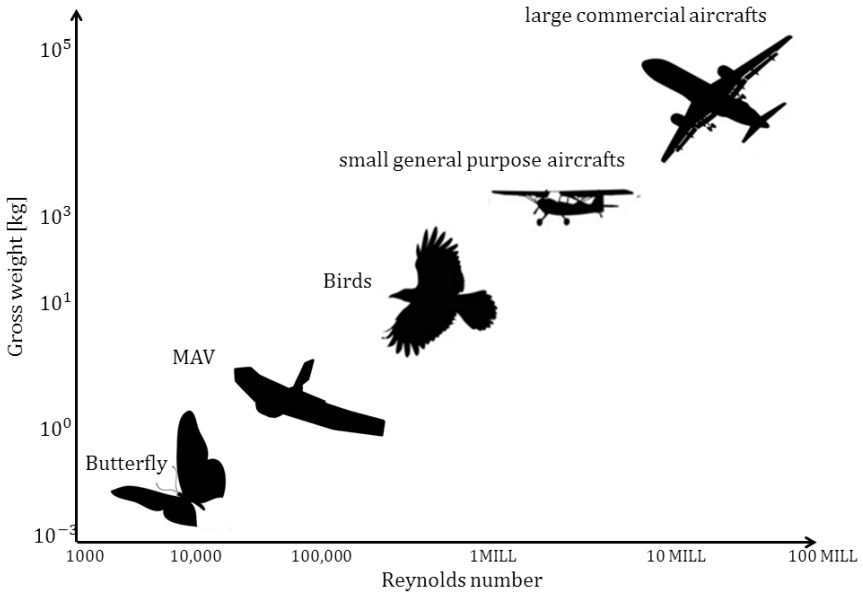

Figure 1.1: Range of Reynolds numbers with representative applications.

vortical perturbations at a tiny scale within the boundary layer are amplified in time, resulting in the growth of two- or three-dimensional instabilities. Numerical simulations able to predict this phenomenon successfully could significantly improve the design capability of low-Reynolds number aerospace applications, because LSBs have a strong influence on the performance of an airfoil. For example, a common strategy to reduce or avoid LSBs is to use airfoil turbulators, which are well-known mechanical devices for generating artificial disturbances forcing the boundary layer to become turbulent. However, such improvements at low flight speed have a cost, because the turbulators increase drag at cruise conditions. Feasible and accurate numerical simulations could lead to optimized turbulators or other novel strategies.

However, the transition to turbulence is a complex and challenging problem dependent on various factors ranging from the flow conditions (Re, M) to the local surface characteristics [2], as many pilots of modern gliders with laminar profiles—who expend much effort to remove dirt, such as bugs, from the wing surfaces after each flight—may agree. The simulations of flows with boundary layer transition and flow separation are non-trivial, and because of flows complexity, an accurate prediction of a transitional flow by a numerical simulation requires a scheme with low numerical viscosity and low dispersion errors.

This illustrates the following quote:

> Perhaps the single, most critical area in CFD simulation capability that will remain a pacing item by 2030 in the analysis and design of aerospace systems is the ability to adequately predict viscous turbulent flows with possible boundary layer transition and flow separation present. – NASA CFD Vision 2030 [3]

In the aforementioned vision study, the authors purposely defined a set of challenging problems. Some of these problems may not be feasible by 2030, but the successful achievement would be rightfully considered a milestone in engineering design capability. Before those goals can be achieved, the significant advances in many areas of computational fluid dynamics are needed because the improvement of computational power alone would not be sufficient [3].

Recently, the attempt to capture the complex flow mentioned above by high-order accurate and high-resolution schemes, together with the large-eddy simulation (LES) or ILES models without explicit sub-grid-scale eddy viscosity, show remarkable success in accounting for the transitional phenomena as well as the characteristic surface pressure and skin friction. However, the simulations are far from trivial and all employ state-of-the-art numerical schemes and essential computer resources to capture the transitional location, the turbulence statistics, and the unsteady aerodynamic forces due to the fluctuation of the separated shear layer. Several groups have employed unstructured grid methods with high-order accuracy, such as the DG method and SD method, which have made remarkable progress in the theory and applications in the last decade. The unstructured method is thus worth further exploration due to its inherent applicability to complex geometries and the ability of local h/p adaptations. In the present work, we examine Huynh's high-order flux reconstruction scheme (FR) [4, 5, 6] for the implicit large-eddy simulations (ILES) of a transitional flows at low Reynolds numbers.

1.1 Approach

The method developed with a high-order FR is examined with regard to feasibility, efficiency, and accuracy on two test cases, the TGV problem at a Reynolds number of 1,600, which is a canonical flow exhibiting homogeneous turbulence, and a low Reynolds number transitional flow over a rectangular infinite SD7003 wing, which represents a realistic

aerospace application. Simulations of the TGV at a Reynolds number of 1,600 are carried out on four mesh resolutions with a maximum of 256^3 degrees of freedom for the highest polynomial order of 7, corresponding to eighth-order accuracy in space.

The transitional flow over a SD7003 wing is simulated on two meshes with a maximum of 2,000,000 degrees of freedom for the fourth-order ($p = 3$) simulations on the finer domain. Two angles of attack are considered, 4° and 8°, representing two flows characterized by transition along long and short separation bubbles, respectively.

To enhance the numerical efficiencies of FR for an unsteady analysis, a time-accurate implicit lower/upper symmetric Gauss–Seidel (LU-SGS) solution algorithm for the application of the FR to complex unsteady flows is developed. Several numerical parameters of the LU-SGS scheme are investigated to limit numerical errors and investigate the performance and accuracy of the algorithm.

In the present work, we follow the implicit large-eddy simulation (ILES) approach. The unresolved small eddies are accounted for by numerical dissipation of the scheme and no sub-grid-scale model is employed. Boris [7, 8] discusses why the ILES approach should work from a physical point of view. Previous studies on FR [9, 10] and DG [11] have considered the dissipation and dispersion properties of the scheme by a von Neumann analysis. They showed that the dissipation of the scheme becomes progressively more focused on the higher wave numbers as the order of accuracy (polynomial degree) increases. This property gives us confidence in ILES by FR without using any special techniques, such as a posteriori filters. Moreover, the FR scheme with Radau polynomials as correction functions and Legendre–Gauss points recovers the DG scheme, i.e., DG via FR. We, therefore, assume that the FR scheme is also suitable for ILES, as was shown for DG [11, 12, 13].

Also, other researchers have reported the successful use of ILES for simulations of low Reynolds number transitional flow using various high-order numerical schemes. For example, ILES approaches have been successfully used by Visbal et al. [14, 15, 16] with a sixth-order compact difference method; by Uranga et al. [12, 17] using a DG method; and by Zhou and Wang [18], and Castonguay et al. [19] using a SD method. In general, the ILES approach seems to be successful in predicting the transitional flow, but the effects of explicit sub-grid-scale modeling on the solution are worth of further exploration. Therefore, selected simulations are recomputed in the LES framework and compared to ILES.

1.2 Outline of the Thesis

The contribution of the present work is twofold: first, to obtain a greater insight into the performance and capabilities of the method developed with a high-order flux reconstruction scheme, as a reliable tool for ILES for transitional flows at low Reynolds number; and secondly, to provide a comprehensive database of positive results (over 100,000 single-CPU hours in total) that could motivate further research on FR, as well as facilitating the evaluation of other state-of-the-art numerical schemes in the future. The structure of the document is the following:

Chapter 2

The reader is first introduced to the background behind the problem relevant to the present study, while additional literature references are provided for the interested reader: 1) LES and ILES approaches are briefly introduced; 2) an overview of high-order numerical schemes is given; 3) additional information on the laminar–turbulent transition and laminar-separation bubble is provided.

Chapter 3

This chapter describes the computational methods and methodology used during this study, from the governing equations and flux reconstruction scheme to the setup and solver.

Chapter 4

This chapter is on the validation of the current approach for the Taylor–Green vortex problem at $Re = 1{,}600$. The chapter is divided into two main parts: first, the effects of the polynomial order on the solution are examined; and second, LES and ILES are compared, while the positive effect of the eddy viscosity on the numerical stability is identified.

Chapter 5

The FR approach is successfully applied to a realistic aerospace application, represented by a transitional flow over a wing at $Re = 60{,}000$. To obtain representative statements for the behavior and performance of the FR scheme for realistic low-Reynolds number flow applications, numerous scenarios are simulated including different polynomial orders, angles of attack, mesh resolutions, time-stepping schemes and sub-grid scale modeling.

Chapter 6

The last chapter contains the conclusions that can be drawn from this work and lists the motivation for future work and perspectives.

Chapter 2

Background

2.1 Large-Eddy Simulation

The first attempts at large-eddy simulation (LES) can be traced back to the pioneering work of Smagorinsky [20] and Lilly [21] for meteorological applications, and to work by Deardorff [22] and Schumann [23] for engineering. The principle behind LES is that the important large scales are fully resolved as they carry most of the flow energy, whereas small scales of little influence are accounted for through the modeling. In the early 1970s, the LES approach, which was originally proposed for simulating atmospheric flows, was applied to relatively simple flows. However, with the improvement of computing power, LES has gained tremendous popularity for the study of complex flows including multi-phase flow, heat transfer, combustion, aeroacoustics etc. Nowadays, the availability of LES in commercial CFD codes is promising to increase the number of industrial applications of simpler flows in the very near future. On the other hand, it is estimated that LES for industrial applications of greater complexity, such as the flow over an aircraft, will not be feasible for 20–30 years. In the CFD vision study published by the National Aeronautics and Space Administration (NASA) for 2030, four Grand Challenge problems for the required CFD capabilities in 2030 were defined. One of them is a wall-resolved LES simulation of a full powered aircraft configuration for the full flight envelope. We refer the reader interested in the prospects of LES in industrial applications to [24, 25, 26].

The aforementioned distinction between resolved and modeled regions is via a low-pass filtering in the governing equations. Such a filtering operation reduces the range of scales that are being resolved; thus, it reduces significantly the computational cost compared to direct numerical simulations (DNS), which resolve the full spectrum of turbulence down to the smallest dissipative scales. On the other hand, the entire turbulence spectrum is modeled by a Reynolds-averaged Navier—Stokes approach (RANS). Therefore, the LES approach is promising to be more accurate than RANS, while less computationally demanding than DNS.

Figure 2.1 illustrates the difference between RANS, LES and DNS for an example of a turbulent kinetic energy spectrum plotted as a function of the length scale of the turbulent structures.

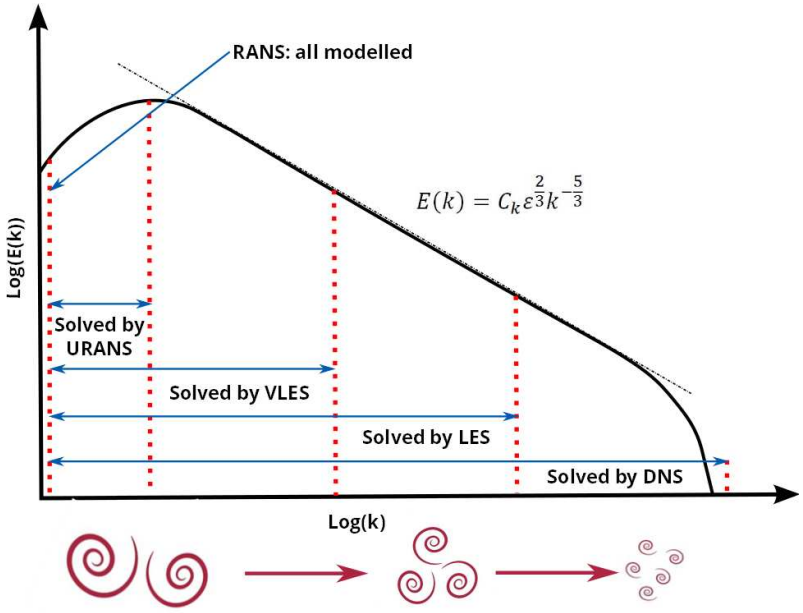

Figure 2.1: Turbulence energy spectrum. The figure has been redrawn based on [24].

The cutoff between the structures of a turbulent flow that are resolved and those that are modeled is done by the filtering operation. Two filtering operation approaches are widely recognized in LES. Explicit filtering applies an LES filter to the discretized governing equations, as an integral part of the solution process. Explicit filtering is performed on the

solution obtained from a finer grid; thus, it reduces the effective resolution of the simulation. This increases the computational cost considerably with $(\Delta)^4$ [27]. An advantage of explicit filtering is that the cutoff filter width (Δ) can be chosen independently of the mesh spacing. If the filter width is held fixed as the mesh is refined, the solution will converge to the true solution of the LES equations. Another advantage is that explicit filtering provides a way to control numerical errors, which dominate the high-energy portion of the spectrum [28].

The other filtering approach offers a straightforward implementation for LES in complex geometries. An implicit filtering procedure relies on a finite computational mesh together with the low-pass filtering effects of discrete derivative operators, which act as a filter. Thus, the small resolvable scales are proportional to the size of the local mesh. In contrast to the explicit filtering procedure, the solution will converge to a DNS as additional lengths are added each time the mesh is refined. The implicit filtering procedure has a disadvantage in that it does not provide any direct control of the energy in the high-frequency portion of the spectrum. This high-energy part, if coupled with the nonlinearities in the Navier–Stokes equations, can produce significant aliasing errors as discussed in [29]. Despite some disadvantages, the implicit—on the grid—filtering approach is commonly used for LES due to its lower calculation cost.

To ensure the accurate transfer of energy between the unresolved and resolved turbulent scales, the contributions from the unresolved scales smaller than the cutoff filter width Δ have to be accounted for [30]. In traditional LES, the contributions from the unresolved sub-grid scales (SGS) are included through a sub-grid model because they cannot be determined from the resolved flow field itself. Many different kinds of SGS models have been developed for LES [27, 31, 32, 33, 34]. Boris [7] discusses the properties of an ideal sub-grid model in detail. One of the most common selections for SGS modeling is based on the eddy-viscosity assumption from Boussinesq's hypothesis [35]. The wall-adapting local eddy-viscosity (WALE) model is discussed more thoroughly in Section 3.4.

An alternative to traditional LES is the implicit LES approach (ILES), which is based on a specific characteristic of the numerical scheme to mimic the physics of the unresolved turbulent motions. The sub-grid model is not implemented and the method stands on the numerical effects of the discretization to dissipate the energy at small scales. The absence of explicit sub-grid-scale models in the ILES approach offers computational efficiency and ease of implementation.

The first use of the ILES approach can be dated back to the early 1990s. Boris [36] assumed that the truncation errors of the numerical algorithm could in fact serve as an SGS model. Later, Boris and his collaborators at the Naval Research Laboratory (NRL) introduced the monotone integrated LES (MILES) approach. Since then, numerous groups have successfully employed the ILES approach to a wide range of applications in engineering, astrophysics and geophysics. The rationale behind the ILES with a high-order flux reconstruction scheme can be found in Section 1.1. In [7, 8], Boris discusses why the ILES approach should work from a physical point of view.

2.2 High-Order Numerical Schemes

High-order numerical schemes for solving the compressible Navier–Stokes equations on unstructured grids have been widely studied during the last decade.

Conventional second-order-accurate schemes usually have higher numerical dispersion and dissipation; they are often insufficient to predict accurately the flow in applications with complex physics and multiscale problems, such as vortex-dominated flows, boundary layer separations or computational aeroacoustics (CAA). The low-order-accurate schemes (with an order of accuracy of 2 or lower) are mostly too dissipative to resolve these flows accurately. The required level of accuracy could be achieved with finer meshes; however, mesh refinement is inefficient for low-order methods [37].

Higher-order methods could provide several potential benefits. When high-order methods can be fully exploited, such as the expected smooth solution problems, they could provide significant savings in computational effort (see Wang [38]), keeping the computational cost of problems requiring a high level of accuracy in the acceptable range. Moreover, they are usually better suited for applications such as computational aeroacoustics due to their better wave propagation properties. Among the CAA community, high-order methods are popular for their accuracy and efficiency when solving CAA problems [39].

Many methods have been developed for structured meshes, e.g. finite difference schemes with extended stencils, compact finite difference schemes [40, 41], and ENO and WENO schemes [42, 43, 44, 45].

To create a structured grid for complex geometries is far more difficult, while unstructured grids offer far more flexibility and utilize computer resources efficiently. Thus, active

research on high-order methods for unstructured grids has led to the development of numerical schemes, such as the discontinuous Galerkin (DG) [46, 47, 48], staggered-grid (SG) [49], spectral difference (SD) [50, 51] and flux reconstruction (FR) [5] methods. The unstructured methods are promising due to their inherent applicability to complex geometries and the ability of local h/p adaptations. The reader is referred to the original articles, as well as to comprehensive surveys of high-order methods by Wang [52], Wang et al. [37], Huynh et al. [53] and Jameson [54]. These sources discuss several aspects of high-order research.

2.3 Laminar Separation Bubble

The flow around an airfoil at low Reynolds numbers is characterized by a laminar separation bubble (LSB), which was first described in detail by Gaster [55]. Figure 2.3 shows a sketch of a LSB on a wing. The flow at moderate angles of attack, e.g. 10 degrees, first separates near the leading edge, and then the transition of the separated shear layer from being laminar to being turbulent occurs over the wing. Finally, the turbulent shear reattaches on the surface to form the LSB. The forepart of the LSB just behind the laminar separation point has very low velocities while the reversed flow region appears in the aft part before the reattachment point. The size of the LSB varies according to the airfoil shape and flow conditions. From experimental data, it was found that the variables that significantly affect the physical dimensions of the separation bubble are the Reynolds number, external disturbance and the angle of attack [56]. The increase in Reynolds number and the angle of attack, in general, reduces the size of the LSB, while a failure of the shear layer to reattach leads to a stall.

Figure 2.4 typically compares the pressure distributions on a wing for the inviscid solution and the viscous solution with an LSB. It shows that airfoil performance is affected remarkably.

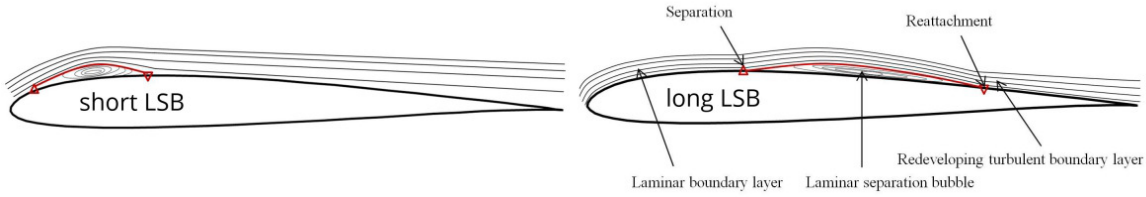

Figure 2.2: Long and short laminar separation bubble.

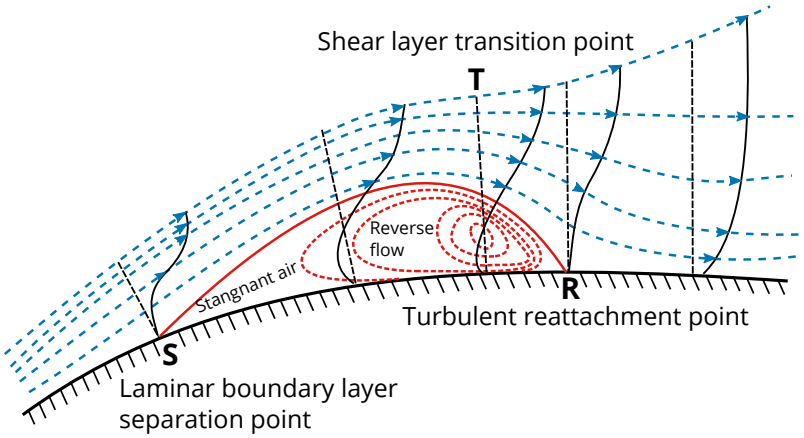

Figure 2.3: Schematical overview of a laminar separation bubble.

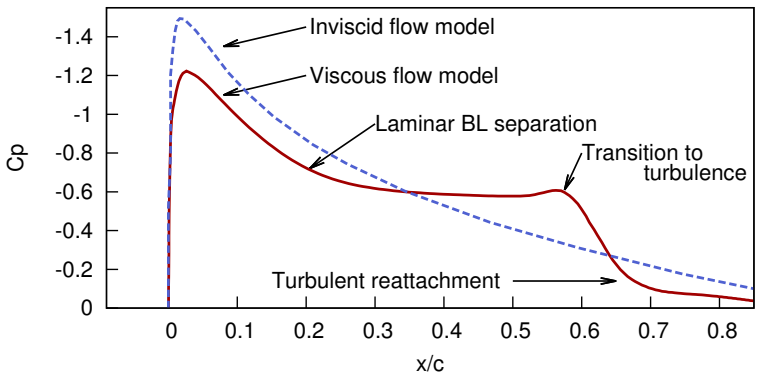

Figure 2.4: Comparison of the pressure distributions on a wing

Chapter 3

Methodology

3.1 Governing Equations

For calculations conducted in this study are used the three-dimensional, unsteady, compressible Navier–Stokes equations. The Navier-Stokes equation of motion was derived by Claude-Louis-Marie Navier in 1827, and independently by Siméon-Denis Poisson in 1831.

The motion of a compressible Newtonian fluid governed by the Navier–Stokes equations can be written in the conservation form as

$$\frac{\partial Q}{\partial t} + \frac{\partial E}{\partial x} + \frac{\partial F}{\partial y} + \frac{\partial G}{\partial z} = 0, \tag{3.1}$$

with the initial condition

$$Q(x, y, z, 0) = Q_0(x, y, z). \tag{3.2}$$

In 3.1, t denotes time, Q is a vector of conservative variables, and E,F and G are the fluxes in the Cartesian coordinates x,y, and z, respectively, which take the following form

$$Q = \begin{Bmatrix} \rho \\ \rho u \\ \rho v \\ \rho w \\ e \end{Bmatrix} \tag{3.3}$$

$$E = E^{inv} - E^{visc} = \begin{Bmatrix} \rho u \\ \rho u^2 + p \\ \rho uv \\ \rho uw \\ (e+p)u \end{Bmatrix} - \begin{Bmatrix} 0 \\ \tau_{xx} \\ \tau_{xy} \\ \tau_{xz} \\ u\tau_{xx} + v\tau_{xy} + w\tau_{xz} + \kappa\frac{\partial T}{\partial x} \end{Bmatrix} \tag{3.4}$$

$$F = F^{inv} - F^{visc} = \begin{Bmatrix} \rho v \\ \rho uv \\ \rho v^2 + p \\ \rho vw \\ (e+p)v \end{Bmatrix} - \begin{Bmatrix} 0 \\ \tau_{xy} \\ \tau_{yy} \\ \tau_{yz} \\ u\tau_{xy} + v\tau_{yy} + w\tau_{yz} + \kappa\frac{\partial T}{\partial y} \end{Bmatrix} \tag{3.5}$$

$$G = G^{inv} - G^{visc} = \begin{Bmatrix} \rho w \\ \rho uw \\ \rho vw \\ \rho w^2 + p \\ (e+p)w \end{Bmatrix} - \begin{Bmatrix} 0 \\ \tau_{xz} \\ \tau_{yz} \\ \tau_{zz} \\ u\tau_{xz} + v\tau_{yz} + w\tau_{zz} + \kappa\frac{\partial T}{\partial z} \end{Bmatrix} \tag{3.6}$$

where components of the velocity vector (u, u, w) align with the Cartesian-coordinate directions (x, y, z), κ is a thermal conductivity coefficient, T is temperature of the fluid, and superscripts inv, and $visc$ denotes inviscid, and viscous terms, respectively.

The total energy per unit volume e is represented by the following equation

$$e = \rho\left(\epsilon + \frac{u^2 + v^2 + w^2}{2}\right), \tag{3.7}$$

and the ϵ is an internal energy per unit volume, assuming the calorically perfect gas

$$\epsilon = c_v T = \frac{R}{\gamma - 1}T = \frac{1}{\gamma - 1}\frac{p}{\rho}, \tag{3.8}$$

where R is ideal gas constant, T is the temperature of the gas and γ is the constant ratio of specific heats set for air to 1.4.

The viscous stress tensor is defined by

$$\begin{aligned}
\tau_{xy} &= \tau_{yx} = \mu\left(u_y + v_x\right) \\
\tau_{yz} &= \tau_{zy} = \mu\left(v_z + w_y\right) \\
\tau_{zx} &= \tau_{xz} = \mu\left(w_x + u_z\right) \\
\tau_{xx} &= \frac{2}{3}\mu\left(2u_x - v_y - w_z\right) \\
\tau_{yy} &= \frac{2}{3}\mu\left(2v_y - u_x - w_z\right) \\
\tau_{zz} &= \frac{2}{3}\mu\left(2w_z - u_x - v_y\right).
\end{aligned} \tag{3.9}$$

The viscosity coefficient μ is related with the absolute temperature, T, of an ideal gas given by Sutherland's law [57],

$$\frac{\mu}{\mu_{ref}} = \left(\frac{T}{T_{ref}}\right)^{3/2} \frac{T_{ref} + S}{T + S} \tag{3.10}$$

where T_{ref} is a reference temperature, μ_{ref} is a viscosity at a reference temperature T_{ref}, and S is the Sutherland temperature (110.4K for dry air).

It is a common practice to work with the governing equations in a non-dimensional form as it makes the equations simpler, and highlights which terms are the most important. Dependent variables are non-dimensionalized by their respective reference values, e.g., density ρ^*_∞, speed of sound c^*_∞, temperature T^*_∞, viscosity coefficient μ^*_∞. Length scales are non-dimensionalized by the reference length L^*, e.g., length of the airfoil. Dimensional values are written with the asterix as a superscript.

$$\begin{aligned}
&\rho = \frac{\rho^*}{\rho^*_\infty}, \quad u = \frac{u^*}{c^*_\infty}, \quad v = \frac{v^*}{c^*_\infty}, \quad w = \frac{w^*}{c^*_\infty}, \quad x = \frac{x^*}{L^*}, \quad y = \frac{y^*}{L^*}, \quad z = \frac{z^*}{L^*} \\
&p = \frac{p^*}{\rho^*_\infty c^{*2}_\infty} = \frac{p^*}{\gamma p^*_\infty} \quad p_\infty = \frac{1}{\gamma} \quad , \quad e = \frac{e^*}{\rho^*_\infty c^{*2}_\infty} = \frac{p}{\gamma - 1} + \frac{1}{2}\rho\left(u^2 + v^2 + w^2\right) \\
&T = \frac{T^*}{T^*_\infty}, \quad c = \frac{c^*}{c^*_\infty} = \left(\frac{\gamma p}{\rho}\right)^{\frac{1}{2}}, \quad t = \frac{t^*}{L^*/c^*_\infty}, \quad \mu = \frac{\mu^*}{\mu^*_\infty}
\end{aligned} \tag{3.11}$$

Then, the non-dimensional governing equations takes following form

$$\frac{\partial Q}{\partial t} + \frac{\partial E}{\partial x} + \frac{\partial F}{\partial y} + \frac{\partial G}{\partial z} = 0, \tag{3.12}$$

where

$$Q = \begin{Bmatrix} \rho \\ \rho u \\ \rho v \\ \rho w \\ e \end{Bmatrix} \tag{3.13}$$

$$E = E^i - E^v = \begin{Bmatrix} \rho u \\ \rho u^2 + p \\ \rho uv \\ \rho uw \\ (e+p)u \end{Bmatrix} - \frac{1}{R_e} \begin{Bmatrix} 0 \\ \tau_{xx} \\ \tau_{xy} \\ \tau_{xz} \\ u\tau_{xx} + v\tau_{xy} + w\tau_{xz} + \frac{\mu}{(\gamma-1)P_r}\frac{\partial T}{\partial x} \end{Bmatrix} \tag{3.14}$$

$$F = F^i - F^v = \begin{Bmatrix} \rho v \\ \rho uv \\ \rho v^2 + p \\ \rho vw \\ (e+p)v \end{Bmatrix} - \frac{1}{R_e} \begin{Bmatrix} 0 \\ \tau_{xy} \\ \tau_{yy} \\ \tau_{yz} \\ u\tau_{xy} + v\tau_{yy} + w\tau_{yz} + \frac{\mu}{(\gamma-1)P_r}\frac{\partial T}{\partial y} \end{Bmatrix} \tag{3.15}$$

$$G = G^i - G^v = \begin{Bmatrix} \rho w \\ \rho uw \\ \rho vw \\ \rho w^2 + p \\ (e+p)w \end{Bmatrix} - \frac{1}{R_e} \begin{Bmatrix} 0 \\ \tau_{xz} \\ \tau_{yz} \\ \tau_{zz} \\ u\tau_{xz} + v\tau_{yz} + w\tau_{zz} + \frac{\mu}{(\gamma-1)P_r}\frac{\partial T}{\partial z} \end{Bmatrix}. \tag{3.16}$$

Two dimensionless parameters Pr and Re newly appears in eq. 3.13-3.16. The Pr stands for a dimensionless Prandtl number defined as the ratio of momentum diffusivity to thermal diffusivity

$$P_r = \frac{c_p^* \mu^*}{\kappa^*}, \tag{3.17}$$

set for air to $Pr = 0.72$. The latter, Re is Reynolds number defined as the ratio of of momentum forces to viscous forces

$$Re = \frac{\rho_\infty^* c_\infty^* L^*}{\mu_\infty^*}. \tag{3.18}$$

Please note that in Equation (3.11) are variables non-dimensionalized by the speed of sound c^*_∞. It is common practice in CFD to use reference velocity. Therefore, as we do not wish to confuse the reader, results presented in this study are following these conventions, thus, e.g., streamwise velocity is presented as $u = \frac{u^*}{u^*_\infty}$, non-dimensional time $t = \frac{t^*}{L^*/u^*_\infty}$ etc.

3.2 High–Order Flux Reconstruction Approach

The FR method is originally developed by Huynh [4, 5, 6], and the high-order accuracy of the FR scheme is achieved by the reconstruction of a high-degree solution polynomial on a given set of solution points (SP) in each computational cell/element. This concept is well known and used in other high-order methods, such as DG and SD. Like the SD method, FR is based on the differential form of Euler/Navier-Stokes equations. In contrast, the FR method needs only one grid for flux and solution points, rather than the two required by the SD method as shown in Figure 3.1. Huynh found links between several existing schemes (FR, DG, and SD), and their simpler and more economical equivalents can be recovered in the FR framework [4]. As the high-order flux reconstruction scheme has promising potential, research is being undertaken by several leading research groups in the CFD community. Recent advances are discussed in section 3.2.1.

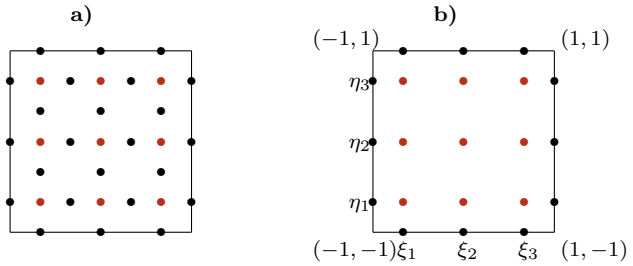

Figure 3.1: A sketch of the placement of solution and flux points within a standard 2D square element: a) solution points (red) and flux points (black) are staggered (spectral difference scheme) b) the flux is collocated with the solution (flux reconstruction scheme).

3.2.1 Recent Advances

Huynh proved, in his work presented between 2007 and 2009, a unified formula that includes nodal DG and SD as well as the original g^2 scheme in one dimension and tensor-product elements in multi dimensions, and in [6] (2011), he proved the reconstruction concept for triangles as well. This inspired the subsequent schemes called correction-procedure by reconstruction (CPR) [58] (2013) and energy-stable flux reconstruction (ESFR). These are also named after the authors as Vincent–Castonguay–Jameson–Huynh (VCJH) schemes [10] (2011), and they are applicable to simplex elements.

Recently, several groups have investigated the performance of schemes from the FR family. Miyaji [59] (2011) and Haga, Kuzuu et al. [60] (2013) conducted numerical simulations with the localized artificial diffusivity (LAD) method for suppressing oscillations in the vicinity of shocks. In the latter, a method for body-fitted Cartesian unstructured grids for aerospace flow simulations, including shocks, was developed. Miyaji [61] (2012) showed that vortical flow simulations exhibited a high-resolution property for large-scale vortices in a practical application of the leading-edge separation vortices of a laminar flow over a delta wing. For the 'resolved' vortices with given DOFs, the effect of the order of accuracy was determined and the method was compared with the finite-volume method. Liang, Cox, and Plesniak [62] (2013) compared FR with a SD scheme. They reported that FR was 27 percent faster than SD for an inviscid flow and over 40 percent faster than SD for viscous flow; both were fourth-order methods. Vermeire, Cagnone, and Nadarajah [63] (2013) and Vermeire, Nadarajah, and Tucker [64] (2014) conducted validation studies of unsteady isentropic vortex advection, supersonic flow through a curved duct, viscous circular Couette flow, the Comte-Bellot-Corsin experiment, the Taylor–Green vortex and turbulent channel flow. The FR scheme achieved the expected degree of accuracy and the results showed good agreement with previous numerical and experimental studies. Three-dimensional turbomachinery flows were simulated by Lu, Liu, and Dawes [65] (2012) and [66] (2013). Skarolek and Miyaji [67] (2014) conducted implicit large-eddy simulations with an FR scheme of a transitional flow at low Reynolds number of 60,000 around the SD7003 wing. The computed separation, reattachment, and aerodynamic forces (CL and CD) agreed reasonably well with many reference data obtained from various high-order schemes using time-accurate explicit/implicit methods. Grazia, Mendalgo et al. [68] (2013) analyzed connections between three versions of nodal DG and two FR schemes to identify which version of DG is in fact recovered.

Yu, Wang, and Liu [69] (2014) analyzed and compared the numerical accuracy and efficiency of quadrature-based DG, nodal DG, SD and FR schemes for the conservation laws. They reported that most schemes from the FR family cost less work units; i.e., they have a lower calculation cost to achieve a desired error level than other high-order methods on both linear and curved elements. Bull and Jameson [9, 70, 71] (2014, 2015) investigated the ability of FR schemes to perform an accurate and stable computation of a compressible Taylor–Green vortex. The FR showed good performance for simulations of turbulent flows on coarse meshes. Asthana and Jameson [72] (2014) focused on a complete modal analysis of the FR formulation and identification of spectrally optimal FR schemes with minimal dispersion and dissipation. Spiegel, Huynh, and DeBonis [73] (2015) investigated an over-integration approach, as a way of preventing aliasing errors for the FR, on simulations of the isentropic Euler vortex problem. As the over-integration approach for some test cases did not improve the robustness of the FR, the authors discuss and analyze the difficulties that they experienced with the vortex problem in [74]. A comprehensive review of recent advances can be found in Huynh et al. [53].

3.2.2 A Brief Review of the Formulation

The flux reconstruction scheme proposed by H. T. Huynh [4, 5, 6] implemented in the solver is briefly reviewed in this section.

The conservation form of the Navier–Stokes equations (see Section 3.1) is,

$$\frac{\partial Q}{\partial t} + \frac{\partial E}{\partial x} + \frac{\partial F}{\partial y} + \frac{\partial G}{\partial z} = 0, \tag{3.19}$$

where t is time, Q is a vector of conservative variables, and E, F and G are flux vectors including inviscid and viscous terms. The computational domain is discretized into non-overlapping elements Ω_j. It is convenient to transform each Ω_j in the physical domain (x, y, z) to a standard cube element Ω_s in the transformed space (ξ, η, ζ), where $(\xi, \eta, \zeta) \in [-1, 1] \times [-1, 1] \times [-1, 1]$ as shown in Figure 3.2. The transformation can be written as:

$$\begin{pmatrix} x(\xi,\eta,\zeta) \\ y(\xi,\eta,\zeta) \\ z(\xi,\eta,\zeta) \end{pmatrix} = \sum_{i=1}^{K} M_i(\xi,\eta,\zeta) \begin{pmatrix} x_i \\ y_i \\ z_i \end{pmatrix}, \tag{3.20}$$

where K is the number of points defining the physical element, (x_i, y_i, z_i) are the Cartesian coordinates at those points and $M_i(\xi, \eta, \zeta)$ are shape functions.

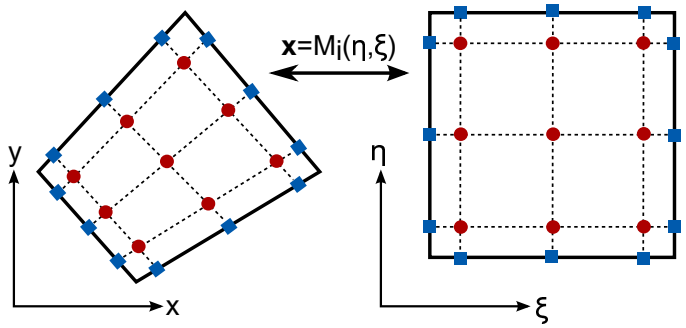

Figure 3.2: Mapping between the physical space (x,y) and the computational space (η,ξ) for the quadrilateral element.

The conservation equations transformed from the physical domain into the computational domain are written as:

$$\frac{\partial \widehat{Q}}{\partial t} + \frac{\partial \widehat{E}}{\partial \xi} + \frac{\partial \widehat{F}}{\partial \eta} + \frac{\partial \widehat{G}}{\partial \zeta} = 0, \tag{3.21}$$

$$\widehat{Q} = J \cdot Q, \quad \widehat{E} = \widehat{\xi}_x E + \widehat{\xi}_y F + \widehat{\xi}_z G, \quad \widehat{F} = \widehat{\eta}_x E + \widehat{\eta}_y F + \widehat{\eta}_z G, \quad \widehat{G} = \widehat{\zeta}_x E + \widehat{\zeta}_y F + \widehat{\zeta}_z G, \tag{3.22}$$

where the Jacobian and metrics of the transformation are calculated from (3.20) as:

$$J = x_\xi (y_\eta z_\zeta - y_\zeta z_\eta) + x_\eta (y_\zeta z_\xi - y_\xi z_\zeta) + x_\zeta (y_\xi z_\eta - y_\eta z_\xi), \tag{3.23}$$

$$\widehat{\xi}_x = y_\eta z_\zeta - y_\zeta z_\eta, \quad \widehat{\eta}_x = y_\zeta z_\xi - y_\xi z_\zeta, \quad \widehat{\zeta}_x = y_\xi z_\eta - y_\eta z_\xi, \quad \ldots \tag{3.24}$$

The polynomial of degree p, defined on $N = p + 1$ solution points, is used to represent the approximate solution inside each element Ω_s. The FR method offers some degree of flexibility for the choice of solution points, e.g., equidistant points, Legendre–Gauss–Lobatto (LGL) points (see Figure 3.3a), or Gauss–Legendre (GL) points (see Figure 3.3b). The interested reader is referred to original papers by Huynh [4, 5, 6]. In this study, we chose the Gauss–Legendre points for the solution and flux points. Two 1D elements with GL points are shown in Figure 3.4.

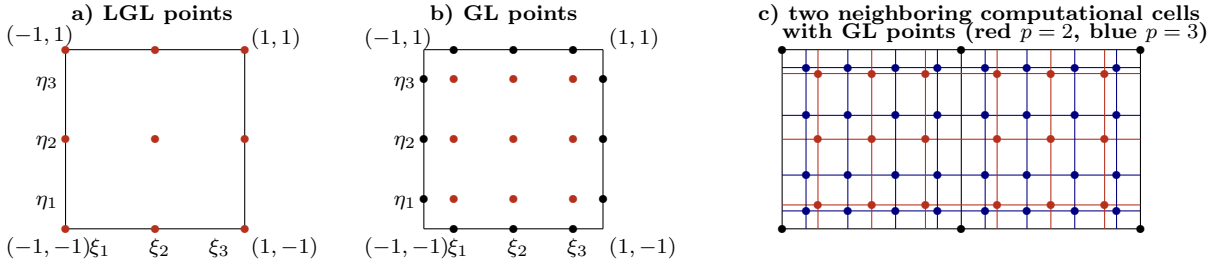

Figure 3.3: A standard 2D square element: a) Legendre–Gauss–Lobatto points lie on the cell edges, b) Gauss–Legendre points all lie inside the computational cell, c) two neighboring computational cells with Gauss–Legendre solution points, where black color shows the base grid, red color shows $p = 2$, and blue color $p = 3$ scheme.

Suppose nodal solutions are denoted as $\widehat{Q}_{i,j,k,l}$ at the (j, k, l) solution points in the cell i, then the piecewise-continuous pth-order solution polynomials can be reconstructed using the following tensor product of three 1D Lagrange polynomials of degree $p = N - 1$:

$$Q_i(\xi, \eta, \zeta) = \sum_{l=1}^{N} \sum_{k=1}^{N} \sum_{j=1}^{N} (J^{-1}_{i,j,k,l} \cdot \widehat{Q}_{i,j,k,l}) \phi_j(\xi) \phi_k(\eta) \phi_l(\zeta), \tag{3.25}$$

where

$$\phi_j(\xi) = \prod_{m=1, m \neq j}^{N} \frac{\xi - \xi_m}{\xi_j - \xi_m} \tag{3.26}$$

is the Lagrange basis polynomial. The solution is thus reconstructed with N^3 solution points in the cell. The cell local flux polynomials are obtained in a similar way from the flux values $\widehat{E}(Q_{i,j,k,l})$, $\widehat{F}(Q_{i,j,k,l})$ and $\widehat{G}(Q_{i,j,k,l})$ at the (j, k, l) solution points as follows:

$$\widehat{E}_i(\xi, \eta, \zeta) = \sum_{l=1}^{N} \sum_{k=1}^{N} \sum_{j=1}^{N} \widehat{E}_{i,j,k,l} \phi_j(\xi) \phi_k(\eta) \phi_l(\zeta). \tag{3.27}$$

$\widehat{F}(Q_{i,j,k,l})$ and $\widehat{G}(Q_{i,j,k,l})$ are obtained in a similar way. The flux is collocated with the solution. It improves numerical efficiencies in evaluating Jacobian and metrics, but it may result in errors for non-linear flux like in the Navier-Stokes equations, compared with a staggered-grid arrangement in Kopriva and Kolias [49].

The element-wise solution functions are generally discontinuous across the interfaces, as depicted in Figure 3.5. To obtain a globally continuous flux polynomial, the discontinuous

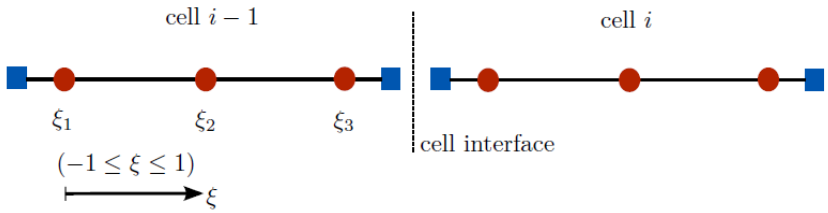

Figure 3.4: Two 1D reference elements for p=2. Solution points are represented by red circles and flux points by blue squares.

fluxes need to be corrected to match the common values at the cell interfaces. This is important to prevent any loss of interaction between adjacent cells. Huynh proposed adding correction functions to modify the discontinuous flux polynomials in a convenient way that they match the common interface fluxes at the left and right interfaces of the element. The correction function, which is a polynomial of degree N, requires an additional

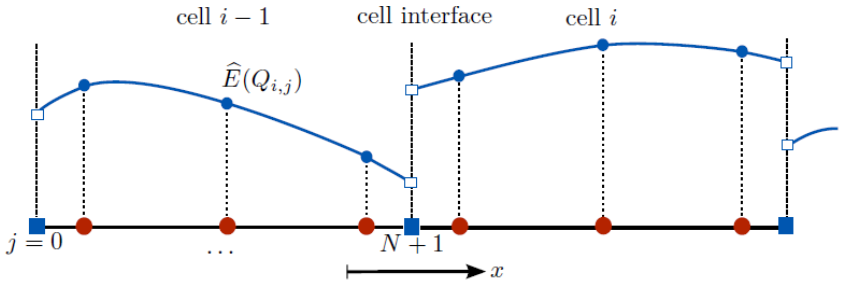

Figure 3.5: Approximate flux $\widehat{E}$ in the standard element are generally discontinuous across cell interface.

$N-1$ conditions together with prescribed boundary conditions (3.29). Huynh derived various correction functions from Legendre, Radau or Lobatto polynomials. The choice of correction function has an influence on the stability and accuracy. With the Radau polynomial g_{DG}, a scheme identical to nodal DG can be recovered. g_{SG} denotes the function that is defined on $N+1$ Chebyshev–Lobato points, from which a simplified version of the staggered-grid [49] (SG) scheme can be recovered. The scheme with g_{SG} is less accurate but has better stability compared to the scheme with g_{DG}. The Radau polynomials are chosen as the correction functions for inviscid and viscous fluxes, thus the scheme recovered is identical to nodal DG as shown by Hyunh [5] and Grazia et al. [68].

The corrected, globally C^0-continuous flux polynomial $\widehat{E}_i^C$ is close to $\widehat{E}_i$ and it should be a polynomial of degree $p+1$. This ensures that its spatial derivative has degree $p = N-1$, the same polynomial degree as Q_i in (3.19). The common inviscid numerical fluxes can be evaluated at each interface using a simple Rusanov solver [75]. In Figure 3.7 is shown how the numerical flux at cell interface is computed using left-, and right-side values.

With the common numerical flux $\widetilde{E}^{com}_{i\pm1/2}(\eta_k, \zeta_l)$ $(k, l = 1, \ldots, N)$ at the boundary in the ξ direction, the corrected flux polynomial $\widehat{E}_i^C$ is

$$\widehat{E}_i^C(\xi, \eta_k, \zeta_l) = \sum_{j=1}^{N} \widehat{E}_{i,j,k,l} \cdot \phi_j(\xi) + \left[\widetilde{E}^{com}_{i-1/2}(\eta_k, \zeta_l) - \widehat{E}_i(-1, \eta_k, \zeta_l)\right] g_L(\xi) + \left[\widetilde{E}^{com}_{i+1/2}(\eta_k, \zeta_l) - \widehat{E}_i(1, \eta_k, \zeta_l)\right] g_R(\xi), \quad (3.28)$$

where $i-1/2$ and $i+1/2$ represent the left and right interfaces of the cell i, respectively. g_L and g_R are the left and right correction functions (see Figure 3.6); they are polynomials of degree $p+1$ with prescribed boundary conditions:

$$g_L(-1) = 1, \quad g_L(1) = 0, \quad g_R(-1) = 0, \quad g_R(1) = 1. \quad (3.29)$$

The derivative of the corrected flux polynomial $\widehat{E}_i^C$ (3.28) in the following equation is used to evaluate the term $\widehat{E}_\xi$ in (3.21):

$$(\widehat{E}_i^C)_\xi(\xi, \eta_k, \zeta_l) = \sum_{j=1}^{N} \widehat{E}_{i,j,k,l} \cdot \phi'_j(\xi) + \left[\widetilde{E}^{com}_{i-1/2}(\eta_k, \zeta_l) - \widehat{E}(-1, \eta_k, \zeta_l)\right] g'_L(\xi) + \left[\widetilde{E}^{com}_{i+1/2}(\eta_k, \zeta_l) - \widehat{E}(1, \eta_k, \zeta_l)\right] g'_R(\xi). \quad (3.30)$$

The derivatives $\widehat{F}_\eta$ and $\widehat{G}_\zeta$ can be evaluated in a similar manner.

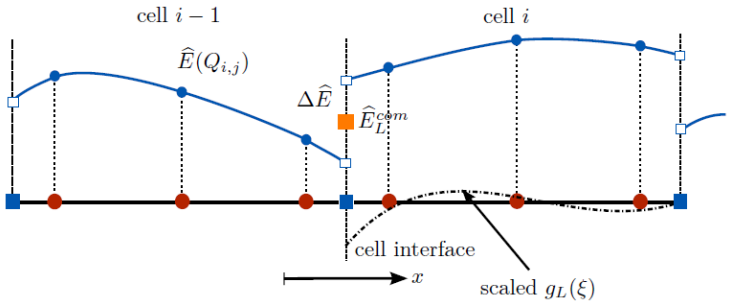

Figure 3.6: The numerical flux at cell interface is computed using left-, and right-side values.

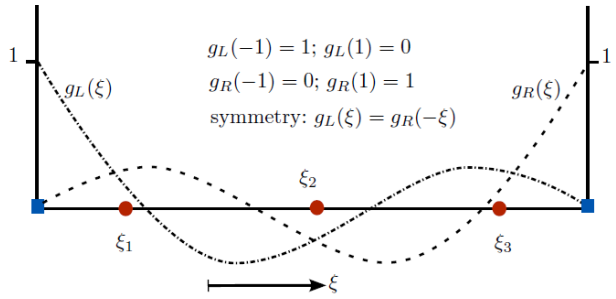

Figure 3.7: Examples of left and right corrections for the case p = 2. Degree $p+1$ flux correction functions $g_L = g_L(\xi)$ and $g_R = g_R(\xi)$ approximate zero in some sense and satisfy prescribed boundary conditions.

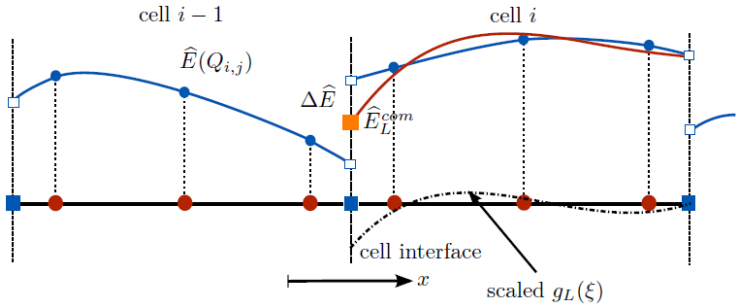

Figure 3.8: The approximate correction flux, obtained as scaled correction function g_L, is added to the approximate discontinuous flux $\widehat{E}$. The process is repeated for left and right interfaces of all cells. The corrected, globally C^0-continuous flux polynomial $\widehat{E}^C$ is close to $\widehat{E}$ and it should be a polynomial of degree $p+1$.

A viscous flux vector is a function of conservative variables and their gradients. Calculation of the first derivative of quantity u with respect to ξ for the viscous term is similar to (3.30):

$$(u_i^C)_\xi = \sum_{j=1}^{N} u_{i,j} \cdot \phi_j(\xi) + \left[u_{i-1/2}^{com} - u_i(-1)\right] g_L(\xi) + \left[u_{i+1/2}^{com} - u_i(1)\right] g_R(\xi), \tag{3.31}$$

with the indices k and l omitted for conciseness. The second Bassi–Rebay (BR2) [76] scheme with compact stencil is implemented to discretize the viscous fluxes. The common viscous flux $u_{i+1/2}^{com}$ is evaluated as the average of the two, right and left, values at the interface as:

$$u_{i+1/2}^{com} = \frac{1}{2}\left[u_i(1) + u_{i+1}(-1)\right]. \tag{3.32}$$

A similar process to (3.31) is repeated to obtain the second derivative. $(u_i^C)_\xi$ is discontinuous at the cell interfaces and common first derivatives are necessary. Since the corrected derivative $(u_i^C)_\xi$ is readily available, we can obtain common derivatives at the interface as:

$$(u_\xi)_{i+1/2}^{com} = \frac{1}{2}\left[(u_i^R)_\xi(1) + (u_{i+1}^L)_\xi(-1)\right], \tag{3.33}$$

where $(u_i^R)_\xi$ and $(u_{i+1}^L)_\xi$ are the derivative of the following functions that respectively employ the right and left correction functions in the cell i and $i+1$:

$$\begin{aligned} u_i^R(\xi) &= u_i(\xi) + \left[u_{i+1/2}^{com} - u_i(1)\right] g_R(\xi) \\ u_{i+1}^L(\xi) &= u_{i+1}(\xi) + \left[u_{i+1/2}^{com} - u_{i+1}(-1)\right] g_L(\xi). \end{aligned} \tag{3.34}$$

The viscous flux vectors are calculated at all solution points. Finally, when all divergence terms in (3.21) are evaluated at all solution points, any suitable time discretization method can be used to update the solution $\widehat{Q}_{i,j,k,l}$ in time.

3.2.3 Connections between FR and DG

In his original paper, Huynh [5] proved on a case of linear advection that a nodal DG scheme can be formulated taking the differential form inside the FR framework and vice versa. In 2013, De Grazia et al. [68] examined connections between three nodal versions of DG and two FR schemes for the case of an advection equation to: 1) identify which variant of DG

scheme can be recovered by the FR; 2) demonstrate that schemes are also equivalent for a nonlinear advection equation. De Grazia et al. demonstrated, for a advection equation, the DG spectral element method (DGSEM) with an exact mass matrix and the DG recovered via FR are equivalent on a regular grid. The careful reader is referred to the original article for mathematical proof and numerical verification.

3.3 Temporal Discretization

Explicit and implicit algorithms for temporal discretization were used in the present study. The former, explicit schemes, such as the explicit Runge–Kutta (RK), are easy to implement, and have a low CPU cost per iteration, since no matrices have to be inverted. On the other hand, explicit schemes suffer from low stability and hence have a limitation on the maximum allowable time step, especially for convection-dominated compressible flows, where viscous grids are clustered in the viscous boundary layer. The latter, implicit schemes can advance the solution with significantly larger time steps, theoretically infinitely large. However, there are restrictions on the maximum allowable time step due to the non-linearities of the flow equations and the accuracy requirements of the unsteady flows. The matrix inversion causes the CPU cost per iteration to be significantly higher, and storing these matrices for matrix manipulations leads to higher memory requirements compared to explicit methods.

In the FR solver are implemented: (i) a third-order accurate-in-time three-stage TVD Runge–Kutta explicit method (TVD-RK3) [77], (ii) the "classic" fourth-order accurate Runge–Kutta explicit method (RK4), and (iii) a second-order accurate-in-time implicit non-linear lower-upper symmetric Gauss–Seidel method (LU-SGS) [78].

Two types of implicit algorithms are widely used for high-order schemes on unstructured grids: LU-SGS and the generalized minimal residual (GMRES) solution algorithms. We would like to cite from the article by Gang, Yuewen, and Zhengyin [79], as we do not have previous experience with the GMRES:

- The strong point of the GMRES scheme is that the quadratic convergence speed can be achieved as the size of the time step is close to infinite.
- The GMRES scheme is characterized with high computational complexity and large memory consumption.

- LU-SGS does not require direct inversion of a large implicit system matrix.
- LU-SGS is easier to implement and has a lower computational cost for marching one time step.
- LU-SGS usually needs more iteration steps to reach the same convergence level compared with GMRES.

The use of the LU-SGS scheme in this study is motivated by available positive data from the literature. Kitamura et al. [80] employed the preconditioned LU-SGS for low-speed flows. Implicit LU-SGS has also been successfully used for SD and SV, such as the methods in papers by Sun et al. [78], Parsani et al. [81], and Kannan [82]. The LU-SGS scheme was adapted for SD by Sun et al., and the results indicate that LU-SGS can considerably improve the convergence rate for the flows they simulated. Due to the similarity of SD with FR is adaptation of the scheme for FR quite straightforward.

3.3.1 Second-Order Accurate LU-SGS Algorithm

An implicit non-linear lower-upper symmetric Gauss–Seidel (LU-SGS) [78] solution algorithm has been adopted for the FR scheme, the LU-SGS is preconditioned by a block element matrix, and the system of equations is then solved with a direct LU decomposition solver. The LU decomposition solve on the element (or cell) matrix associated with each element (the left-hand side of the equation 3.40).

The LU-SGS scheme that was originally first-order accurate is extended to be second-order accurate in time. The following lines give a brief overview of the implemented scheme. Equation (3.21) is rewritten as:

$$\frac{\partial \widehat{Q}_i}{\partial t} = R_i(\widehat{Q}), \tag{3.35}$$

where $\widehat{Q}_i$ and R_i are vectors for the solution and residuals at all the solution points in the cell i with dimensions $5 \times \text{order}^3$. The semi-discrete equation using a three-point backward difference in time is

$$\frac{3\widehat{Q}_i^{n+1} - 4\widehat{Q}_i^{n} + \widehat{Q}_i^{n-1}}{2\Delta t} = R_i(\widehat{Q}^{n+1}). \tag{3.36}$$

Let $\Delta\widehat{Q}_i = \widehat{Q}^{n+1} - \widehat{Q}^n$ and since $\widehat{Q}_i^{n+1}$ is unknown on current time level, the residual $R_i(\widehat{Q}^{n+1})$ can be linearized about the state at time index n by using a first-order Taylor expansion. The fully linearized equations for (3.36) can be written as

$$\left[\frac{3I}{2\Delta t} - \frac{\partial R_i}{\partial \widehat{Q}_i}\right]\Delta\widehat{Q}_i - \sum_{nb=i}\frac{\partial R_i}{\partial \widehat{Q}_{nb}}\Delta\widehat{Q}_{nb} = R_i(\widehat{Q}^n) + \frac{\widehat{Q}_i^n - \widehat{Q}_i^{n-1}}{2\Delta t}, \tag{3.37}$$

where nb indicates neighboring cells contributing to the residual of the cell i. Using a relaxation method,

$$\left[\frac{3I}{2\Delta t} - \frac{\partial R_i}{\partial \widehat{Q}_i}\right]\Delta\widehat{Q}_i^{(k+1)} = R_i(\widehat{Q}^n) + \sum_{nb=i}\frac{\partial R_i}{\partial \widehat{Q}_{nb}}\Delta\widehat{Q}_{nb}^{*} + \frac{\widehat{Q}_i^n - \widehat{Q}_i^{n-1}}{2\Delta t}, \tag{3.38}$$

where superscript k is a sub-iteration index of the symmetric Gauss–Seidel and superscript $*$ indicates the most recently updated solutions. Employing ingenious manipulations by Sun et al. [78] to eliminate matrices $\partial R_i/\partial\widehat{Q}_{nb}$ which we do not want to store, one obtain

$$R_i(\widehat{Q}^n) + \sum_{nb=i}\frac{\partial R_i}{\partial \widehat{Q}_{nb}}\Delta\widehat{Q}_{nb}^{*} = R_i(\widehat{Q}^{*}) - \frac{\partial R_i}{\partial \widehat{Q}_i}\Delta\widehat{Q}_i^{*}. \tag{3.39}$$

Combining (3.38) and (3.39) together with $\Delta\widehat{Q}_i^{(k)} = \widehat{Q}_i^{(k)} - \widehat{Q}_i^n$, the final form can be written as

$$\left[\frac{3I}{2\Delta t} - \frac{\partial R_i}{\partial \widehat{Q}_i}\right](\widehat{Q}_i^{(k+1)} - \widehat{Q}_i^{(k)}) = R_i(\widehat{Q}^{*}) - \frac{3\widehat{Q}_i^{*} - 4\widehat{Q}_i^n + \widehat{Q}_i^{n-1}}{2\Delta t}, \tag{3.40}$$

where the right-hand side is the unsteady residual that is found in (3.36) and it needs to drop sufficiently within sub-iterations for unsteady problems. A numerical or analytical approach can be used for the computation of the element Jacobi matrix. The analytical approach leads to a complex formulation whereas the numerical approach is easier to implement. We have used finite difference to compute the Jacobian matrix $\partial R_i/\partial\widehat{Q}_i$ as used in [78],

$$\frac{\partial R_i}{\partial \widehat{Q}_i} \approx \frac{R_i(\{\widehat{Q}_{nb}\}, \widehat{Q}_i + \epsilon) - R_i(\{\widehat{Q}_{nb}\}, \widehat{Q}_i)}{\epsilon},$$

where ϵ is a small parameter, $\epsilon \approx \|\widehat{Q}_i\| \times 10^{-8}$.

However, numerical computation of the Jacobian matrix $\partial R_i/\partial\widehat{Q}_i$ with dimensions $25 \times \text{order}^6$ every iteration is quite expensive. Therefore, we have followed the Jacobi

matrix-freezing approach [78]. The Jacobi matrix is recalculated every n-th iteration, where n is usually between 10-100 in the literature. This approach can significantly increase efficiency, but careful validation is needed, as improperly high interval n could affect the results.

3.4 Wall-Adapting Local Eddy-Viscosity Model

We have implemented the wall-adapting local eddy-viscosity (WALE) model proposed by Nicoud and Ducros [83]. This model, like other eddy-viscosity models, belong to the class of functional sub-grid scale models. They reproduce the effect of the unresolved scales on the resolved field by treating dissipation of kinetic energy at sub-grid scales as analogous to molecular diffusion. Such an effect can be accounted for by addition of eddy viscosity (ν_{sgs}) to the solution, which is assumed to be proportional to the sub-grid dissipation. Thus, the aim of sub-grid modeling is to withdraw energy from the resolved turbulent structures in order to mimic the forward kinetic energy cascade in the unresolved part [27, 34].

Based on the use of the eddy-viscosity assumption, approximate of the sub-grid scale tensor is modeled as

$$\tau_{ij}^{sgs} = 2\nu_{sgs}\bar{S}_{ij} \tag{3.41}$$

where ν_{sgs} is the eddy viscosity, and

$$\bar{S}_{ij} = \frac{1}{2}\left(\frac{\partial \bar{u}_i}{\partial x_j} + \frac{\partial \bar{u}_j}{\partial x_i}\right), \tag{3.42}$$

is the rate-of-strain tensor of the resolved scales.

Many models have been developed for calculation of the eddy viscosity ν_{sgs}, e.g., the Smagorinsky model [20], Germano's dynamic Smagorinsky model [84], WALE model [83] and others. For more information on the topic of sub-grid scale modeling the reader is referred to [27, 34, 85].

The idea of the WALE model is reproduce the proper scaling at the wall with returning the correct wall-asymptotic y^{+3}-variation of the SGS viscosity [83], and the ν_{sgs} goes naturally to zero in the vicinity of a wall. In addition, this model is well-suited for LES in complex geometries because only local information is needed.

The WALE model computes the eddy viscosity (ν_{sgs}) and thermal diffusivity (κ_{sgs}) by: [83]

$$\nu_{sgs} = C^2\Delta^2 \frac{(\bar{S}^d_{ij}\bar{S}^d_{ij})^{3/2}}{(\bar{S}_{ij}\bar{S}_{ij})^{5/2} + (\bar{S}^d_{ij}\bar{S}^d_{ij})^{5/4}}, \tag{3.43}$$

where C is a model constant, Δ defines the characteristic filter length and $\bar{S}^d_{ij}$ is the traceless symmetric part of the square of the resolved velocity gradient tensor $\bar{g}_{ij}$

$$\bar{g}_{ij} = \frac{\partial \bar{u}_i}{\partial x_j} \tag{3.44}$$

given as

$$\bar{S}^d_{ij} = \frac{1}{2}\left(\bar{g}^2_{ij} + \bar{g}^2_{ji}\right) - \frac{1}{3}\delta_{ij}\bar{g}^2_{kk}, \tag{3.45}$$

with

$$\bar{g}^2_{ij} = \bar{g}_{ik}\bar{g}_{kj}. \tag{3.46}$$

The thermal diffusivity κ_{sgs} is computed as

$$\kappa_{sgs} = \frac{\nu_{sgs}}{Pr_{sgs}}. \tag{3.47}$$

In the present study, the model constant C is set to 0.3, a value that was also used by Lodato et al. [86]. The SGS Prandtl number, Pr_{sgs} is assumed constant and equal to 0.5 [86, 87, 88]. Then, the x-component of the subgrid heat-flux vector, q^{sgs}, is computed by [81, 89]:

$$q^{sgs}_x = c_p \frac{\nu_{sgs}}{Pr_{sgs}} \frac{\partial \bar{T}}{\partial x} = c_p \kappa_{sgs} \frac{\partial \bar{T}}{\partial x} \tag{3.48}$$

In Equation (3.43), Δ defines the characteristic filter length. Usually computed as $\Delta = (\Delta x \Delta y \Delta z)^{1/3}$, where Δx, Δy, Δz is the size of the cell in the x-, $y-$, z-direction, respectively. However, Parsani et al. suggested that for use with high-order schemes is more appropriate to choose the filter width depending on the order of the polynomial. Parsani et al. [81] suggested procedure for spectral difference scheme, where the order of the polynomial is taken into account through the division of the Jacobian determinant by the number of solution points as follows:

$$\Delta_{i,l} = \left(\frac{J_{i,l}}{N} \right)^{1/dim}, \tag{3.49}$$

where i is a computational cell with index, l index of each solution points, $N(p, dim)$ is number of solution points, and J is the determinant of the Jacobian matrix.

3.5 Computational Methodology

The FR solver solves unsteady three-dimensional compressible Navier–Stokes equations using the flux reconstruction scheme for spatial discretization. All numerical simulations are carried out on structured hexahedral domains in this study, but the solver can also be applied to general unstructured hexahedral meshes. Structured meshes are generated in a commercial software for grid generation GridGen from Pointwise, Inc.

Grid generation for a high-order simulation is a bit more challenging, as high-order methods can achieve similar accuracy on a much coarser mesh than low-order methods. Therefore, quite coarse meshes are often sufficient for a high-order simulations. However, special care must be taken to capture higher-order geometry information of curved boundaries with high-order polynomials, as the linear elements are often not suitable for higher-order discretizations [76]. In this study, a high-order grid is used. The grid has been curved in a circumferential direction, i.e. a curved direction, with the use of cubic-shaped elements for the cells on the curved boundaries. The shape functions (3.20) of the cells on curved boundaries must first be modified, and then the meshes prepared with three times finer curved direction in any suitable software. This manual refinement gives us the four points that are needed for cubic functions in each cell on the curved boundaries.

Simulations in this study are computed by a parallel solver using the Message Passing Interface [90] (MPI). Computational domains are partitioned into the corresponding number of regions (number of CPUs) by the partitioning scheme Metis [91]. The maximum number of CPUs used in this study is 132. In order to make comparisons regardless of the machine used, the computational costs are provided normalized and expressed in work units. The work units are adopted from guidelines of the third HIOCFD. A three-dimensional Navier-Stokes code (TauBench)[1] developed at the German Aerospace Center

[1]Data available online at http://www.as.dlr.de/hiocfd/taubench_src.tar.gz (Accessed: 06/10/2015)

(DLR) for benchmarking was run on the machine equipped with Intel® Xeon® X5680 CPUs running at 3.33 GHz. The average time over four runs was 7.89 s. The work unit is defined as T_2/T_1 where T_2 is CPU time taken by our solver using a single CPU, excluding the initialization, post-processing, data preparation, and file I/O time. The time T_1 is CPU time of the TauBench benchmark with 10 pseudo steps on the grid with $250,000$ DOFs, using a single CPU.

The implicit LU-SGS scheme is used for a temporal discretization in the SD7003 wing (Chapter 5) test case. The calculation cost with the second-order accurate LU-SGS scheme is about 1.5% higher than the cost with the first-order accurate LU-SGS scheme. For simulations of the Taylor–Green vortex (Chapter 4) is used a third-order accurate-in-time three-stage TVD Runge–Kutta explicit method due to a lower memory consumption. This is especially noticeable at simulations using very fine domains with 256^3 DOFs.

Chapter 4

Taylor–Green vortex at $Re = 1,600$

The Taylor–Green vortex (TGV) problem is a canonical flow for which a turbulent energy cascade can be easily observed numerically. The TGV is started from a simple initial condition. As the simulation continues, the flow transitions from an initially two-dimensional single-mode flow field to a three-dimensional fully turbulent flow. This transition at $t^* > 0$ naturally occurs due to the existence of a pressure gradient in the flow field. The turbulent energy is transferred to smaller scales through the vortex-stretching mechanism, and the flow decays over a period of 20 seconds.

The fully developed decaying turbulent flow contains small scales covering a full turbulent spectrum and it exhibits the features of homogeneous turbulence. This makes the TGV problem a challenging test for numerical schemes, and as such, the TGV has become popular for code validation and evaluation of numerical schemes.

In this chapter, results from numerical simulations of the compressible TGV problem at $Re = 1600$ using a flux reconstruction (FR) scheme recovering the nodal discontinuous Galerkin (DG) are presented and discussed. We employ this test case to validate our FR code, as well as to verify the ability and performance of the FR scheme for under-resolved large-eddy simulations of turbulent flows. Simulations are carried out with degree $p = 1, 2, 3, 4, 5, 7$ polynomials resulting in second-, third-, fourth-, fifth-, sixth- and eight-order accurate FR schemes, respectively.

In the following, literature sources are discussed in Section 4.1, the computational setup is described in Section 4.2, and in Section 4.3, the results are presented and discussed.

4.1 Literature Review

The TGV problem was proposed in the category of three-dimensional and difficult problems in the 1st and 2nd international workshops on high-order computational fluid dynamics methods (HIOCFD) held in 2012 and 2013. In those workshops, the participants compared their results using solvers based on various methods, such as DG, finite difference, finite volume, FR, and spectral difference methods. A summary of the 1st HIOCFD workshop and a description of 15 benchmark cases, which were adopted in the workshop, can be found in [37] and in the workshop website (http://zjwang.com/hiocfd.html). Additional information about the 2nd HIOCFD workshop can be found in the workshop website (http://www.dlr.de/as/hiocfd). However, reports of solutions of this flow using methods achieving high-order accuracy are not only restricted to HIOFCD.

Direct simulation of three-dimensional turbulence in a TGV was performed by Brachet [92] in 1991. In his paper, Brachet used a pseudo-spectral method with a resolution of 864^3. In 2011, van Rees [93] compared the hybrid particle-mesh vortex method against a pseudo-spectral method for the TGV at $Re = 1600$. It was shown by van Rees that the solution of the TGV at $Re = 1600$ was fully converged with 512^3 degrees of freedom (DOFs).

Following the recommendation of the HIOCFD committee, a pseudo-spectral computation is taken as a reference. The FR results presented in this study are compared to a pseudo-spectral computation performed by Carton de Wiart, Hillewaert, Duponcheel, and Winckelmans [94] (2013) on a 512^3 mesh. The aforementioned authors performed TGV simulations at $Re = 1600$ using a DG method on hexahedral meshes and unstructured high-quality meshes. The TGV benchmark has also been studied by Gassner and Beck [95, 96] (2012) using a high-order discontinuous Galerkin spectral element method (DGSEM). Gassner and Beck investigated the accuracy of a high-order DG method for coarse under-resolved turbulence simulations. They employed high-order approximations up to $p = 15$. Although, the $p = 7$ and $p = 15$ simulations needed stabilization by de-aliasing via over-integration, they showed the good accuracy of the method for such simulations.

DeBonis [97] (2013) performed TGV simulations using finite difference methods based on central differencing (up to 12th-order accurate) on grids ranging from 64^3 to 512^3. He also examined the effect of sub-grid models based on large-eddy simulation employing the

Smagorinsky [20] and dynamic Smagorinsky [84] models.

In 2012, Haga and Wang [37, 98] presented results from TGV simulations using the FR scheme at the 1st HIOCFD workshop. The FR schemes at $p = 2, 3, 4$ were successfully used by Haga and Wang on domains ranging from 64^3 to 96^3 (up to 32,768,000 DOFs at $p = 4$). Vermeire, Nadarajah and Tucker [64] (2014) examined the performance and suitability of the FR scheme for turbulent simulations on the Comte–Bellot–Corsin experiment, the TGV, and turbulent channel flow.

Recently, Bull and Jameson [9, 70, 71] (2014, 2015) performed TGV simulations using schemes from a family of energy-stable flux reconstruction (ESFR) schemes developed at Stanford University. They conducted simulations on hexahedral [9] and tetrahedral meshes [71]. In their paper [9], Bull and Jameson compared two new FR schemes (called optimal ESFR and optimal FR) developed by Asthana and Jameson [72] (2015), which are optimized for wave dissipation and dispersion properties, to the nodal discontinuous Galerkin (FR-DG) and spectral difference methods (FR-SD) recovered via the ESFR method. They found that the optimal ESFR scheme performed nearly identically to the FR-DG, whereas the optimal FR scheme tested was as stable as, but more accurate than, the FR-SD and FR-DG schemes. In their work, they successfully demonstrated that the FR scheme has low numerical dissipation and accurately reproduces the turbulent energy cascade on relatively coarse grids. Moreover, they reported that all schemes at higher than fifth-order exhibit instabilities at low mesh resolutions.

Despite that the performance of the FR scheme was quite thoroughly demonstrated earlier by Haga et al., Vermeire et al. and Bull et al., performing simulations of the TGV problem is still useful. The TGV simulations are important for the validation of computational fluid dynamics codes, and they are particularly useful during research into FR, as newly developed features can be easily tested and evaluated.

4.2 Numerical Setup

We follow the guidelines for the computational setup from the 1st and 2nd HIOCFD workshops for numerical simulations presented in this chapter.

4.2.1 Geometry and Initial Condition

The flow is computed within a periodic square box of dimension $0 \leq (x, y, z) \leq 2\pi L$, where L is the characteristic length of the box. The initial field is given by the following functions:

$$u_0(x, y, z) = V_0 \sin\left(\frac{x}{L}\right) \cos\left(\frac{y}{L}\right) \cos\left(\frac{z}{L}\right), \tag{4.1}$$

$$v_0(x, y, z) = -V_0 \cos\left(\frac{x}{L}\right) \sin\left(\frac{y}{L}\right) \cos\left(\frac{z}{L}\right), \tag{4.2}$$

$$w_0(x, y, z) = 0, \tag{4.3}$$

$$p_0(x, y, z) = p_\infty + \frac{\rho_0}{16} \left(\cos\left(\frac{2x}{L}\right) + \cos\left(\frac{2x}{L}\right) \right) \left(\cos\left(\frac{2z}{L}\right) + 2 \right). \tag{4.4}$$

The flow is governed by the three-dimensional compressible Navier–Stokes equations with constant physical properties. The compressible fluid is a perfect gas with a constant ratio of specific heats $\gamma = c_p/c_v = 1.4$ and Prandtl number $Pr = \mu c_p/\kappa$ set to 0.71, where c_p and c_v are the heat capacities at constant pressure and volume, respectively, μ is the dynamic viscosity and κ is the heat conductivity. Simulations are carried out with a low Mach number set to $M_0 = V_0/c_0 = 0.1$, where c_0 is the speed of sound corresponding to the temperature $T_0 = p_0/R\rho_0$. We consider the uniform initial temperature field $T = T_0$; then, the initial density field is taken as $\rho = p/RT_0$. The Reynolds number of the flow is set to 1600 and is prescribed by adjusting the viscosity. All the quantities involved in the study are assumed dimensionless using L, V_0 and ρ_0.

The domain consists of a cubic box with periodic boundary conditions applied on all faces. Meshes are considered Cartesian with equal grid spacing composed of hexahedral elements. The TGV simulations are performed on meshes involving 64^3, 128^3, 192^3 and 256^3 DOFs, denoted as coarse, medium coarse, medium and fine, respectively. The maximum

resolution of 256^3 DOFs seems often to be sufficient to represent the main characteristics of the flow (see [93]). Figures Figure 4.1a and b show an example of the fine domain with solution points shown in the bottom right quadrant and initial condition at $t = 0$ visualized by iso-surfaces of the z-component of the vorticity. The computational domains are summarized in Table 4.1.

(a): Periodic domain (b): z-vorticity at $t^* = 0$

Figure 4.1: TGV simulation: (a) Periodic domain with SP shown in bottom right quadrant (256^3 DOFs), (b) z-component of the vorticity shown at $t^* = 0$.

Table 4.1: Computational domains employed in the FR computations of the TGV problem.

solution order	hexahedral elements	DOFs	solution order	hexahedral elements	DOFs
$p = 1$	32^3	64^3	$p = 2$	21^3	63^3
	64^3	128^3		42^3	126^3
	96^3	192^3		64^3	192^3
	128^3	256^3		85^3	255^3
$p = 3$	16^3	64^3	$p = 4$	13^3	65^3
	32^3	128^3		25^3	125^3
	48^3	192^3		38^3	190^3
	64^3	256^3		51^3	255^3
$p = 5$	11^3	66^3	$p = 7$	8^3	64^3
	21^3	126^3		16^3	128^3
	32^3	192^3		24^3	192^3
	43^3	258^3		32^3	256^3

4.2.2 Temporal Evolution

A third-order three-stage TVD Runge–Kutta explicit method is used for time stepping. Computational domains are composed of regular hexahedral elements and the explicit scheme is preferred in this case, as it has considerably lower memory requirements at fine resolutions than implicit methods. The non-dimensional time step is set to $\Delta t^* = 4.5 \times 10^{-4}$; this value is comparable with the literature [99]. This time step is small enough that lowering it does not affect our findings, since the main objective is to observe the effects of the spatial discretization on the solution. This time step corresponds to a range of the Courant numbers (CFL) between 0.07 and 1.5.

The duration of the computation is set to $t^* = 20$. The simulation starts from large vortices, which immediately begin to evolve and interact with each other. At approximately $t^* = 7$, small structures of high-vorticity start to appear in the flow field. The most important region is a peak of the dissipation with the smallest turbulent structures, which occurs approximately at $t^* = 9$. After this peak, the fully developed turbulent flow starts to decay quickly. The flow evolving in time can be seen in Figure 4.2, where the solution on the medium mesh (192^3) for $p = 4$ is visualized using iso-surfaces of pressure colored by the vorticity magnitude at several simulation times.

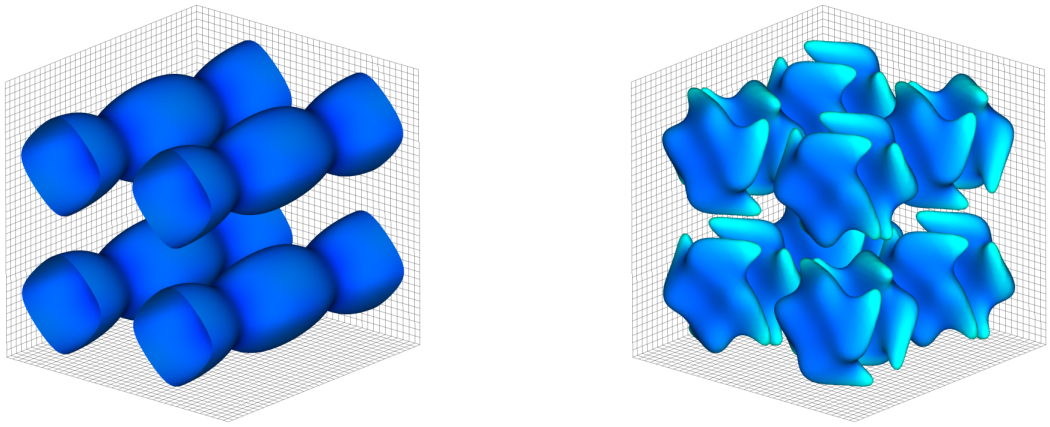

(a): $t^* = 0$, initial (b): $t^* = 3$, inviscid

Figure 4.2: TGV solution on the medium mesh (192^3 DOFs) for $p = 4$ depicting the evolution of the flow field using iso-surfaces of pressure (0.99) colored by the vorticity magnitude (0:10).

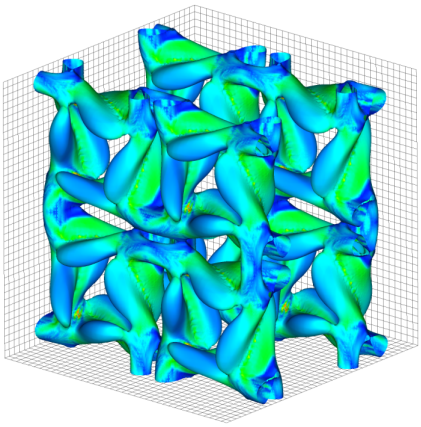

(a): $t^* = 5$, vortex roll-up

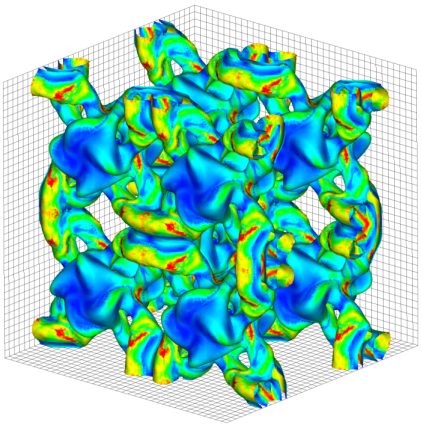

(b): $t^* = 7$, structure changes

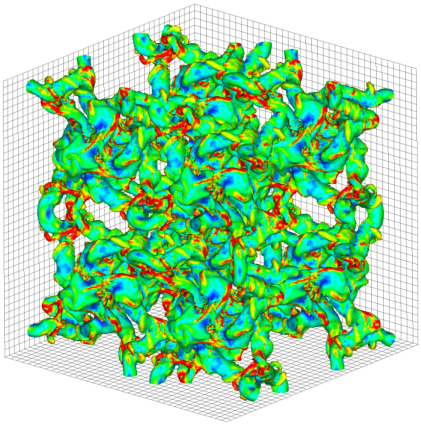

(c): $t^* = 9$, dissipation peak

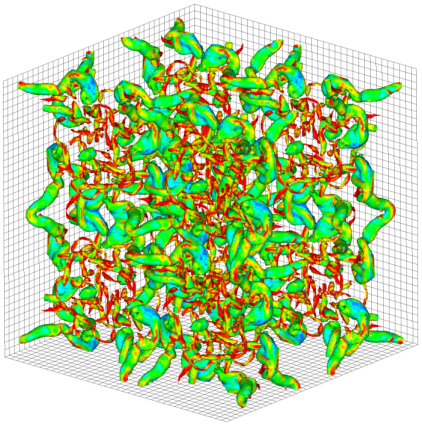

(d): $t^* = 11$, fully turbulent

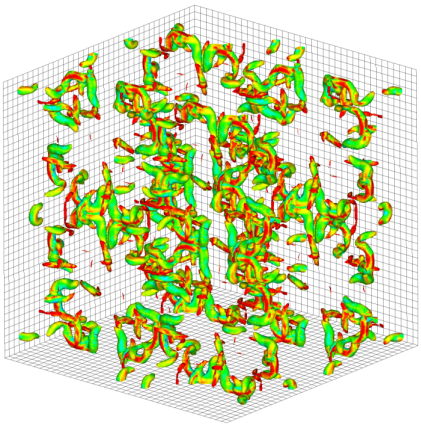

(e): $t^* = 13$, turbulent decay

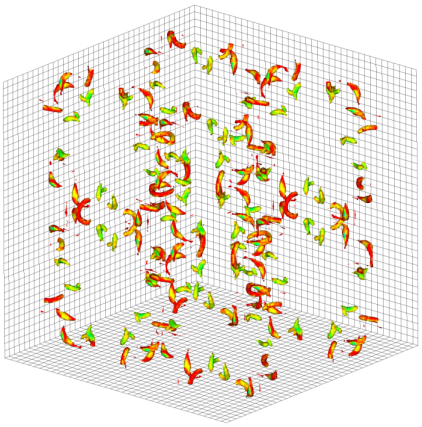

(f): $t^* = 15$, turbulent decay

Figure 4.3: Continue of Figure 4.2: TGV solution on the medium mesh (192^3 DOFs) for $p = 4$.

4.2.3 Diagnostics

To analyze the results, several diagnostic quantities related to the turbulent motion are computed. The quantities are averaged in space over a volume V, and they are computed from the flow as it evolves in time. Firstly, the mean turbulent kinetic energy E_k (also named TKE in the literature) is given by

$$E_k = \frac{1}{\rho_0 V} \int_V \frac{1}{2} \rho \mathbf{u} \cdot \mathbf{u} dV, \tag{4.5}$$

where $\mathbf{u}$ is the velocity vector.

We can obtain the temporal evolution of the kinetic energy dissipation rate from the kinetic energy as

$$\epsilon_1 = \epsilon(E_k) = -\frac{dE_k}{dt}, \tag{4.6}$$

where the temporal derivative is calculated using second-order finite differences.

The temporal evolution of the mean enstrophy $\mathcal{E}$ is computed as

$$\mathcal{E} = \frac{1}{\rho_0 V} \int_V \frac{1}{2} \rho \boldsymbol{\omega} \cdot \boldsymbol{\omega} dV, \tag{4.7}$$

where $\boldsymbol{\omega}$ is the vorticity vector.

It can be shown that for an incompressible flow ($\rho = \rho_0$) or a low Mach number flow with negligible compressible effects, the dissipation rate is related to the mean enstrophy $\mathcal{E}$ by a constant and is equal to

$$\epsilon_2 = \epsilon(\mathcal{E}) = 2 \frac{\mu}{\rho_0} \mathcal{E}. \tag{4.8}$$

These volume-integrated quantities—the kinetic energy and enstrophy—are useful, as they allows us to evaluate the quality of the solution and reveal inaccuracies in the discretization of the gradients by the scheme employed. The kinetic energy dissipation rate ϵ_2 computed from the enstrophy $\mathcal{E}$ represents the dissipation due to the vorticity. Ideally, when using a method that is not numerically dissipative, the directly computed dissipation rate $\epsilon(E_k)$ and the vorticity-based dissipation rate $\epsilon(\mathcal{E})$ should be equivalent.

For qualitative comparisons of solutions, we plot the iso-surfaces of the vorticity magnitude, the iso-surfaces of the pressure and the positive values of the Q-criterion [100].

4.3 Results at $Re = 1600$

In this section, we present and discuss results from the TGV simulations at $Re = 1600$. Simulations are carried out with degree $p = 1, 2, 3, 4, 5, 7$ polynomials. Solutions from the implicit large-eddy simulation approach (without an explicit sub-grid model) are compared to those obtained with the large-eddy simulation using the wall-adapting local eddy-viscosity (WALE) model. The results are compared to the reference solution computed using a pseudo-spectral method on a 512^3 mesh by Carton de Wiart et al. [94]. This reference solution is denoted as 'spectral' later in the text. The vortical structures are compared to results from Beck and Gassner [95] and Bull and Jameson [70].

4.3.1 Effect of the Polynomial Order on Solution

Figure 4.4 compares the evolution of the mean turbulent kinetic energy E_k, dissipation rate ϵ, and enstrophy $\mathcal{E}$ on a medium coarse mesh (128^3 DOFs) and fine mesh (256^3 DOFs) at $p = 1, 2, 3, 4, 5$, corresponding to second- to sixth-order accuracy. The reference spectral solution computed by Carton de Wiart et al. [94] on a 512^3 DOFs mesh is plotted as red circles. Figures 4.4a and b show the evolution of E_k. On both meshes, E_k computed at $p = 1$ deviates from the reference solution. Although there is a noticeable improvement with a higher mesh resolution, E_k decaying faster indicates that the numerical error introduced by the linear approximation of the solution dominates the behavior of the second-order scheme. On both meshes, the prediction for E_k significantly improves as the polynomial order increases. The calculated E_k matches the reference solution well in both well-resolved and under-resolved scenarios at $p > 1$.

Figures 4.4c and d show the evolution of the directly computed dissipation rate $\epsilon(E_k)$. At $p = 1$ on both meshes, $\epsilon(E_k)$ grows fast at the early phase of the simulation, where the convective phenomena are predominant. As the polynomial order increases, $\epsilon(E_k)$ gets closer to the reference solution. The largest discrepancies are expected at later times when the vortex core steepens into a high gradient, as the numerical dissipation significantly reduces the sharpness of the approximated velocity derivatives [99]. Figures 4.5a and b are a closer look at the peak dissipation rates $\epsilon(E_k)$ at $7 < t^* < 12$. Near $t^* = 9$, the peak of $\epsilon(E_k)$ is slightly underpredicted for all p on a coarser mesh, whereas $\epsilon(E_k)$ reasonably matches the reference solution on a finer mesh at $p = 3, 4, 5$. At $p = 5$ on both meshes,

oscillations are noticeable near the peak. The occurrence of these oscillations was reported by Gassner and Beck [95, 96] and Bull and Jameson [9, 70]. Gassner and Beck used a high-order DGSEM, whereas Bull and Jameson examined schemes from the FR family. In their paper, Bull and Jameson suggested that the origin of those oscillations is from large variations in the high-order polynomials within each element, and that the TGV flow, which has anti-symmetry in all three coordinate directions, may cause those variations to add up [70].

As expected by the previous statement, oscillations are significantly lower on a finer mesh (Figure 4.5a) than those on a coarser mesh (Figure 4.5b). This is due to the flow structures, which are represented with high-order polynomials within smaller elements. Section 4.3.2 presents the results computed on a coarse mesh (64^3). These coarse simulations at $p = 7$ suffered from instability. Thus, it seems that direct use of high-order polynomials for severely under-resolved simulations is not possible without employing some stabilizing mechanism. In their paper, Gassner and Beck [96] successfully used the over-integration stabilization technique for their simulations at $p = 7$ and $p = 15$. In the next section, we discuss the effect of the implicit modeling of the sub-grid scale turbulence on the solution and whether it can enhance the stability of the calculation.

Figures 4.4e and f show the evolution of the vorticity-related dissipation rate $\epsilon(\mathcal{E})$. Figures 4.5c and d show details of the solution near the peak. Recall that the directly computed dissipation rate $\epsilon(Ek)$ and the vorticity-based dissipation rate $\epsilon(\mathcal{E})$ should be equivalent in an ideal case. Thus, the discrepancy between $\epsilon(Ek)$ and $\epsilon(\mathcal{E})$ provides an additional valuable insight into how well the employed scheme works. On a coarser mesh, $\epsilon(\mathcal{E})$ gets closer to the reference solution as the polynomial order p increases. However, regardless of the polynomial order, the dissipation rate computed from the enstrophy ($\epsilon(\mathcal{E})$) is significantly lower than the dissipation rate directly computed from the kinetic energy ($\epsilon(E_k)$). On the other hand, the prediction improves with grid resolution and $\epsilon(\mathcal{E})$ approaches the correct levels on a finer mesh. The results on a fine grid at $p = 3$ or higher agree well with the reference solution. On the other hand, the results on a medium coarse grid—employed to demonstrate the effects on the under-resolved turbulence—show that only $p = 5$ achieves a reasonable compliance with the reference solution. This indicates that there is in the simulations another source of dissipation than just the dissipation due to the turbulence, and its effect is more intense at low resolutions. A significant part of the discrepancy originates in the numerical dissipation of the FR scheme. Other secondary sources could arise from the temporal discretization error and the effects of the compressibility.

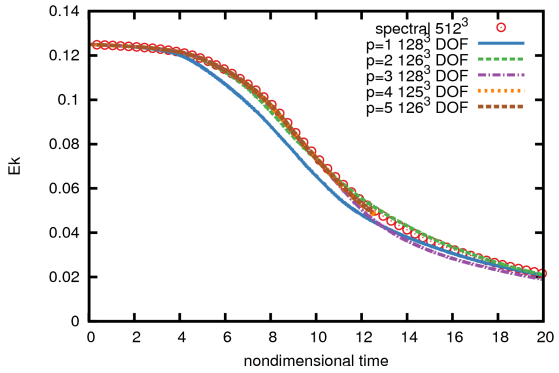

(a): E_k, 128^3 DOFs

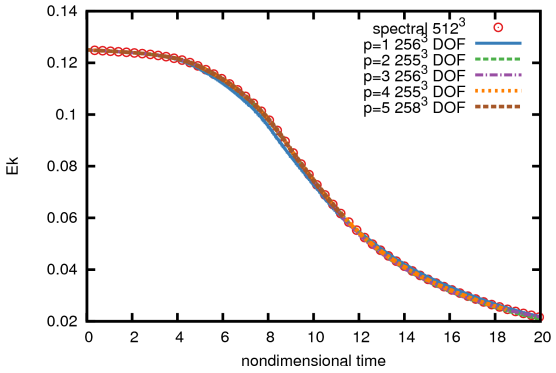

(b): E_k, 256^3 DOFs

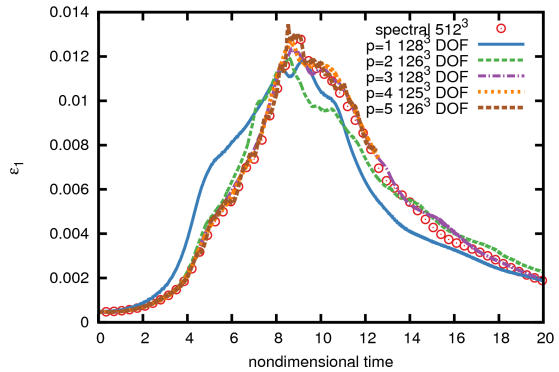

(c): $\epsilon(E_k)$, 128^3 DOFs

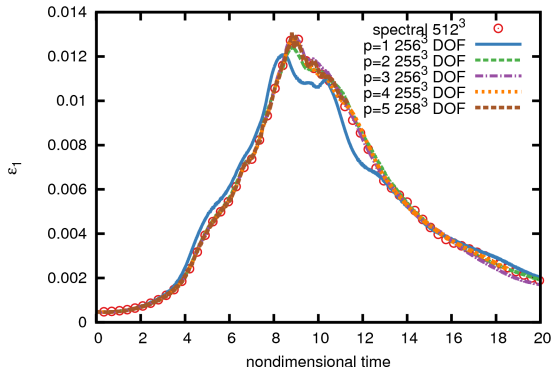

(d): $\epsilon(E_k)$, 256^3 DOFs

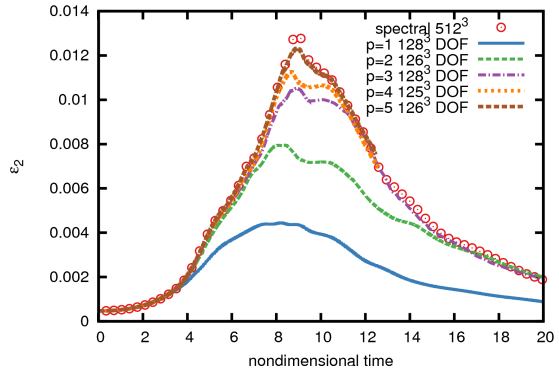

(e): $\epsilon(\mathcal{E})$, 128^3 DOFs

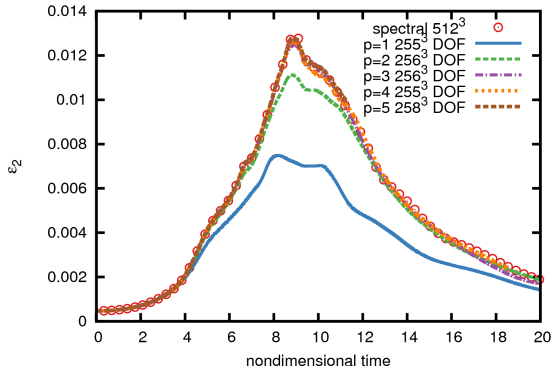

(f): $\epsilon(\mathcal{E})$, 256^3 DOFs

Figure 4.4: TGV solution on 128^3 and 256^3 DOFs meshes computed for all polynomial orders.

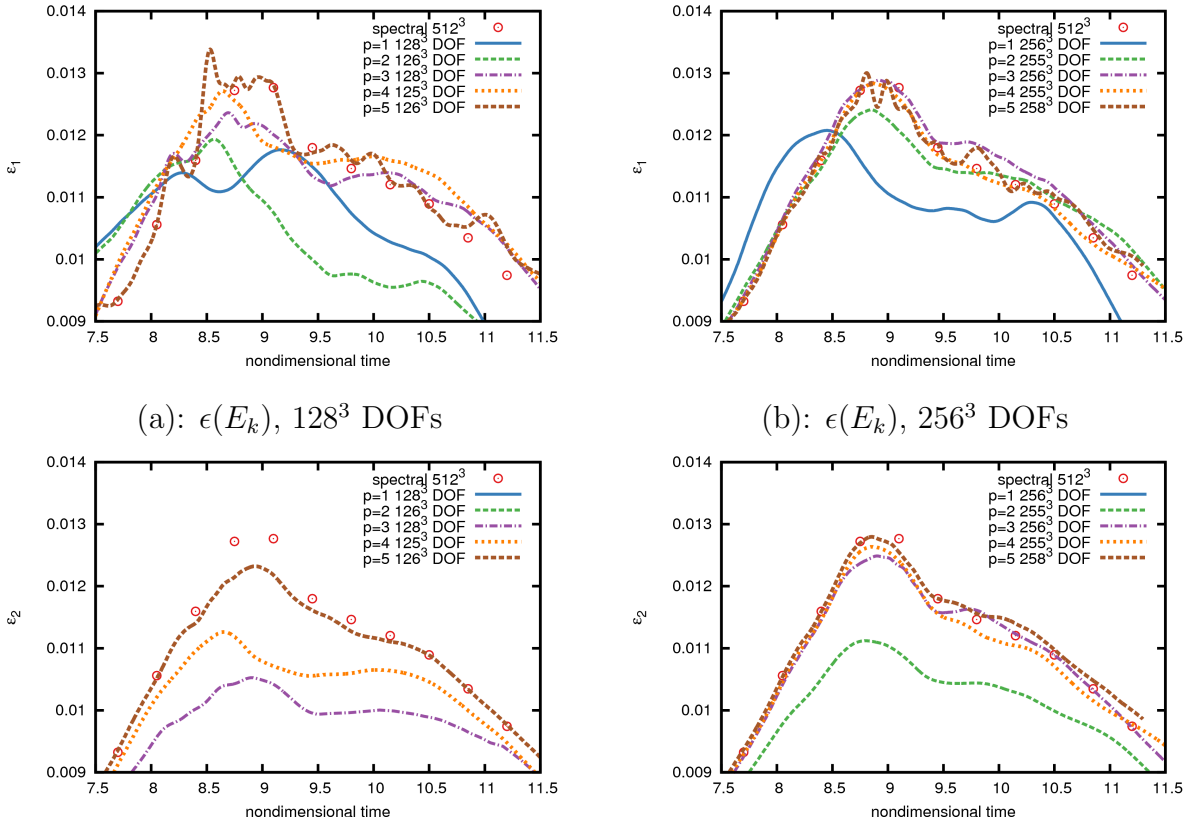

(a): $\epsilon(E_k)$, 128^3 DOFs

(b): $\epsilon(E_k)$, 256^3 DOFs

(c): $\epsilon(\mathcal{E})$, 128^3 DOFs

(d): $\epsilon(\mathcal{E})$, 256^3 DOFs

Figure 4.5: Detail of the TGV solution on 128^3 and 256^3 DOFs meshes computed for all polynomial orders.

Figures 4.6 and 4.7 shows the TGV solution ($0 \leq x, y, z \leq \pi$) at $p = 1$ and $p = 3$ for 64^3, 128^3, 192^3, and 256^3 DOFs using iso-surfaces of the Q-criterion at time $t^* = 8$. The solution at $p = 1$ is shown in the left column. They are similar in shape compared to the $p = 3$ solution in the right column, but only very large structures are captured by the second-order scheme at all mesh resolutions. With higher polynomial order comes a significant improvement, and large-scale structures are complemented by much smaller structures. On a 64^3 DOFs mesh at $p = 3$, the small-scale structures seem to be captured, but the solution seems to be blurred and jagged because there is insufficient resolution.

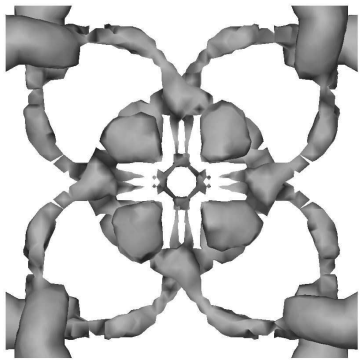

(a): $p = 1$, 64^3 DOFs

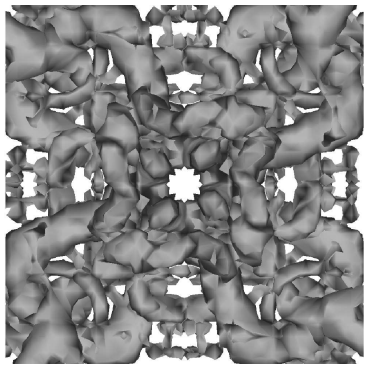

(b): $p = 3$, 64^3 DOFs

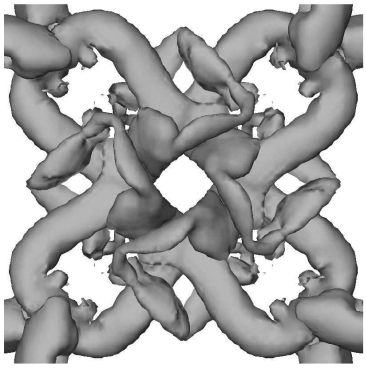

(c): $p = 1$, 128^3 DOFs

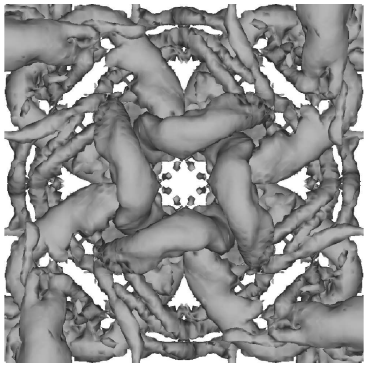

(d): $p = 3$, 128^3 DOFs

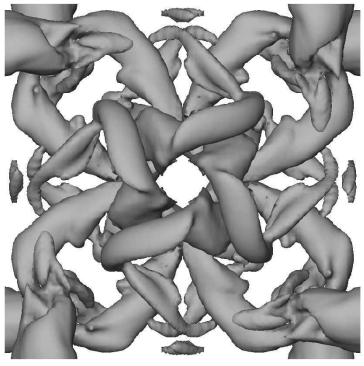

(e): $p = 1$, 192^3 DOFs

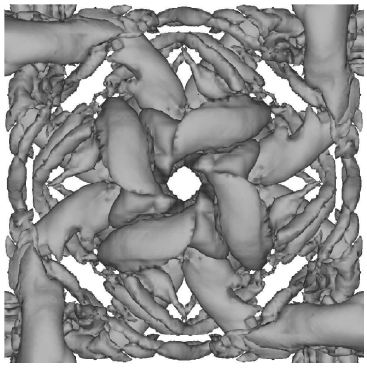

(f): $p = 3$, 192^3 DOFs

Figure 4.6: TGV solution at $p = 1$ compared to $p = 3$ on the coarse (64^3 DOFs), medium coarse (128^3 DOFs), and medium meshes (192^3 DOFs).

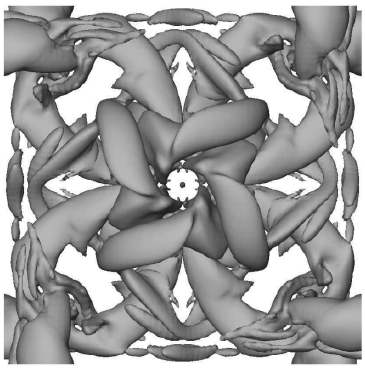

(a): $p = 1$, 256^3 DOFs

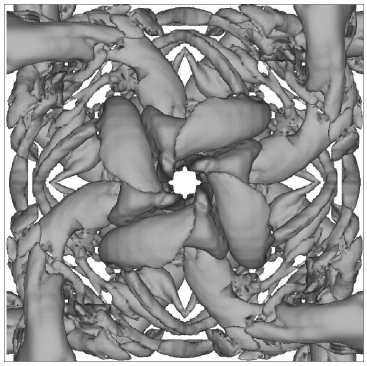

(b): $p = 3$, 256^3 DOFs

Figure 4.7: TGV solution at $p = 1$ compared to $p = 3$ on the fine (256^3) mesh.

Figure 4.8 shows the details of the vortices computed on 256^3 DOFs meshes at $p = 1, 2, 3, 4, 5$ compared to each other. $p = 2$ shows the poorest performance among the presented cases. The solutions for the other polynomials $p > 2$ seem to be almost identical, with captured large- and small-scale structures. In Figure 4.9, the TGV solution at $p = 3$ on a 256^3 DOFs mesh is compared to DGSEM at $p = 3, 15$ on a 256^3 DOFs mesh by Beck and Gassner [95] and DG recovered via FR at $p = 3$ on a 256^3 DOFs mesh by Bull and Jameson [70]. The structures are almost identical.

In this section, the effect of the polynomial order on the solution of the TGV using the FR scheme was investigated. We can summarize the main findings as follows:

- Low polynomial orders $p = 1, 2$ show excessive numerical dissipation, which has an impact on the accuracy of predictions.
- Predictions improve as the polynomial order increases, especially on coarse meshes.
- At high polynomial orders $p = 5, 7$, stronger instabilities appear in the solution as the mesh resolution decreases.
- $p = 3, 4$ show a good balance between stability and performance.
- For the practical use of higher polynomial orders, a stabilizing technique must be employed.

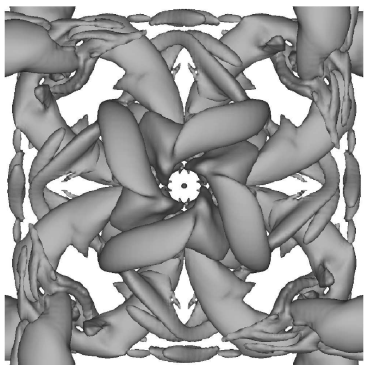

(a): $p = 1$

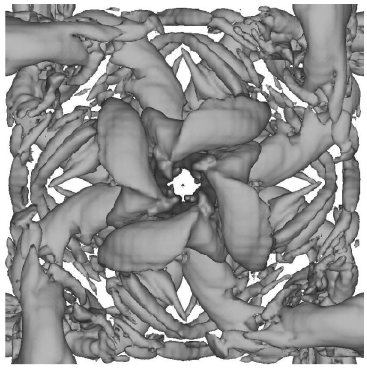

(b): $p = 2$

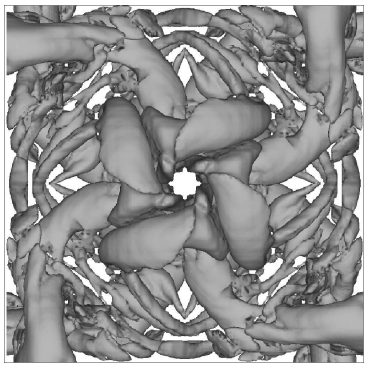

(c): $p = 3$

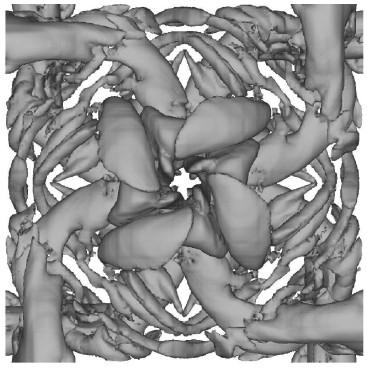

(d): $p = 4$

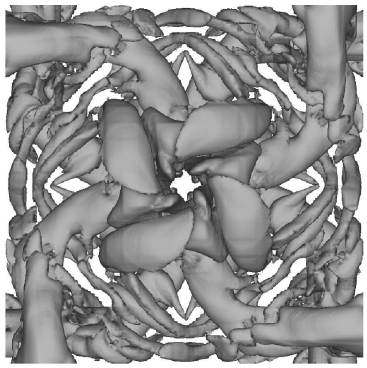

(e): $p = 5$

Figure 4.8: TGV solution on a fine mesh (256^3 DOFs) for $p = 1, 2, 3, 4, 5$ depicting the vortex structure at $t^* = 8$ using iso-surfaces of Q-criterion $Q = 1.5$.

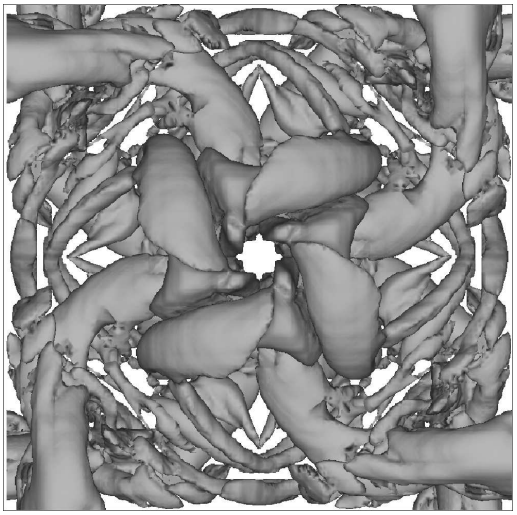

(a): $p = 3$, FR present study

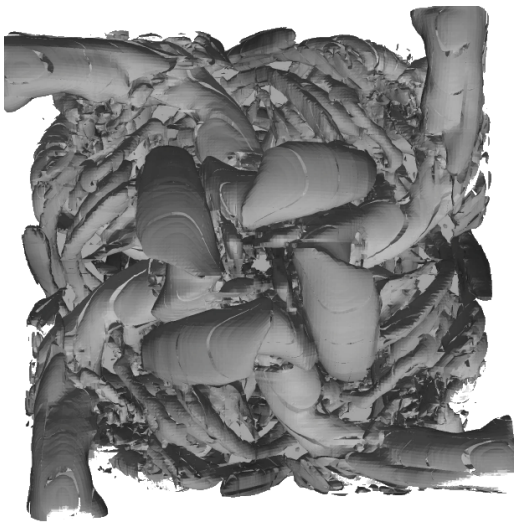

(b): $p = 3$, FR Bull and Jameson [70]

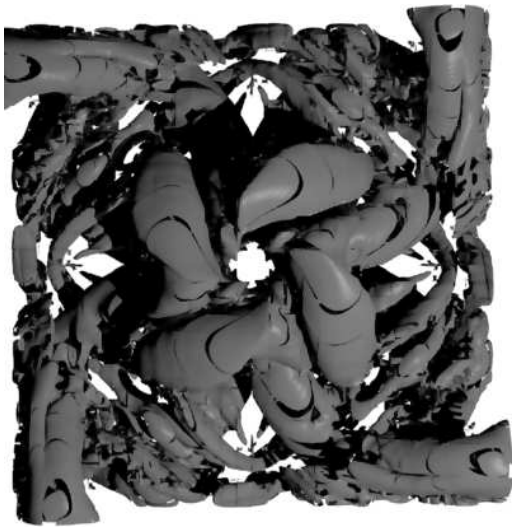

(c): $p = 3$, DGSEM Beck and Gassner [95]

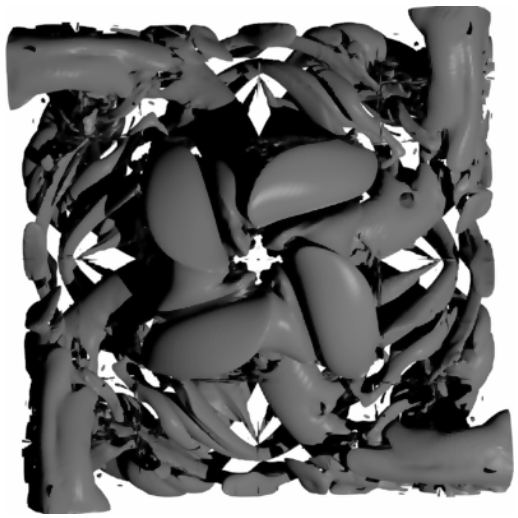

(d): $p = 15$, DGSEM Beck and Gassner [95]

Figure 4.9: TGV solution on the fine mesh (256^3 DOFs) for $p = 3$ depicting the vortex structure at $t^* = 8$ using iso-surfaces of Q-criterion $Q = 1.5$ compared to $p = 3$ solutions using FR-DG by Bull and Jameson [70] and $p = 3, 15$ DGSEM by Beck and Gassner [95].

4.3.2 Comparison of LES and ILES

In this section, implicit and explicit SGS modeling using the WALE model proposed by Nicoud and Ducros [83] is investigated within the FR framework at several polynomial orders on coarse to fine meshes, covering under-resolved to well-resolved cases. In the previous Section 4.3.1, solutions without any explicit modeling of the SGS turbulence agreed well with the reference spectral solution. Thus, this gives us some confidence in the method developed with the FR for implicit large-eddy simulations. However, the addition of an explicit SGS is examined for two reasons. We investigate firstly, the effect of additional dissipation introduced through the SGS model on the solution, and secondly, the effect of the SGS modeling on the stability of the numerical computations at high polynomial orders $p = 5, 7$ on coarse meshes.

Figures 4.11a,b, 4.11c,d, and 4.11e,f compare the evolution of E_k, the directly computed dissipation rate $\epsilon(E_k)$, and the vorticity-based dissipation rate $\epsilon(\mathcal{E})$, respectively. The solutions are presented for ILES and LES computed using polynomial orders $p = 1, 2, 3, 4, 5$ on a coarse mesh (64^3 DOFs). This 64^3 DOFs mesh represents a severely under-resolved case, where the effects of the SGS modeling should be highlighted. In general, the sub-grid model solutions are similar to the cases without a sub-grid model. However, it seems that additional dissipation added from the SGS model slightly alters the solution for all polynomial orders. Recall that the simulations are initialized from large vortices (see Figure 4.2a), and mainly there are interactions between large vortical structures until $t^* = 5$ to 7 (see Figure 4.3a and b). Despite that small-scale structures are not present, as the fully turbulent flow has not been developed yet, the sub-grid model produces dissipation, which adds to the overall dissipation. The careful reader may notice how the $\epsilon(E_k)$ curves at $p = 2, 3, 4, 5$ coincide in the SGS model case until $t^* = 5$. This particular result may indicate that the dissipation of the sub-grid model dominates the numerical dissipation from the discretization using $p = 2$ or higher at the early stage of the simulation. Nevertheless, as soon as the flow develops into a fully turbulent flow at approximately $t^* = 7$, the sub-grid model seems to work correctly and the kinetic energy dissipation rates become closer to the reference spectral solution as the polynomial order increases.

However, since the eddy viscosity sub-grid models are inherently dissipative [85], it seems the turbulent structures are damped by the added dissipation, which results in lower levels of the enstrophy. Our finding are in agreement with those of DeBonis [97]. In his paper, DeBonis examined the effect of sub-grid models based on large-eddy simulation

employing the Smagorinsky [20] and dynamic Smagorinsky models [84], which are popular eddy viscosity sub-grid models. DeBonis reported that the sub-grid models add too much dissipation where the flow is not fully turbulent. They improve the solution near the peak dissipation rates, dissipate the resolved turbulent structures reducing the peak levels of vorticity, and increase the levels of numerical dissipation. Thus, it seems that the eddy viscosity sub-grid models are not the best choice for simulations over a long time interval, where an accurate representation of the decaying turbulence is needed. Figure 4.11 shows the TGV solution at $p = 3$ for 64^3 and 256^3 DOFs meshes computed with and without a sub-grid model. As expected, the effect of the sub-grid model is weaker at higher resolutions, when the resolved scales are much closer to the Kolmogorov scale.

On the other hand, the added dissipation from the sub-grid model seems to stabilize the numerical computations—to some degree—at high polynomial orders. In the previous section, it was shown that instabilities appears at high polynomial orders $p = 5, 7$ in the solution, and they get stronger as the mesh resolution decreases. These instabilities reached a critical level for polynomial order $p = 7$, and they destabilized the solution on coarser meshes (64^3 and 128^3 DOFs) at approximately $t^* = 7$. Simulations on the same meshes using a sub-grid model exhibit enhanced numerical stability. This can be seen in Figure 4.10, where $\epsilon(E_k)$ and $\epsilon(\mathcal{E})$ computed without sub-grid modeling on 64^3 and 128^3 DOFs meshes are compared to those computed with the sub-grid model. On a coarse mesh at $p = 7$, the effect of added dissipation on $\epsilon(E_k)$ seems rather limited. Although, $\epsilon(E_k)$ passes the dissipation peak at $t^* = 9$, oscillations appear near the peak. Later, at time $t^* = 11$, the simulation diverges as well. On the other hand, the numerical stability significantly improves on a medium coarse mesh at $p = 7$. The originally unstable simulation, which diverged at time $t^* = 7$, is now stable over the whole calculation period.

Although we found that the TGV simulations without any explicitly modeled SGS turbulence outperformed simulations with SGS modeling, the positive effect on the numerical stability seems promising.

The eddy viscosity models have proven to be very useful for calculating turbulent flows in industrial settings (see [101] for reviews). In the next Chapter 5, we examine the performance of the FR scheme on a realistic aerospace application. In such setting, the WALE model produces comparable results to the case without any SGS model.

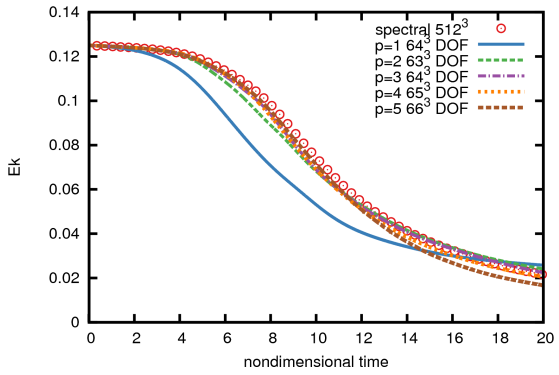

(a): ILES E_k

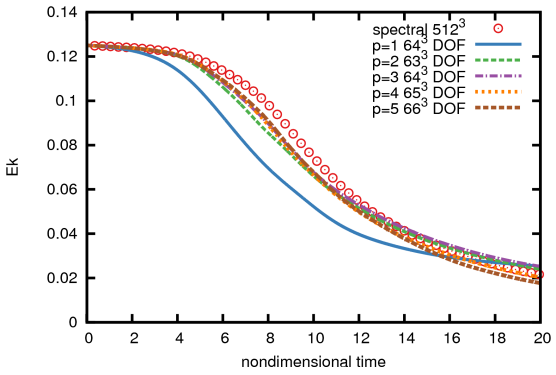

(b): LES E_k

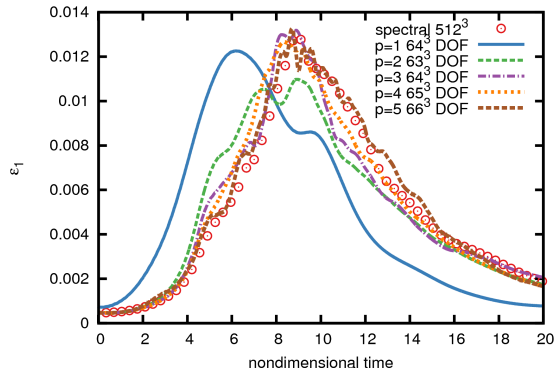

(c): ILES $\epsilon(E_k)$

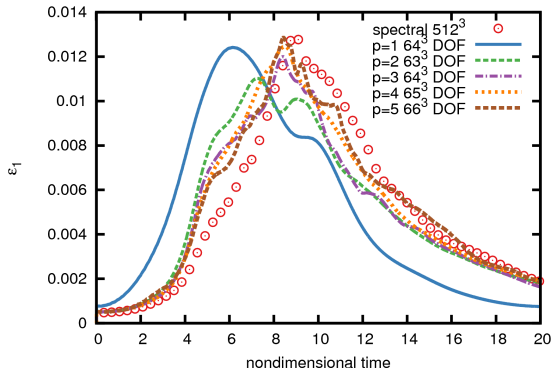

(d): LES $\epsilon(E_k)$

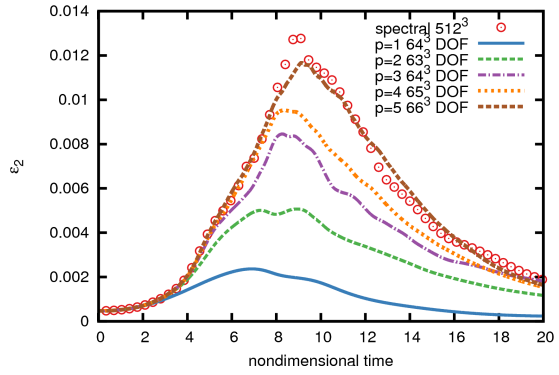

(e): ILES $\epsilon(\mathcal{E})$

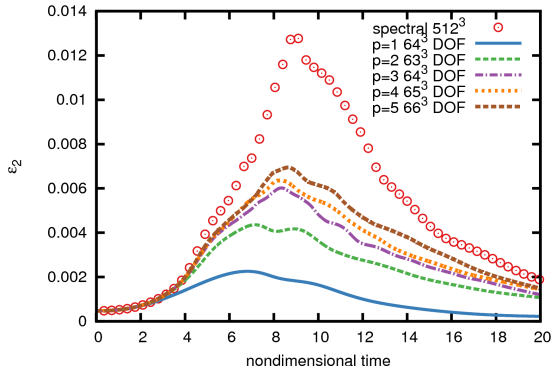

(f): LES $\epsilon(\mathcal{E})$

Figure 4.10: TGV solutions on a 64^3 DOFs meshes computed using ILES and LES.

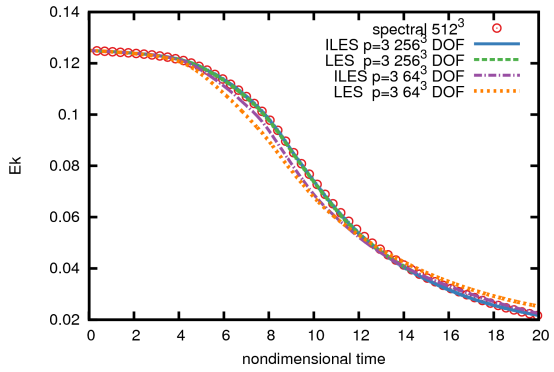

(a): E_k

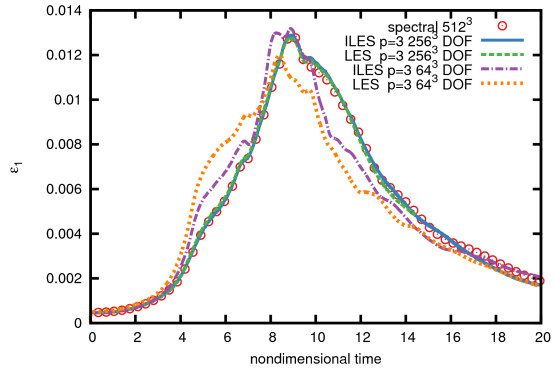

(b): $\epsilon(E_k)$

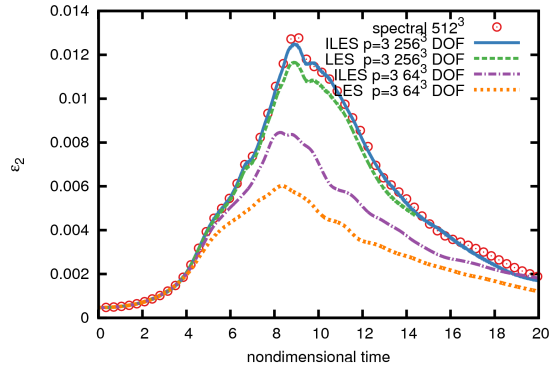

(c): $\epsilon(\mathcal{E})$

Figure 4.11: TGV solution at $p = 3$ on 64^3 and 256^3 DOFs meshes computed using ILES and LES.

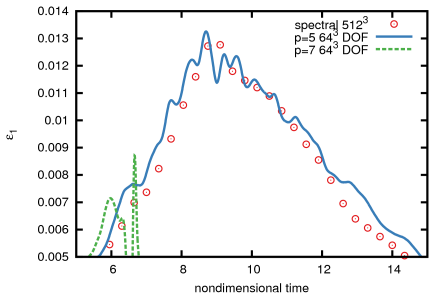

(a): ILES $\epsilon(E_k)$, 64^3 DOFs

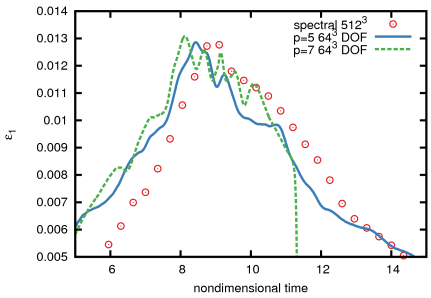

(b): LES $\epsilon(E_k)$, 64^3 DOFs

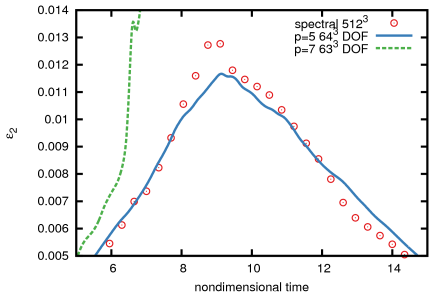

(c): ILES $\epsilon(\mathcal{E})$, 64^3 DOFs

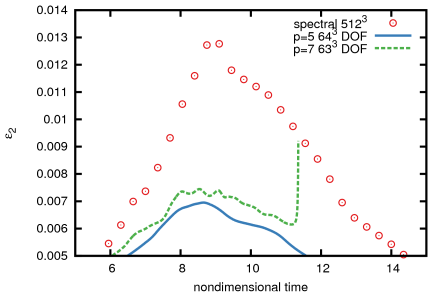

(d): LES $\epsilon(\mathcal{E})$, 64^3 DOFs

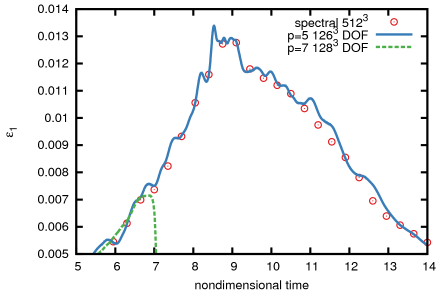

(e): ILES $\epsilon(E_k)$, 128^3 DOFs

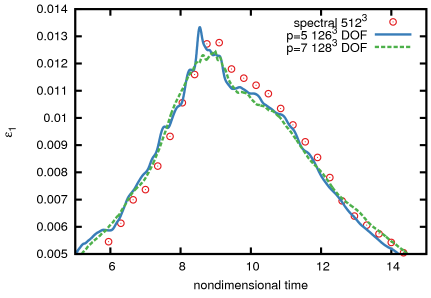

(f): LES $\epsilon(E_k)$, 128^3 DOFs

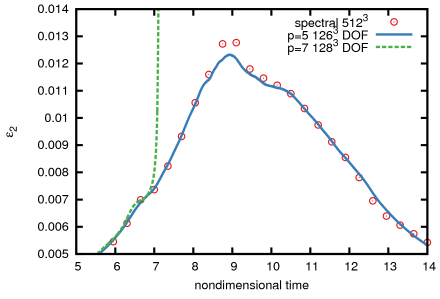

(g): ILES $\epsilon(\mathcal{E})$, 128^3 DOFs

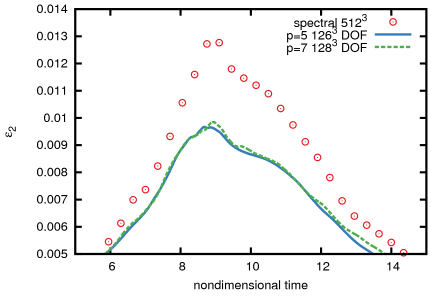

(h): LES $\epsilon(\mathcal{E})$, 128^3 DOFs

Figure 4.12: TGV solutions on a 128^3 DOFs mesh computed using ILES and LES at $p = 5$ and 7.

4.3.3 Calculation Cost

Figure 4.13 plots a semilog of the calculation cost using $p = 1, 2, 3, 4, 5$ FR schemes on mesh sizes ranging from 64^3 to 256^3 DOFs. The data are shown for the ILES setting. The calculation cost increases about 13–15% for LES with the SGS modeling. The vertical logarithmic axis shows the calculation cost expressed in work units for each iteration (for a definition, see Section 3.5), and the horizontal axis shows the length scale h defined as $1/\sqrt[3]{\text{nDOFs}}$ with nDOFs the total number of DOFs per equation. To give a better idea of the calculation cost, the simulation takes 28 single-CPU hours and 17 single-CPU hours at $p = 1$ and $p = 5$ on a 64^3 mesh, respectively. The simulations at $p = 1$ and $p = 5$ on a 256^3 DOFs mesh need 1795 single-CPU hours and 1067 single-CPU hours, respectively. We found a large difference of about 65% between $p = 1$ and $p = 5$ FR schemes. In other words, we obtained much more accurate results in a considerable shorter time at $p = 5$. Please note that we use a scientific code in this study. It seems it has a reasonable computational speed compared to other scientific codes. For example, Haga and Wang [98] presented the computational costs of the CPR code at the 1st HIOCFD workshop. Their FR code required 12.55 work units for each iteration on a fine mesh (256^3 DOFs) at $p = 3$. We achieved of 12.68 work units for each iteration.

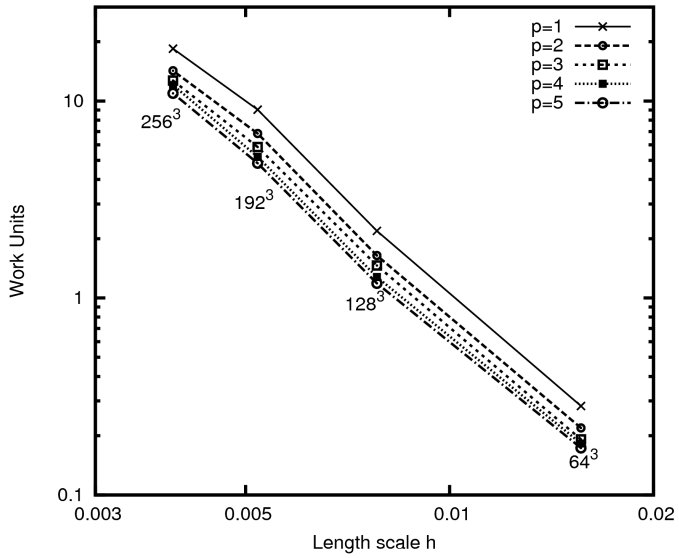

Figure 4.13: ILES TGV: calculation cost.

Chapter 5

Flow Around the SD7003 Wing at $Re = 60,000$

In this chapter are presented and discussed results from numerical simulations of transitional flow over a rectangular wing section with a Selig–Donovan low Reynolds number airfoil at $\alpha = 4°$, $8°$, and $Re = 60,000$ using high-order flux reconstruction scheme. Simulations are carried out with the degree $p = 1, 2, 3$ polynomials resulting in second-, third-, and fourth-order accurate FR schemes, respectively.

The flow around an airfoil at this condition is characterized by a laminar-separation bubble (LSB) that was first described in detail by Gaster [55] and discussed in previous Section 2.3. An accurate prediction of transitional flows by the numerical simulation requires the scheme with low numerical viscosity and low dispersion errors. Recently, the attempt to capture the complex flow stated above by high-order accurate and high-resolution schemes, together with the large-eddy simulation or the implicit large-eddy simulation without explicit sub-grid-scale eddy viscosity models, show remarkable successes to account for the transitional phenomena as well as the characteristic surface pressure and skin friction. However, the simulations are far from trivial and all employs state-of-the art numerical schemes and essential computer resources to capture transitional location, the turbulent statistics, and unsteady aerodynamic forces due to the fluctuation of separated shear layer.

For numerical simulations of the complex flow described above, a low Reynolds transitional flow around an SD7003 wing was proposed in the category of three-dimensional and difficult problems in the 1st and 2nd international workshops on high-order CFD methods (HIOCFD) held in 2012 and 2013 [37]. In the 3rd HIOCFD held in January 2015, the SD7003 wing test case was removed from the database of HIOCFD test cases. Possible reasons for removing the SD7003 case are quantitative discrepancies in separation, reattachment and transition locations, as well as in aerodynamic loads across the literature [102], the absence of DNS or additional experimental data for validation, and the fact that this case is quite computationally intensive, which makes it difficult to conduct grid resolution studies. Additional information about the 3rd HIOCFD can be found in the workshop website (https://www.grc.nasa.gov/hiocfd/). However, reports on solutions of this type of flow problem using methods achieving high-order accuracy are not only restricted to HIOFCD, but can be found in numerous other sources [[12]-[106]]. Literature sources which we will refer to later to are introduced in Section 5.1.

5.1 Literature Review

Catalano and Tognaccini [107] (2009) performed RANS simulations of the flow at Re = 60,000 around the SD7003 airfoil. They showed that the laminar separation bubbles can be detected by a RANS method without any particular treatment of the laminar–turbulent transition. However, the unsatisfactory performance of the $\kappa - \omega$ SST turbulence model employed in some cases led Catalano and Tognaccini [108] (2010) to propose a modification of the turbulence model so that it would correctly reproduce the wall-law velocity for attached flows of low Reynolds numbers. This model is called $\kappa - \omega$ SST-LR. In [106] (2010), Catalano and Tognaccini performed RANS with turbulence models $\kappa-\omega$ SST, $\kappa-\omega$ SST-LR, and LES using a numerical code based on second-order central differences in the stream-wise and wall-normal directions, and Fourier collocations in the span-wise direction. Their main conclusions are that flows at low Reynolds number and the laminar separation bubbles can be simulated by the RANS approach, but as the angle of attack increases and a converged solution is no longer obtained, then time-accurate URANS simulations need to be performed.

A high-order discontinuous Galerkin (DG) method for implicit large-eddy simulation was introduced by Uranga et al. [12, 17] (2009, 2011). Uranga has conducted two- and three-dimensional simulations at $\alpha = 4^\circ$ and Re = 10,000, 22,000, and 60,000, using third- and fourth-order DG schemes on unstructured tetrahedral meshes. Recently, ILES using the DG scheme have been conducted by Carton de Wiart and Hillewaert [11] (2012), Beck et al. [13] (2014), and Bassi et al. [103] (2015). Carton de Wiart and Hillewaert have conducted three-dimensional fourth-order accurate simulations at $\alpha = 4^\circ$ on unstructured mixed meshes composed of hexahedra and wedges. Beck et al. conducted fourth- and eighth-order accurate simulations at $\alpha = 8^\circ$ on unstructured hexahedral meshes. An over-integration approach has been used to achieve a stable simulation for eighth-order accurate simulation. Bassi et al. have performed ILES using fouth- and fifth-order DG schemes at $\alpha = 8^\circ$.

Galbraith and Visbal [14, 15] (2009, 2010) have conducted numerical simulations using the sixth-order accurate compact finite difference (CD) scheme with a high-order low-pass filter. They have used the overset grid approach and presented a comprehensive set of results, including various angles of attack and mesh resolutions. More recently, Garmann, Visbal, and Orkwis [16] (2012) conducted a comparative study of implicit and subgrid-scale-based large-eddy simulations. In their simulations, the time-mean flow or statistical quantities have not been significantly affected by the addition of the dynamic Smagorinsky model. Garmann and Visbal [109] (2013) conducted additional simulations at $\alpha = 4^\circ$, 8° on very fine meshes (up to 53.4 million DOFs) using CD scheme for the second HIOCFD.

Boom and Zingg [104] (2013) and Weide, Giangaspero, and Svärd [105] (2015) conducted ILES with high-order SBP-SAT (summation-by-parts spatial operators) finite difference (FD) schemes. Boom et al. have conducted simulations at $\alpha = 4^\circ$ and 8° using second- and fourth-order accurate code, while Weide et al. have used fifth-order accurate code to perform simulations at $\alpha = 8^\circ$.

Vermiere, Cagnone, and Nadarajah [63] (2013) presented some results for ILES using an FR scheme of turbulent and transitional flow over an SD7003 airfoil at $\alpha = 4^\circ$ and Re = 60,000. Preliminary fourth-order results showed good agreement with previous numerical and experimental studies. Skarolek and Miyaji [67] (2014) conducted three-dimensional simulations at $\alpha = 4^\circ$ and 8° using third- and fourth-order FR schemes on two structured hexahedral meshes. The laminar separation bubble and the transition process was predicted quite well with remarkable agreement with the reference data across the literature.

In 2015, Vermeire and Nadarajah [110] presented an adaptive implicit/explicit (IMEX) approach for use with high-order unstructured schemes. The algorithm was validated on two-dimensional unsteady laminar flow over the SD7003 airfoil at $\alpha = 4°$ and Re = 10,000.

Zhou and Wang [18] (2010) and Castonguay, Liang, and Jameson [19] (2010) have investigated the flow around the SD7003 wing using the spectral difference (SD) method. Both groups have conducted third- and fourth-order simulations at $\alpha = 4°$. Castonguay et al. have conducted simulations at Re = 10,000 and 60,000. In the work of Zhou et al., the vortex breakdown process and the transition mechanism are discussed.

5.2 Computational Methodology

We follow guidelines for the computational set-up from the 1st and 2nd HIOCFD for numerical simulations presented in this chapter.

5.2.1 Geometry and Mesh Generation

The Selig–Donovan low Reynolds number airfoil has a maximum thickness of 8.5% and maximum camber of 1.45% at the 35% of the chord. The wing section is created from the extended planar airfoil geometry with spanwise length set to $z/c = 0.2$. The original sharp trailing edge (TE) has been rounded, with a very small circular arc of radius $r/c \sim 0.0004$ to facilitate grid generation near the trailing edge. The SD7003 airfoil and wing section is shown in Figure 5.1. As shown later, the flow at this Reynolds number transitions to turbulence, and since the flow has a clearly visible three-dimensional nature, one can expect that important flow features cannot be captured by a two-dimensional simulation. This is confirmed by comparing the two- and three-dimensional results obtained on a grid with the same resolution in a span-wise plane. Figure 5.2 plots instantaneous contours of vorticity for two- and three-dimensional simulations. A strong robust vortex travels downstream to a trailing edge in the two-dimensional simulation, and this means that transition phenomena are not captured correctly if the three-dimensional effects are neglected.

Numerical simulations are conducted on two structured hexahedral O-grid domains. They differ in the number of SP in a circumferential direction on the upper surface of the wing. Mesh coordinates $(\xi \times \eta \times \zeta)$ are oriented such that ξ follows the spanwise direction, η

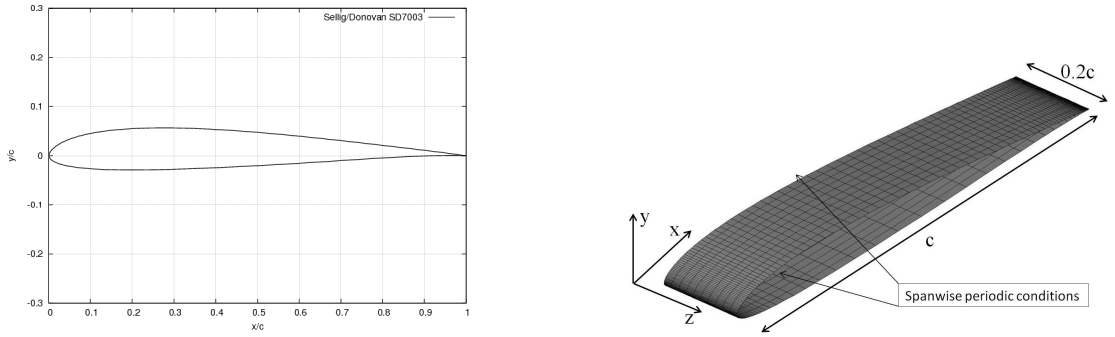

(a) (b)

Figure 5.1: Selig–Donovan SD7003 low Reynolds number airfoil (a) and wing section (b).

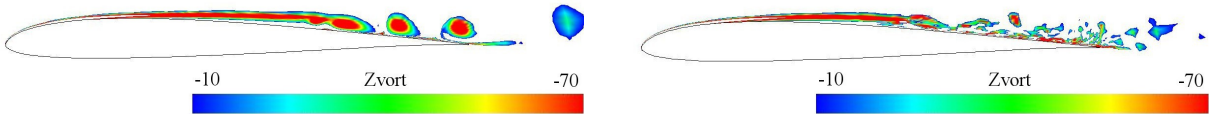

(a): 2D (b): 3D

Figure 5.2: Vorticity contours: comparison of 2D and 3D simulation.

traverses clockwise around the airfoil, and ζ is normal to the surface as shown in Figure 5.4a. Dimensions of a coarse domain expressed in terms of the number of cells in spanwise, circumferential, and radial direction are $7 \times 96 \times 24$. The mesh contains $16,128$ hexahedral cells, which give $129,024$ DOFs, $435,456$ DOFs, and $1,032,192$ DOFs for $p = 1, 2, 3$, respectively. Finer domain consists of $32,256$ hexahedral cells with dimensions $7 \times 192 \times 24$. This gives $258,048$ DOFs, $870,912$ DOFs, and $2,064,384$ DOFs for $p = 1, 2, 3$, respectively. Approximately 75 percent of solution points is located in the upper part of the O-grid domain, i.e., there are more solution points on the upper surface of the wing than on the lower surface. The first wall-bounded base grid cell lies in the viscous sublayer with approximately $y^+ = 2.5$. In Figure 5.3a and 5.4a is shown a base grid — defined as the mesh without added solution points— for coarse simulations. Figures 5.3b and 5.4b show the same grid with solutions points for $p = 3$. The computational domains are summarized in Table 5.1.

Table 5.1: Computational domains: present study

Case	p	mesh dimensions†	DOFs	Approximate distance between two high-order nodes calculated as size of an element divided by p				
				$(\Delta s/c)_{LE}$	$(\Delta s/c)_{TE}$	$(\Delta s/c)_{0.2}$	$(\Delta s/c)_{0.6}$	$(\Delta n/c)_{0.6}$
Coarse	1	$7 \times 96 \times 24$	129,024	0.0014	0.00022	0.018	0.022	0.00061
	2		435,456	0.0007	0.00011	0.009	0.011	0.00031
	3		1,032,192	0.00046	0.000073	0.006	0.0073	0.00020
Fine	1	$7 \times 192 \times 24$	258,048	0.0014	0.00022	0.012	0.010	0.00073
	2		870,912	0.0007	0.00011	0.006	0.005	0.00037
	3		2,064,384	0.00046	0.000073	0.004	0.0033	0.00024

$(\Delta s/c)$ - surface spacing in circumferential direction at leading edge (LE), trailing edge (TE) and x/c location

$(\Delta n/c)$ - normal spacing near the wall at x/c location

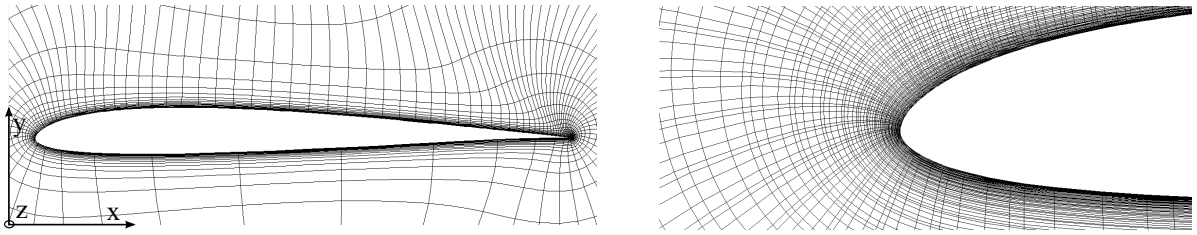

(a): base grid (b): solution points $p = 3$

Figure 5.3: Coarse mesh: (a) base grid with 16,128 hexahedral cells, (b) added solution points for $p = 3$ (1M DOFs)

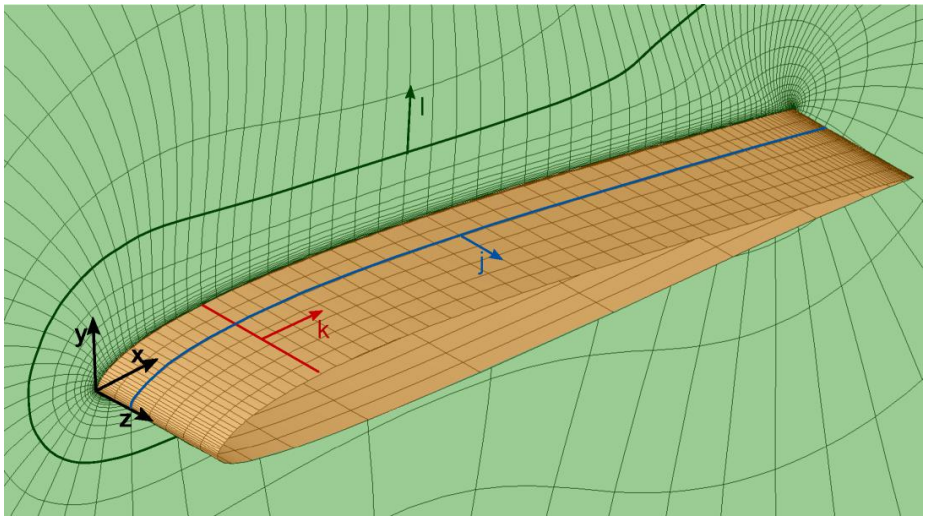

(a): base grid

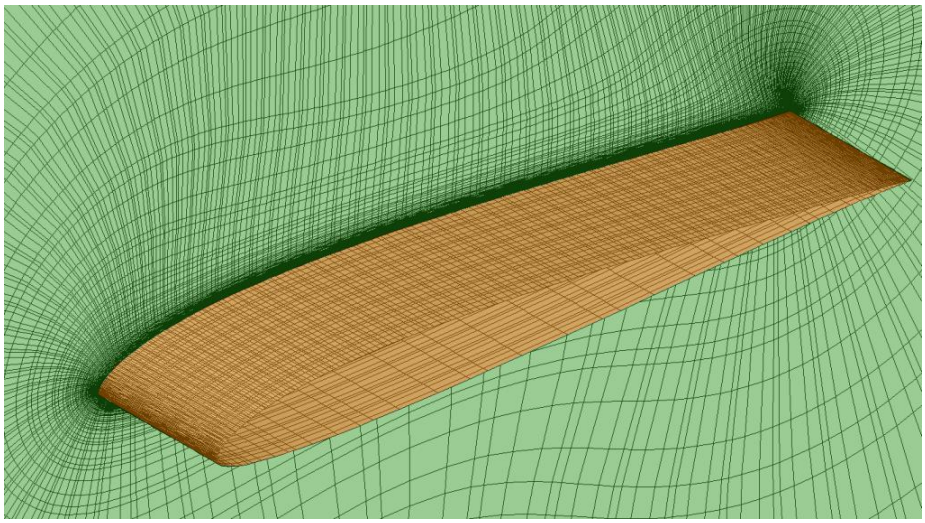

(b): $p = 3$ coarse [1M DOFs]

Figure 5.4: Coarse mesh: (a) base grid with 16,128 hexahedral cells, (b) added solution points for $p = 3$ (1M DOFs)

5.2.2 Initial Conditions

Simulations are carried out with a free-stream Mach number $M_\infty = 0.1$, with a constant ratio of specific heats $\gamma = 1.4$, and the Prandtl number set to 0.72. Boundary conditions (BC) follow the recommendations given by the HIOCFD committee. A no-slip isothermal BC condition $T_{wall}/T = 1.002$ is applied on the surface of the wing. A far-field boundary with a free-stream velocity condition is located approximately 100 chords away. The periodic boundary is along the spanwise (ξ) direction. Second- and third-order simulations are initiated from free-stream conditions. The fourth-order simulations are started from a developed state of third-order simulations to reduce the computational cost. Lagrange interpolation polynomials are used to obtain the initial fourth-order flow fields. Then, a continuous solution function $Q(\xi, \eta, \zeta)$ in a cell is constructed from N^3 discrete solutions $Q_{j,k,l}$ as follows:

$$Q(\xi, \eta, \zeta) = \sum_{l=1}^{N} \sum_{k=1}^{N} \sum_{j=1}^{N} \{P_{j,k,l}(\xi, \eta, \zeta) Q_{j,k,l}\}, \tag{5.1}$$

where

$$P_{j,k,l}(\xi, \eta, \zeta) = \left(\prod_{i=1, i=j}^{N} \frac{\xi - \xi_i}{\xi_j - \xi_i} \right) \cdot \left(\prod_{i=1, i=k}^{N} \frac{\eta - \eta_i}{\eta_k - \eta_i} \right) \cdot \left(\prod_{i=1, i=l}^{N} \frac{\zeta - \zeta_i}{\zeta_l - \zeta_i} \right). \tag{5.2}$$

5.2.3 Temporal Evolution

The non-dimensional implicit time step is set to $\Delta t^* = 0.0002$ for all simulations. This time step is based on physical considerations from Kolmogorov theory. We have followed the conclusions of Choi and Moin in [111], where they demonstrated that turbulence fluctuations could not be sustained in the DNS of a turbulent channel flow if the computational time step was near or larger than the Kolmogorov timescale. Therefore, the time step should be considerably lower than the timescale of the grid-resolved eddies for LES. In our study, a computational time step of 0.0002 is approximately 1 order lower than a relevant grid-resolved timescale. However, these assumptions are valid only for flows with high enough Reynolds number, according to Pope [34]. Therefore, we conducted a computational time-step study in Section 5.3.1 for validation. The time step set to $\Delta t^* = 0.0002$ is also comparable to the literature [11, 13, 15, 19]. Selected simulations are recomputed

with the TVD-RK3 scheme to confirm the equivalent flow solutions and the amount of speed-up by the explicit and implicit method by our code.

It is convenient to express the simulation time in so-called convective time units (CTUs). This is simply the time it takes for the flow to travel one chord length. A relation holds that 1 non-dimensional time unit equals 1 CTU. Since, the second- and third-order simulations are initiated from free-stream conditions, a numerical adjustment from an unphysical state with large variations in forces occurred about five CTUs with slow stabilization of the forces during next 10 CTUs. Therefore, to let the flow stabilize for a reasonably long period of time, the second- and third-order simulations run for 40–50 CTUs with all quantities of interest averaged during the last 15 CTUs. At first, the fourth-order simulations, which are started from a developed state of third-order simulations, are allowed to stabilize, then data for time mean solutions are collected every iteration at least over 8 CTUs. Selected variables, such as velocity and mean-squared fluctuations of u-, v-, and w-velocity, are recorded every tenth iteration to give enough samples for computation of turbulence statistics. Time-mean flow fields are obtained as the arithmetic mean of solutions from about 40,000 iterations or more. This time-mean solution is averaged along the span-wise direction to obtain time and span-wise averaged solution at the end of each simulation. A small number of solutions that point in the span-wise direction makes the simple arithmetic mean inappropriate for span-wise averaging. Therefore, solutions at solution points are interpolated by a polynomial, and then span-wise average solutions are obtained by using a trapezoidal integration with very fine sampling. Note that, if not specified otherwise, the term "mean" is defined later in the text as for results averaged in time and space along the wingspan.

Convergence histories of the C_L and C_D showed a very slight upward drift in the values as visible in Figure 5.5. It seems that longer simulation time is needed to obtain a statistically converged solution than time reported by Uranga [17]. This has also been previously reported by Carton de Wiart and Hillewaert [11]. Authors believe that an enormous increase in computational cost due to extension of the simulation time could easily outweigh benefits of a statistically converged solution.

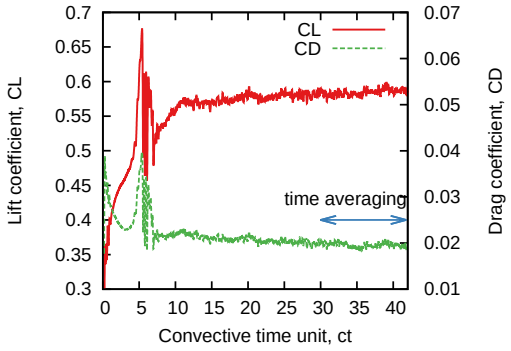

(a): p=2

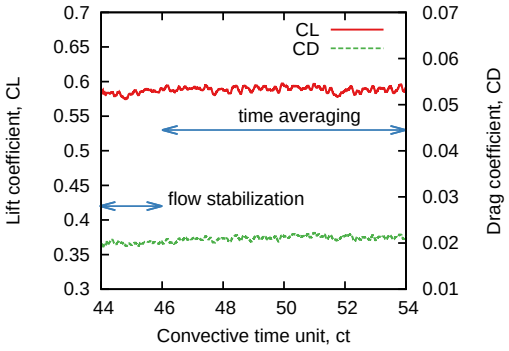

(b): p=3

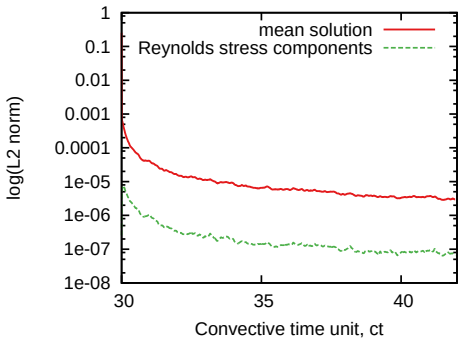

(c): p=2

Figure 5.5: Temporal evolution: lift and drag coefficients ($\alpha = 4°$, coarse domain)

5.3 Results and Discussion

In this chapter are presented and discussed results obtained from the current effort. In Section 5.3.1 are investigated several numerical parameters to limit numerical errors. Section 5.3.2 contains results for simulations at $\alpha = 4°$ and $Re = 60,000$. A long separation bubble is formed on the upper surface of the wing in mean time sense at this angle of attack. In Section 5.3.3 are presented results for simulations at $\alpha = 8°$ and $Re = 60,000$. The short LSB is formed on the upper surface of the wing for this angle of attack. In Sections 5.3.4, 5.3.5, and 5.3.6 are presented effects of the polynomial order on solution, comparison of LES and ILES, and comparison of explicit and implicit time integration schemes, respectively.

5.3.1 Numerical Considerations

Several numerical parameters are investigated at $\alpha = 8°$ and $Re = 60,000$ to limit numerical errors. Third-order simulations with the coarse mesh are chosen due to a large number of simulations in an attempt to reduce computational demands. For purposes of comparison, selected simulations are recomputed using the explicit third-order RK (TVD-RK3) scheme with a CFL number set to 0.45 and the time step size $\Delta t^* \approx 2 \times 10^{-6}$. Effects of the computational time step size on numerical solution are shown on mean surface skin friction coefficients (C_f) in Figure 5.8a. The C_f coefficients obtained with the LU-SGS scheme for time step sizes lower than $\Delta t^* = 3 \times 10^{-4}$ agree well compared to the explicit RK3. It seems that a transition to turbulence and, consequently, reattachment occur later in simulations with disproportionately large time steps.

The reference values for the Jacobian recalculation and number of sub-iterations used in the LU-SGS scheme (see Section 3.3.1) need to be selected. The Jacobian matrix is recalculated every 40 iterations. This value is based on the work of Sun et al. [78]. Sun et al. found it unnecessary to recompute the matrix every iteration, as they did not observed any significant effects on the convergence rate of the steady state problems with matrix recomputed every 40−100 iterations. Figure 5.6 shows that the convergence rate of the inner solver is not affected due to the worse approximation of the Jacobian matrix at higher recalculation intervals. Computational savings from the Jacobian freezing approach can be expressed as follows. In our code, if we assume the CPU time for one iteration is 1 U, then the cost for the matrix update is about 5 U. It takes 45 U for 40 iterations with one matrix update, while it takes 50 U for 40 iterations with two matrix updates. Figure 5.8b plots three skin friction distributions for the Jacobian matrix recalculation every 20, 40, and 100 iterations. The C_f distributions agree very well between the three simulations; thus, it seems that the recalculation every 40 iterations is adequate for the given flow conditions.

Additional parameter is number of sub-iterations. We used fixed number of sub-iterations set to 10 to sweep the unsteady residual, which needs to drop sufficiently within sub-iterations for unsteady problems. Figure 5.7a is a plot of the residual drop averaged over 1 CTU for several sub-iteration levels. The sweeping efficiency significantly decreases at higher sub-iterations. Moreover, it seems that the unsteady residual tends to oscillate at higher sub-iterations as shown in Figure 5.7b. Therefore, it seems that for unsteady flows to drive the unsteady residual every iteration to machine zero could be quite computationally exhaustive.

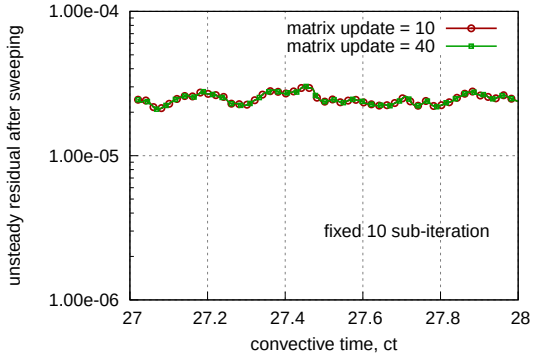

Figure 5.6: Unsteady residuals after 10 inner-iterations for the Jacobian matrix recalculated every 10 and 40 iterations.

With 10 sub-iterations as used in this study, the unsteady residual decreases by 3 orders or more. This seems to be a good compromise between accuracy and efficiency, because between the number of sub-iterations and computational cost is an almost linear relationship. Comparison of skin friction distributions for simulations with 5, 10, and 20 sub-iterations is shown in Figure 5.8d. The skin friction distributions agree well between the simulations with 10 and 20 sub-iterations; on the other hand, 5 sub-iterations lead to an under-resolved solution. Figure 5.8f compares the first- and second-order accurate-in-time LU-SGS schemes. The solutions agree well: the skin friction gradient is sharper and reattachment occurs earlier upstream with the second-order accurate LU-SGS scheme. The second-order accurate LU-SGS scheme is used for all simulations, since the CPU cost is only about 1.5% higher than the cost with the first-order accurate LU-SGS scheme. The increase in CPU time of only about 1.5% makes an implicit solver of higher orders promising, e.g., third- or fourth-order accurate-in-time. This was previously shown by Bassi et al. [103]. They reported that higher-order time schemes are more efficient than lower-order ones if the required accuracy is high and they seem to be more suitable for complex and demanding simulations of turbulent flows. However, we have not implemented an implicit solver for higher orders yet.

Figure 5.8c plots four averaging lengths: 2.5, 5, 10, and 20 CTUs. The C_f distributions are very similar for averaging longer than 5 CTUs. It seems that the averaging interval over 8–15 CTUs is sufficient, representing a good compromise between accuracy and efficiency. The C_f distributions obtained for the three meshes, i.e., meshes with two times finer radial,

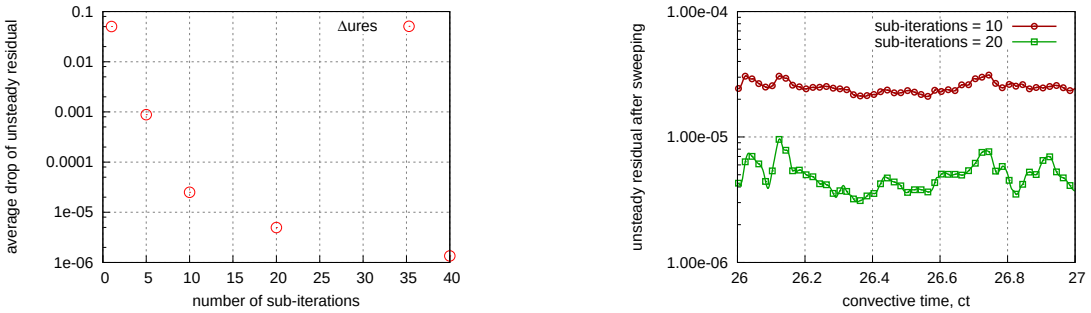

(a) (b)

Figure 5.7: a) Average drop (Δ *u-res* = *u-res*$_{init}$ - *u-res*$_{final}$) of unsteady residual as a function of sub-iterations (averaged over 1 CTU), b) unsteady residuals after 10 or 20 sub-iterations.

spanwise direction, and reference coarse mesh, agree fairly well—with some discrepancies—along the chord, as shown in Figure 5.8e. Simulations conducted by the authors showed that the streamwise resolution on the upper surface of the wing is of prime importance. The authors evaluated the effects of the refined radial and spanwise directions as relatively minor. The principal reason for this omission is a lack of computational power.

The order, the grid size, the number of degrees of freedom, and the computational costs expressed in work units needed for 1 convective time are summarized in Table 5.2. Compared with explicit time stepping, the computation time for LU-SGS is reduced by a factor of about 5, while producing comparable results.

Table 5.2: Computational cost of coarse $p = 2, 3$ and fine $p = 3$ simulations.

	Coarse				Fine	
	solution order p 2		solution order p 3		solution order p 3	
Scheme	RK3	LU-SGS	RK3	LU-SGS	RK3	LU-SGS
Dimension, cells	$7 \times 96 \times 24$		$7 \times 96 \times 24$		$7 \times 192 \times 24$	
DOFs	435,456		1,032,192		2,064,384	
Timestep, t^*	2.52×10^{-6}	2×10^{-4}	1.89×10^{-6}	2×10^{-4}	1.87×10^{-6}	2×10^{-4}
CFL	0.45	35.71	0.45	47.61	0.45	48
Memory GB	0.29	4.7	0.9	14.6	1.8	29.3
Work units for 1 CTU	1.12×10^5	2.18×10^4	3.77×10^5	7.65×10^4	7.71×10^5	1.62×10^5
LU-SGS speedup	5.14 times		4.93 times		4.76 times	

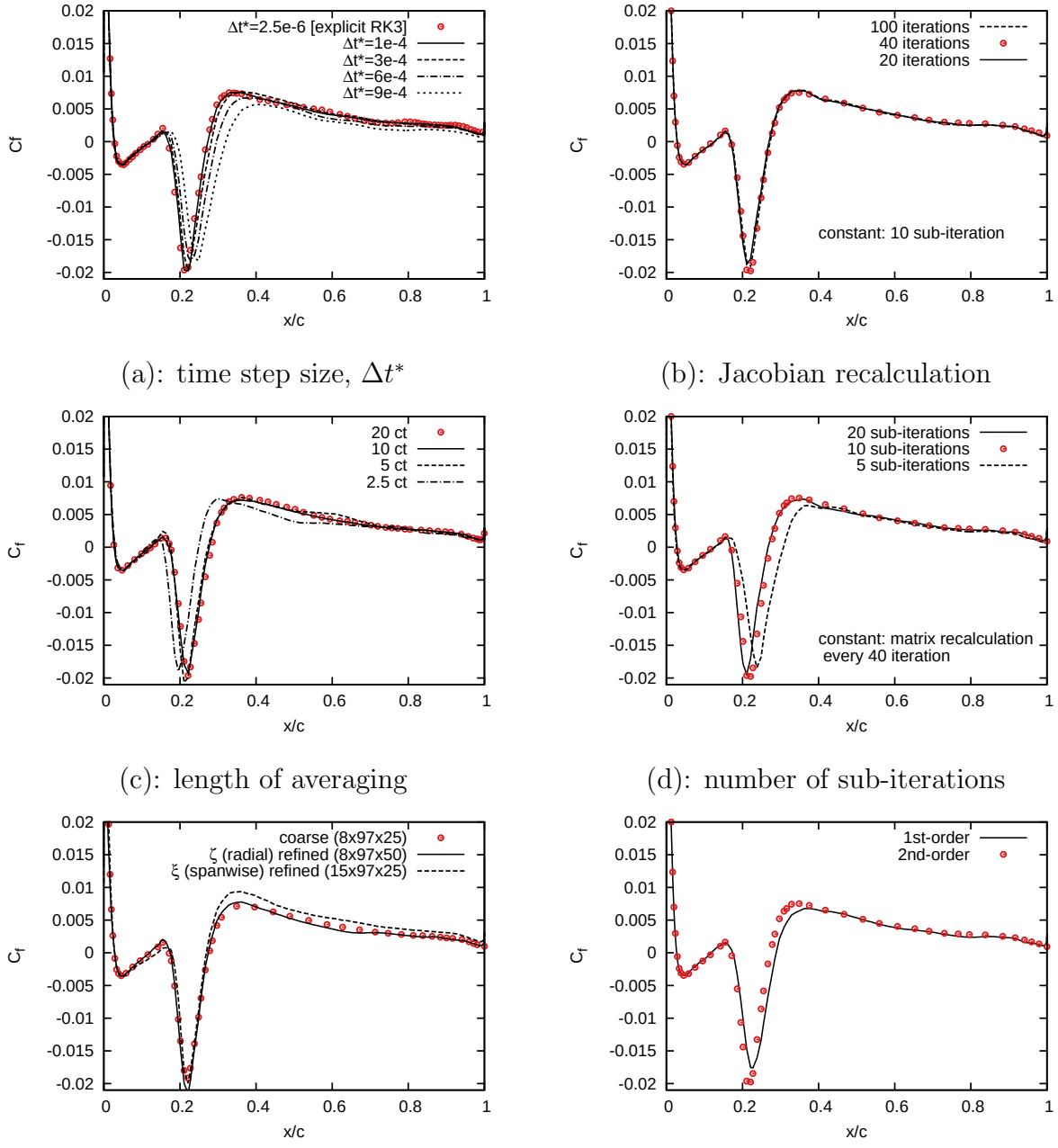

(a): time step size, Δt^*

(b): Jacobian recalculation

(c): length of averaging

(d): number of sub-iterations

(e): ξ and ζ resolution

(f): LU-SGS accuracy

Figure 5.8: Effects of the computational time step size (a), length of time averaging (b), radial or spanwise resolution (c), Jacobian matrix recalculation interval (d), number of sub-iterations (e), temporal order of accuracy (f) on numerical solution. Obtained from $p = 2$ coarse simulation at $\alpha = 8°$.

5.3.2 Reynolds Number = 60,000, $\alpha = 4°$

This chapter discusses the results at $\alpha = 4°$ and Reynolds number = 60,000 obtained from the work described in the previous sections.

A laminar separation occurs at approximately 20% of the chord length for $\alpha = 4°$. Consequently, the flow reattaches at approximately 66% of the chord. Figure 5.9 shows mean streamwise velocity contours for $\alpha = 4°$. A LSB that is relatively lengthy in mean time is formed on the suction side of the wing for this angle of attack.

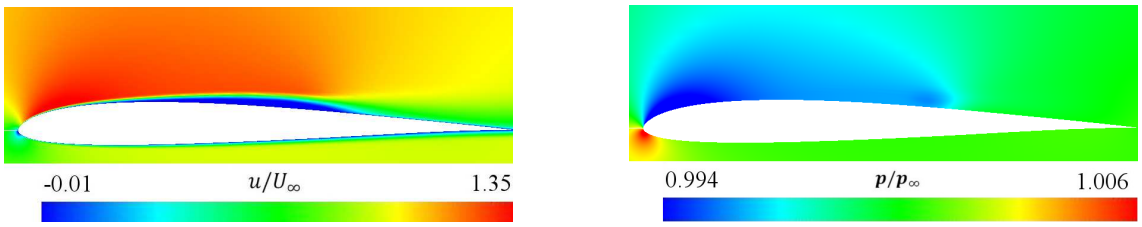

(a): u-velocity (b): pressure

Figure 5.9: Mean u-velocity and pressure contours from fine $p = 3$ simulations at $\alpha = 4°$.

The lift coefficient (C_L), drag coefficient (C_D), separation (x_{sep}), and reattachment (x_r) locations are compared in Table 5.3 with those reported previously in the literature. The values for separation x_{sep} and reattachment x_r are obtained from observing the velocity profiles in the boundary layer. At $\alpha = 4°$, the results are compared with previous numerical studies that used CD [15, 109], FD [104], DG [11, 17], and SD [18, 19] high-order schemes, and with several experiments [112, 113, 114, 115]. Table 5.3 also shows DOFs. They usually range from 1 to 53 million in the literature for this angle of attack, with most studies having around 4–6 million DOFs. Our finest mesh consists of 2 million solution points, i.e., DOFs. This value is similar to those of studies by Uranga et al. [12], Castonguay et al. [19], Bassi et al. [103], and others. The mean C_L and C_D coefficients converge to $C_L = 0.6$ and $C_D = 0.022$ for $\alpha = 4°$. x_{sep} and x_r for the fourth-order ($p = 3$) simulation are predicted to be 0.198 and 0.660 x/c, respectively. These results are consistent with the literature.

Figure 5.10 shows mean C_p and C_f distributions for the degree $p = 1, 2, 3$. The C_f profiles are shown only for the suction side of the wing. The pressure gradient is not steep in the transition region, and transition into turbulence occurs further upstream for the

Table 5.3: Mean results: present study and literature ($\alpha = 4°$).

	$\overline{C_L}$ [–]	$\overline{C_D}$ [–]	x_{sep}/c [–]	x_r/c [–]	Scheme order/type	DOFs in millions
Author						
Garmann and Visbal [109] very fine	0.599	0.0215	0.207	0.649	$\mathcal{O}(6)$ ILES CD	53.4
Galbraith and Visbal [15] overset	0.59	0.021	0.23	0.65	$\mathcal{O}(6)$ ILES CD	5.7
Galbraith and Visbal [14] fine overset	—	—	0.20	0.66	$\mathcal{O}(6)$ ILES CD	6.6
Boom and Zingg [104]	0.60	0.022	0.21	0.64	$\mathcal{O}(4)$ ILES FD SBP/SAT	4.9
Uranga, Persson and Drela [12]	0.60	0.022	0.24	0.6	$\mathcal{O}(4)$ ILES DG	1
Hillewaert and Carton de Wiart [11]	0.60	0.022	0.21	0.66	$\mathcal{O}(4)$ ILES DG	—
Zhou and Wang [18]	—	—	0.227	0.685	$\mathcal{O}(4)$ ILES SD	5
Castonguay, Liang and Jameson [19]	—	—	0.23	0.65	$\mathcal{O}(4)$ ILES SD	3.1
Catalano and Tognaccini [106]	0.62	0.023	0.021	0.64	$\mathcal{O}(2)$ FD & dyn. Smag.	8.86
Experiment						
Selig, Donovan and Fraser [112]	≈ 0.58	≈ 0.021	—	—	—	—
Selig, Guglielmo and et al. [113]	≈ 0.60	≈ 0.0165	—	—	—	—
Radespiel and et al. (TU–BS) [114]	—	—	0.3	0.62	—	—
Ol, McAuliffe and et al. (HFWT) [115]	—	—	0.18	0.58	—	—
Present study						
Coarse $p = 1$	0.571	0.0212	0.247	0.713	$\mathcal{O}(2)$ ILES FR	0.13
Coarse $p = 2$	0.584	0.0198	0.241	0.622	$\mathcal{O}(3)$ ILES FR	0.4
Coarse $p = 3$	0.595	0.0222	0.228	0.654	$\mathcal{O}(4)$ ILES FR	1
Fine $p = 2$	0.604	0.0215	0.204	0.661	$\mathcal{O}(3)$ ILES FR	0.9
Fine $p = 3$	0.599	0.0223	0.198	0.660	$\mathcal{O}(4)$ ILES FR	2

second-order ($p = 1$) simulation on the coarse mesh. The second-order accurate simulation ($p = 1$) fails in recovering C_f after the reattachment at 0.71 x/c. The transition to turbulence is suppressed with stronger vortical structures traveling further downstream. This has a negative effect on the flow downstream and leads to misprediction of the C_f in the turbulent regime. We conclude that the coarse mesh with $129,024$ DOFs is obviously insufficient for the second-order ($p = 1$) simulations.

The third-order ($p = 2$) simulation on the coarse mesh with $435,456$ DOFs shows an improvement. The coarse $p = 3$ and $p = 2, 3$ fine simulations have quite similar C_p and C_f profiles. The pressure gradient is steeper in the transition region, and the C_f profile seems to be successfully recovered in the turbulent regime. Noticeable differences between the coarse $p = 3$ and $p = 2, 3$ fine simulations can be observed in the separation region from 0.1 to 0.3 x/c and in the turbulent region from 0.6 to 1 x/c. An increase in the number of solution points in a streamwise direction (fine mesh) caused that separation occurs earlier, while reattachment later downstream for $p = 2, 3$ simulations.

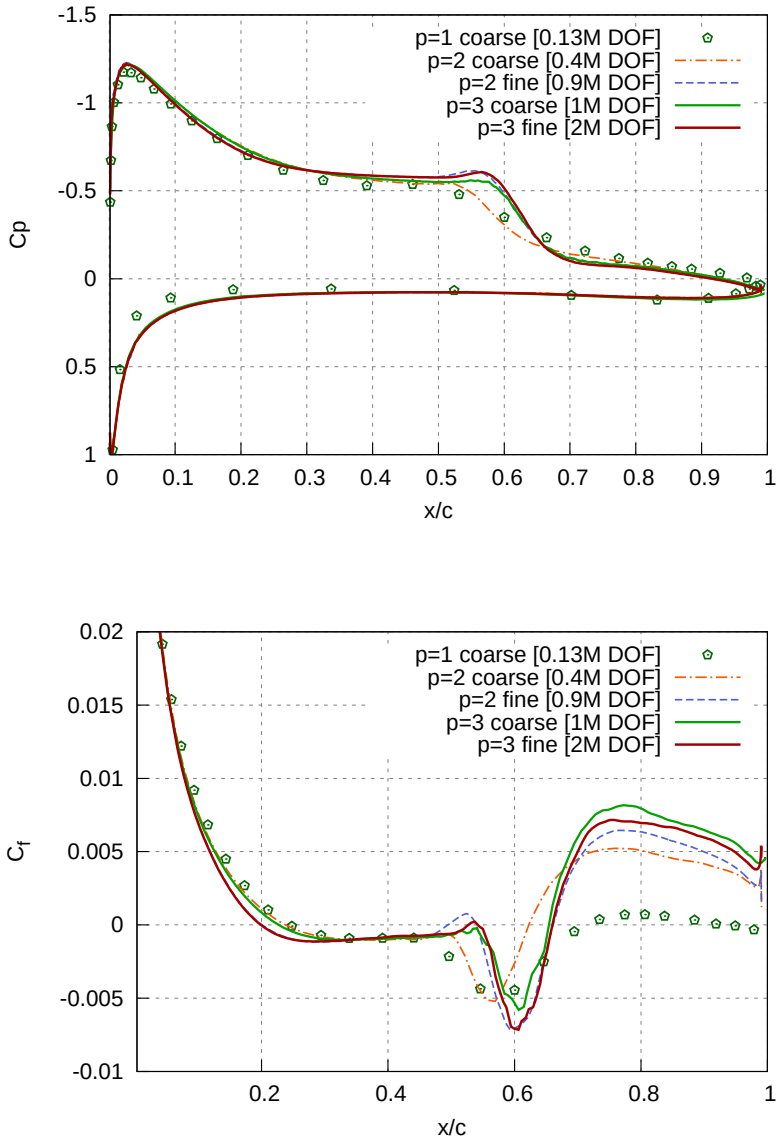

Figure 5.10: Mean surface C_p and C_f distributions at $\alpha = 4°$.

Figure 5.11 plots C_p and C_f distributions from the fourth-order ($p = 3$) simulations for $\alpha = 4°$ compared with the literature [14, 15, 16, 102, 109, 116]. The results for $\alpha = 4°$ show good agreement with the literature, despite the lower resolution used in our study. Differences between the coarse and fine simulations seem to be caused by the insufficient

streamwise resolution of the coarse domain. This trend is similar to Galbraith's results on the "overset," and streamwise refined "fine overset" meshes. It seems that results for $\alpha = 4°$ agree reasonably well with the literature.

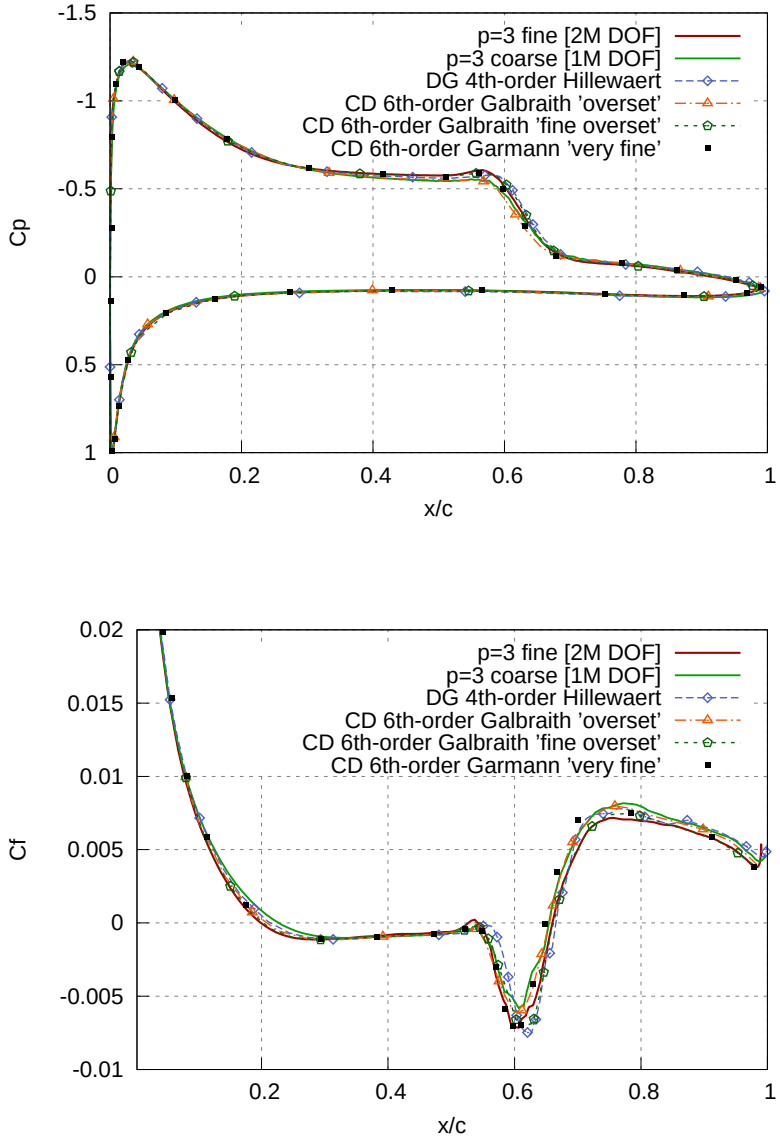

Figure 5.11: Mean surface C_p and C_f compared to the literature values at $\alpha = 4°$.

Figure 5.12a,b compares the mean boundary layer (BL) velocity profiles and mean-squared fluctuations of u-velocity with the literature [102, 109, 116] for $\alpha = 4°$. It seems that BL profiles are in reasonable agreement with the literature with respect to coarser domains used in this study.

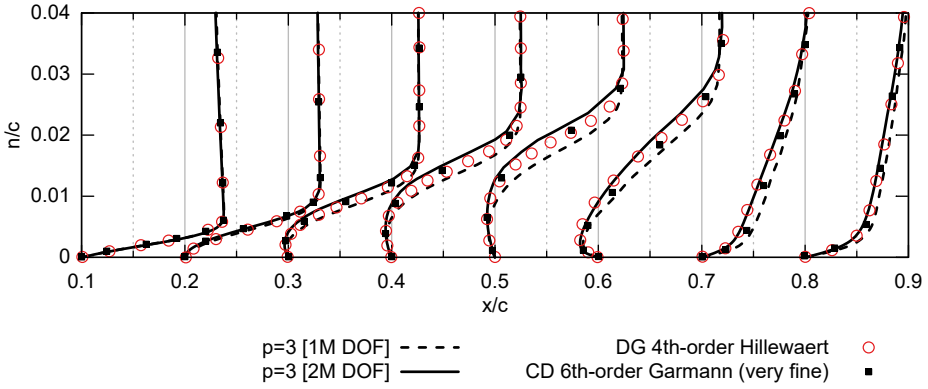

(a): u-velocity at $\alpha = 4°$

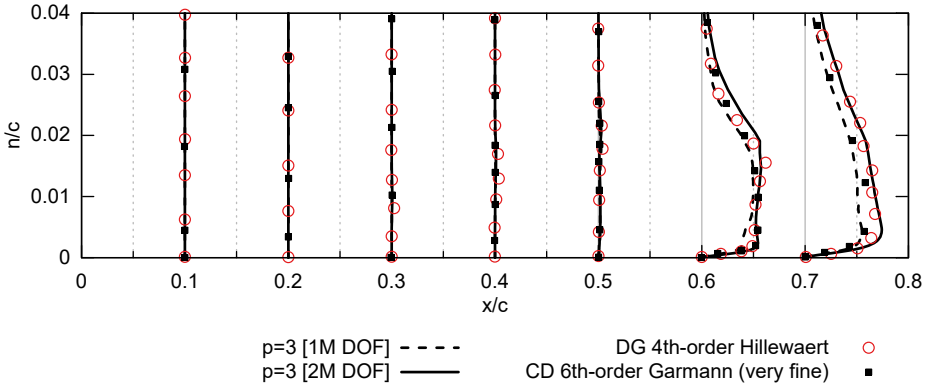

(b): $\overline{u^2}$ at $\alpha = 4°$

Figure 5.12: Boundary layer profiles of u-velocity and mean-squared fluctuations of u-velocity ($\overline{u^2}$) at $\alpha = 4°$

Figure 5.13 shows the three-dimensional vortical structures visualized by the iso-surfaces of the Q-criterion [100], colored with the local value of the Mach number for $\alpha = 4°$. In this study, the predicted vortical structures seem to be in agreement with those in the literature, although long hairpin-like vortices are not clearly visible, as they are in the literature [15, 19, 109]. The low-order ($p = 1$) solution on the coarse mesh shows that the

vortex disintegration is suppressed, with the robust vortical structures appearing further downstream. A similar trend is visible between the third-order ($p = 2$) and fourth-order accurate ($p = 3$) simulations with comparable DOFs, as shown by Figures 5.13b and 5.13c. Different performance on meshes with similar resolution illustrates the positive effect of a higher polynomial degree on the solution. The excessive dissipation is associated with the lower polynomial degrees. Section 4.3.1 discussed the effect of higher polynomial degrees on the under-resolved turbulence in simulations of a compressible Taylor–Green vortex. The visualized structures indicate that the laminar-turbulent transition in a laminar separation bubble is dominated by vortex formation and the breakup process. The span-wise vortices—formed by the roll-up process in the shear layer—are recognizable after 50% of the chord. Immediately downstream of their formation, the vortices become distorted in the stream-wise direction and quickly disintegrate into small-scale turbulence.

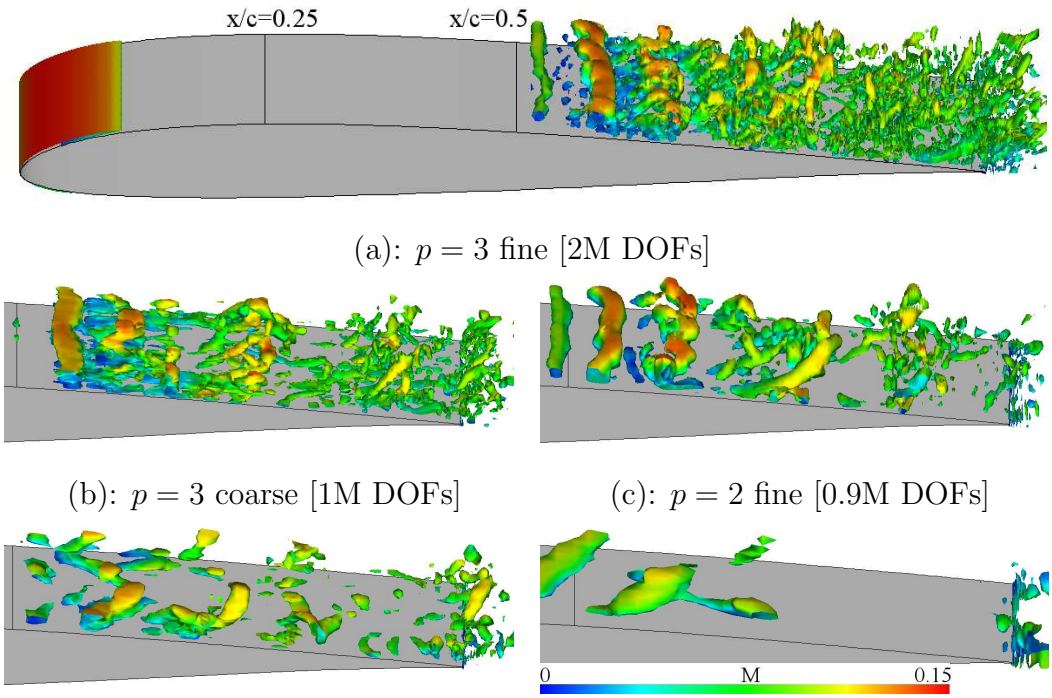

(a): $p = 3$ fine [2M DOFs]

(b): $p = 3$ coarse [1M DOFs]

(c): $p = 2$ fine [0.9M DOFs]

(d): $p = 2$ coarse [0.4M DOFs]

(e): $p = 1$ coarse [0.13M DOFs] (Q = 200)

Figure 5.13: Instantaneous iso-surfaces of Q-criterion colored with the Mach number ($\alpha = 4°$, $Q = 500$).

Figure 5.14 shows a sequence of six consecutive instantaneous snapshots of the unsteady flow for $\alpha = 4°$ with corresponding C_p and C_f distributions. This sequence illustrates the unsteadiness of the flow, as well as that span-wise vortices are periodically shed from the bubble.

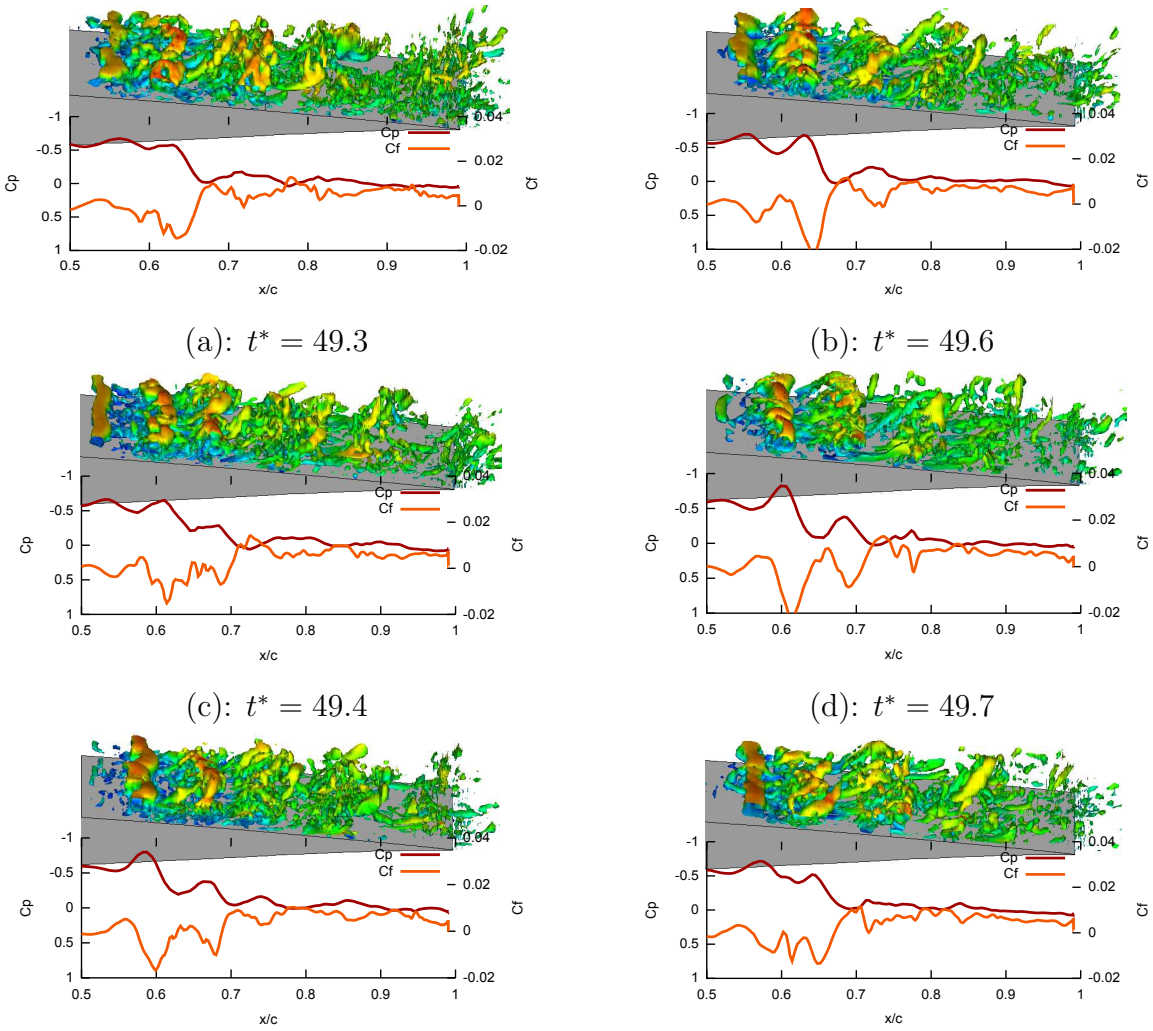

(a): $t^* = 49.3$ (b): $t^* = 49.6$

(c): $t^* = 49.4$ (d): $t^* = 49.7$

(e): $t^* = 49.5$ (f): $t^* = 49.8$

Figure 5.14: Instantaneous iso-surfaces of Q-criterion colored with the Mach number (top) with corresponding C_p and C_f distributions ($\alpha = 4°$, $Q = 500$, $p = 3$ fine).

Better insight on the laminar–turbulent transition provides Figure 5.16, which plots contours of the turbulent kinetic energy,

$$\text{TKE} = \frac{1}{2}\left(\overline{u'^2} + \overline{v'^2} + \overline{w'^2}\right) \quad ,$$

and Reynolds stress component,

$$\tau_{xy} = \frac{\overline{u'\,v'}}{U_\infty^2},$$

for $\alpha = 4°$ and $p = 1, 2, 3$ simulations on coarse and fine meshes. Figure 5.15 shows contours from numerical simulation [15] and experiments [114, 115]. Contours are taken from Galbraith et al. [15] for comparison. In Figure 5.16, coordinates $x\,, y$ are two-dimensional x, y coordinates rotated about the origin $(0, 0)$ by an angle α to match the style used by Galbraith in Figure 5.15. Simulations $p = 1, 2$ on a coarse domain are clearly under-resolved due to the insufficient resolution. This is in agreement with previous observations from Figure 5.10, where C_p and C_f differ from other results in the critical region after 50% chord length. Simulations $p = 3$ on coarse and fine domains show significant improvement. The shape, extent, and magnitude seem to agree to a reasonable degree with those in the literature.

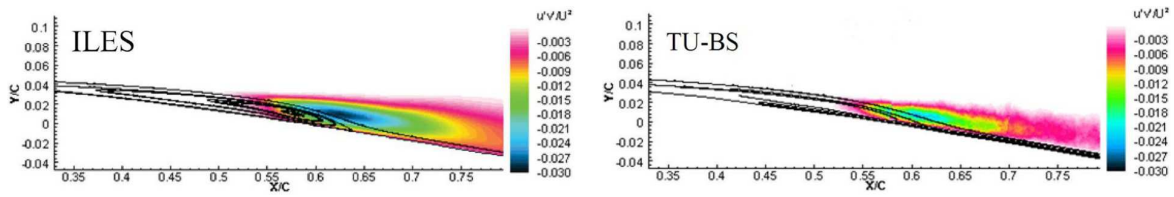

(a): ILES Galbraith et al. [15]

(b): Exp. TU-BS [114]

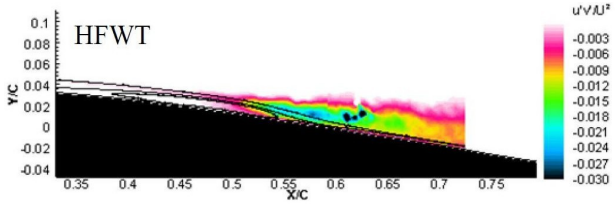

(c): Exp. HFWT [115]

Figure 5.15: Reynolds stress ($\overline{u'\,v'}$) contours at $\alpha = 4°$ taken from Galbraith et al. for the purpose of comparison.

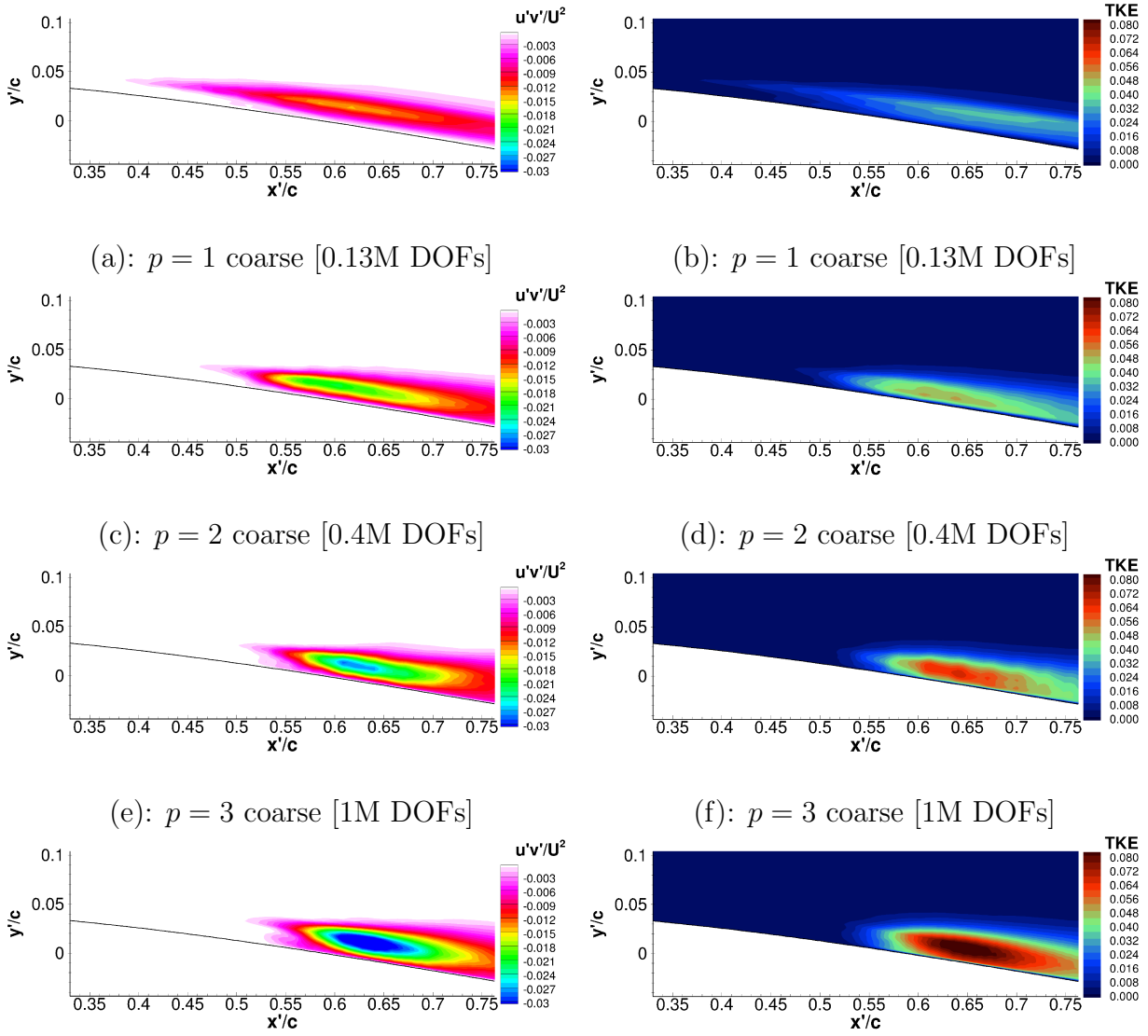

(a): $p = 1$ coarse [0.13M DOFs]

(b): $p = 1$ coarse [0.13M DOFs]

(c): $p = 2$ coarse [0.4M DOFs]

(d): $p = 2$ coarse [0.4M DOFs]

(e): $p = 3$ coarse [1M DOFs]

(f): $p = 3$ coarse [1M DOFs]

(g): $p = 3$ fine [2M DOFs]

(h): $p = 3$ fine [2M DOFs]

Figure 5.16: Reynolds stress ($\overline{u\,v}$) and TKE contours at $\alpha = 4°$. Results are for ILES, $p = 1, 2, 3$ simulations.

To obtain greater insight into the LSB dynamics, e.g., the shedding frequency of the span-wise vortices, the frequency spectra are plotted for the fourth-order ($p = 3$) simulation on the fine mesh. Figure 5.17 shows the frequency spectra of the stream-wise velocity component at 0.1, 0.5, and 0.95 x/c stations for $\alpha = 4°$. Recorded u-velocities from the three stations on the suction side of the wing are transformed into the frequency domain using the Fourier transform. Velocity probes are positioned at the mid-span at approximately half the local time-mean boundary layer height. The cutoff frequency associated with the size corresponding to the high-order nodes is shown by a vertical line. The uniform distribution of fluctuations in the solution indicates that energy is not accumulated at certain wavelengths. At $\alpha = 4°$, the breakdown of the shear layer occurs at about 0.5 x/c and the spectrum at $x/c = 0.5$ shows distinct peak frequencies of $f^* = 5.13$, 7.69, and 9.49. It seems that these frequencies are most likely associated with vortex shedding. Zhou and Wang [18] suggest that there is not a single vortex shedding frequency but more likely there is a continuous frequency band $4 \leq f^* \leq 9$. This study's results agree also reasonably well with the numerical study of Galbraith et al. [15], where vortex shedding frequencies of $f^* = 5.8$, 6.4, 7.3, and 9.2 were found.

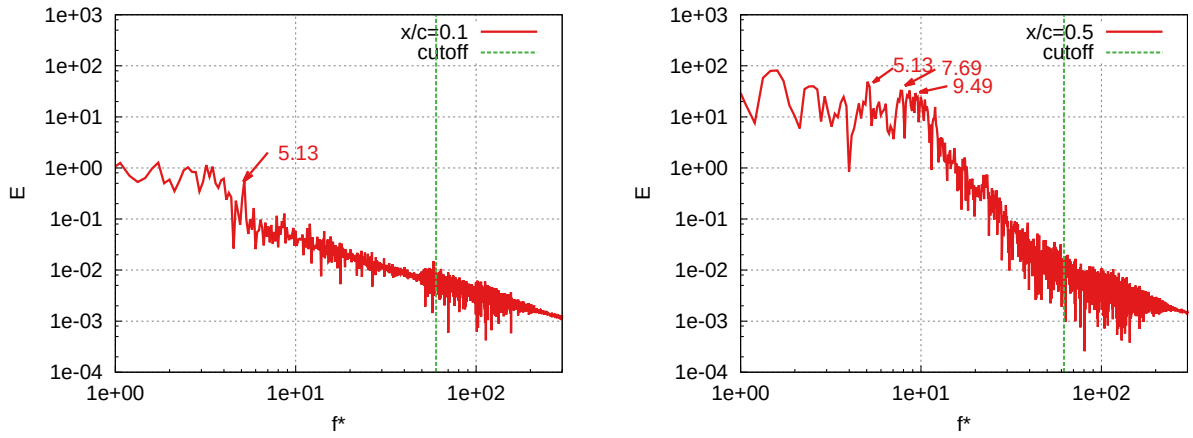

(a): $x/c = 0.1$ (b): $x/c = 0.5$

Figure 5.17: Frequency spectra of u-velocity. Three probes were placed in the BL on the upper surface of the wing. Obtained from $p = 3$ fine simulation at $\alpha = 4°$.

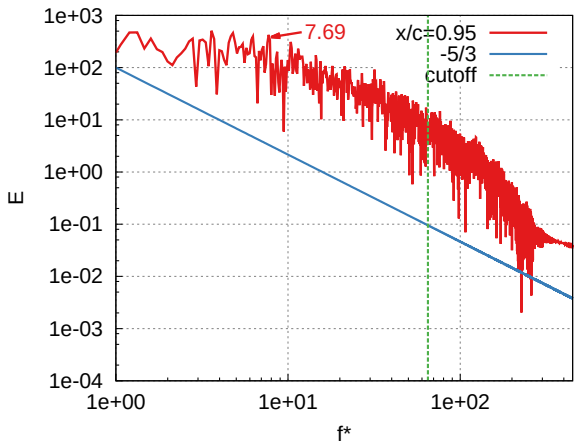

(a): $x/c = 0.95$

Figure 5.18: Continue of Figure 5.17: Frequency spectra of u-velocity at $x/c = 0.95$.

5.3.3 Reynolds Number = 60,000, $\alpha = 8°$

In this chapter, the results at $\alpha = 8°$ and Reynolds number = 60,000 are presented and discussed.

A laminar separation occurs almost immediately at approximately 3% of the chord length for $\alpha = 8°$. The flow reattaches at approximately 25% of the chord. Figure 5.19 shows mean streamwise velocity contours for $\alpha = 8°$. The LSB shortens in length and moves toward the leading edge (LE) for higher α, and turbulent flow is so over the most of the upper surface. The mean lift coefficient (C_L), drag coefficient (C_D), separation (x_{sep}),

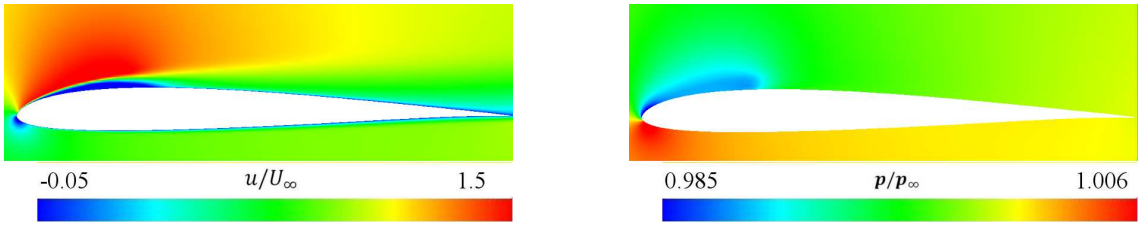

(a): u-velocity (b): pressure

Figure 5.19: Mean u-velocity and pressure contours from fine $p = 3$ simulations at $\alpha = 8°$.

and reattachment (x_r) locations are compared in Table 5.4 with those reported previously in the literature. At $\alpha = 8°$, the results are compared with numerical results reported by various authors using DG [13, 103], FD [104, 105, 106], and CD [15, 16, 109] high-order schemes, and with two additional experiments [112, 113]. Table 5.4 also shows DOFs. At $\alpha = 8°$, the DOFs range from 4 to 53 million in the literature. Our finest domain with 2 million DOFs is coarser—in terms of the number of DOFs—than those of most previous studies for this angle of attack. Taking a closer look at the results for $\alpha = 8°$ in Table 5.4, it seems that there is no general agreement across the results, as there is for $\alpha = 4°$. Therefore, it seems that the $\alpha = 8°$ case is considerably more challenging, most likely because the turbulent flow occurs over almost the whole length of the suction side of the wing. The mean C_L and C_D coefficients for the fourth-order ($p = 3$) fine simulation at $\alpha = 8°$ are 0.924 and 0.0433, respectively. Separation and reattachment occur at 0.030 and 0.297 x/c, respectively. These values agree reasonably well with the results from other authors. However, the noticeable discrepancies in the results of the experiments and numerical simulations require further explanation.

Table 5.4: Mean results: present study and literature ($\alpha = 8°$).

	$\overline{C_L}$ [–]	$\overline{C_D}$ [–]	x_{sep}/c [–]	x_r/c [–]	Scheme order/type	DOFs in millions
Author						
Garmann and Visbal [109] very fine	0.917	0.045	0.031	0.303	$\mathcal{O}(6)$ ILES CD	53.4
Garmann, Visbal and Orkwis [16] fine	0.969	0.039	0.023	0.259	$\mathcal{O}(6)$ ILES CD	12.5
Garmann, Visbal and Orkwis [16] coarse	0.970	0.044	0.023	0.284	$\mathcal{O}(6)$ ILES CD	9.1
Galbraith and Visbal [15] overset	0.92	0.043	0.040	0.280	$\mathcal{O}(6)$ ILES CD	5.7
Boom and Zingg [104]	0.968	0.034	0.037	0.2	$\mathcal{O}(4)$ ILES FD	4.9
Catalano and Tognaccini [106]	0.95	0.044	0.033	0.29	$\mathcal{O}(2)$ FD & dyn. Smag.	8.86
Beck, Bolemann and et al. [13]	0.923	0.045	0.027	0.310	$\mathcal{O}(4)$ ILES DG-SEM	4.26
Weide, Giangaspero and Svärd [105]	0.918	0.045	0.034	0.308	$\mathcal{O}(5)$ ILES FD	4
Bassi, Botti and et al. [103]	0.953	0.045	0.027	0.294	$\mathcal{O}(5)$ ILES DG	0.7
Experiment						
Selig, Donovan and Fraser [112]	≈ 0.89	≈ 0.048	—	—		—
Selig, Guglielmo and et al. [113]	≈ 0.92	≈ 0.029	—	—		—
Present study						
Coarse $p = 1$	0.940	0.0466	0.061	0.371	$\mathcal{O}(2)$ ILES FR	0.13
Coarse $p = 2$	0.962	0.0418	0.026	0.283	$\mathcal{O}(3)$ ILES FR	0.4
Coarse $p = 3$	0.934	0.0385	0.030	0.257	$\mathcal{O}(4)$ ILES FR	1
Fine $p = 2$	0.937	0.0408	0.030	0.264	$\mathcal{O}(3)$ ILES FR	0.9
Fine $p = 3$	0.924	0.0433	0.030	0.297	$\mathcal{O}(4)$ ILES FR	2

Surprisingly, Selig's [113] experiment from 1995 shows a considerably lower drag coefficient than those measured in 1989 [112] or those predicted by numerical simulations. Selig et al. reported that the measured mean aerodynamic forces differed widely in each experimental run for Re = 60,000. Moreover, experimental data collected from four span-wise locations differed radically by about $\pm 20\%$ C_D from each other, where the final coefficient is an average value from the four span-wise locations. Selig et al. reported difficulties for all airfoils tested at Re = 60,000 [112, 113]. One possible explanation is that the separated flow at a given low Reynolds number is highly sensitive to the free-stream turbulence. Due to its nature, experiments were conducted with some measurable turbulence intensity, whereas implicit large-eddy simulations were performed with zero turbulence intensity. This could explain some of the discrepancies found between experiments and numerical simulations.

Figure 5.20 shows mean C_p and C_f distributions for the degree $p = 1, 2, 3$. The C_f profiles are shown only for the suction side of the wing. The second-order accurate simulation ($p = 1$) fails in recovering C_f after the reattachment. This is a similar result as for $\alpha = 4°$. The third-order ($p = 2$) simulation on the coarse mesh with $435,456$ DOFs shows again an improvement compared to $p = 1$ simulation. At $\alpha = 8°$, differences between $p = 2, 3$ coarse, $p = 2$ fine, and $p = 3$ fine simulations are also visible as at $\alpha = 4°$. It seems that the fine $p = 3$ simulation has some patterns in common for both angles of attack. The reattachment is predicted later, and simultaneously the C_f peak after the reattachment seems to be lower for the fine $p = 3$ simulation compared to the coarse $p = 3$ simulation. This is more pronounced at 8° than at 4°.

Figure 5.21 show C_p and C_f distributions from the fourth-order ($p = 3$) simulation for $\alpha = 8°$, compared with the literature [13, 16, 103, 105, 109, 117]. At $\alpha = 8°$, the C_p distribution for the fourth-order ($p = 3$) simulation on the coarse mesh is reasonably close to the distribution found by Garmann et al. [16] until the point where the flow undergoes the transition to turbulence. The early transition is shifting the drop of the C_f upstream. The transition on the fine mesh is delayed. Moreover, the flat pressure plateau is lower for the finest ($p = 3$) simulation. It is not clear why pressure plateaus differ across the literature, or in this study's results. This suggests the need for accurate and reliable DNS reference database to evaluate the quality of the LES results. Overall, however, it seems that results for $\alpha = 8°$ agree reasonably well with the literature, as our results lie somewhere between the previously published results.

Figure 5.22 shows the three-dimensional vortical structures visualized by the iso-surfaces of Q-criterion [100], colored with the local value of the Mach number for $\alpha = 8°$. The predicted vortical structures seem to be in agreement with the literature. Similar to $\alpha = 4°$, long, hairpin-like vortices are not clearly visible, as they are in the literature [16, 103]. At $\alpha = 8°$, Kelvin–Helmholtz instabilities are clearly visible near the leading edge, with the spanwise vortices recognizable after 10% of the chord. The vortical structures at $\alpha = 4°$ are discussed in Section 5.3.2.

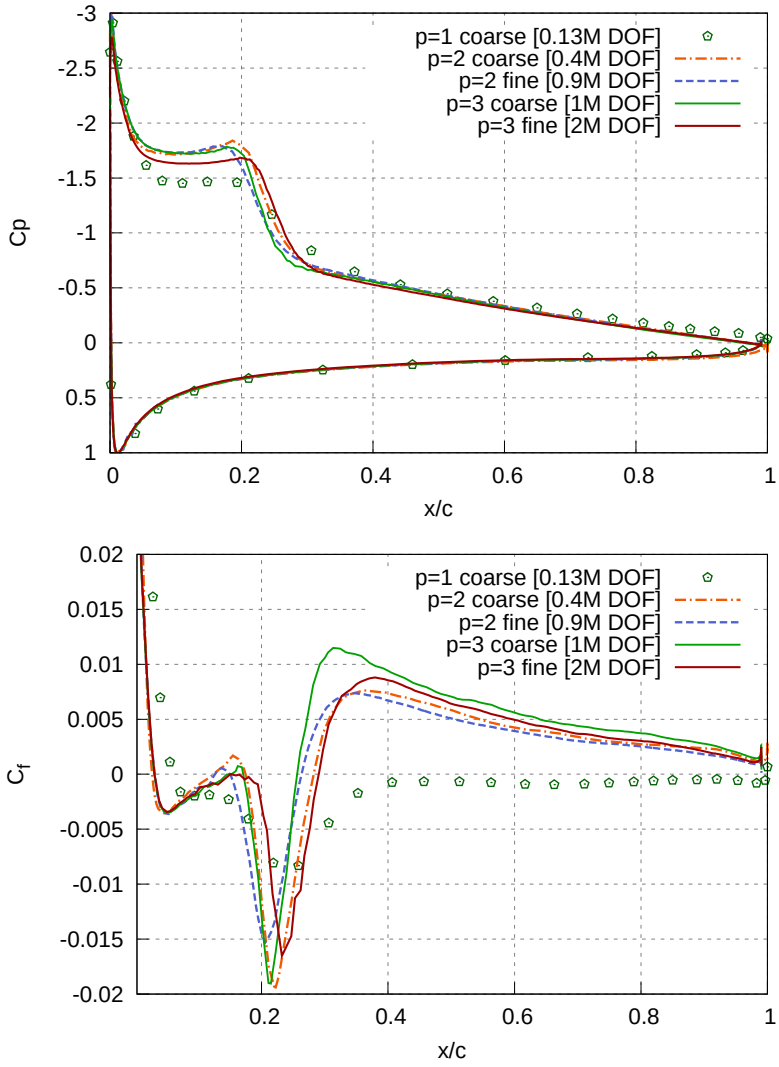

Figure 5.20: Mean surface C_p and C_f distributions at $\alpha = 8°$.

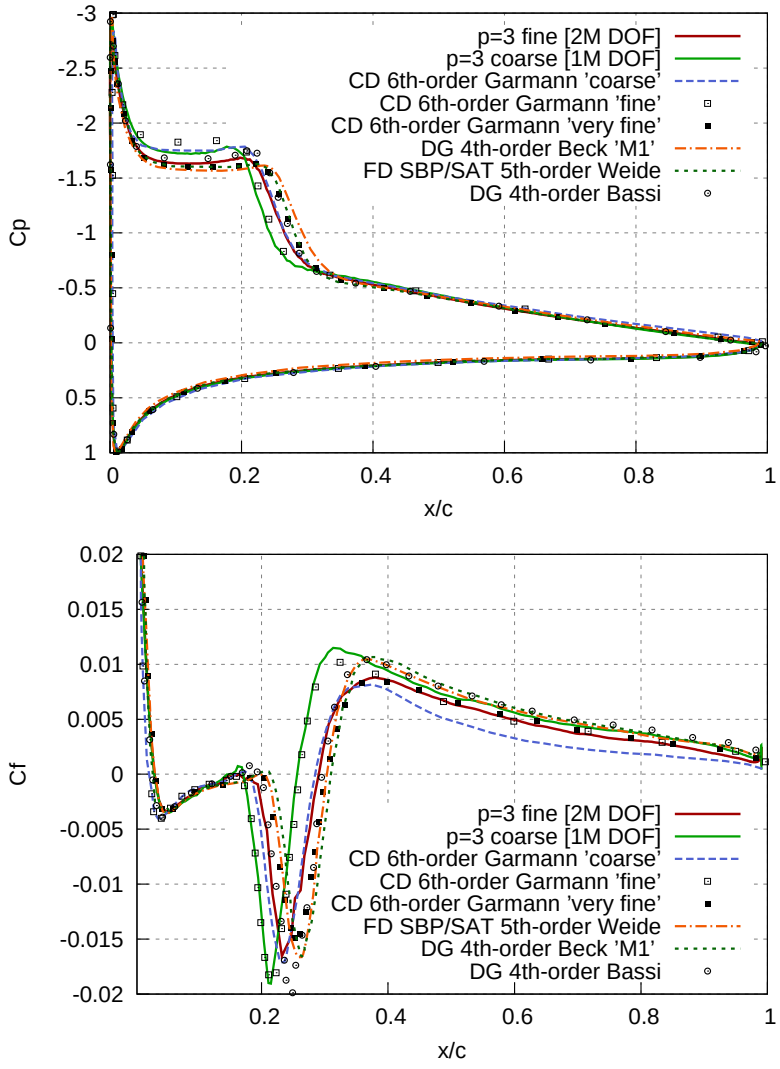

Figure 5.21: Mean surface C_p and C_f compared to the literature values at $\alpha = 8°$.

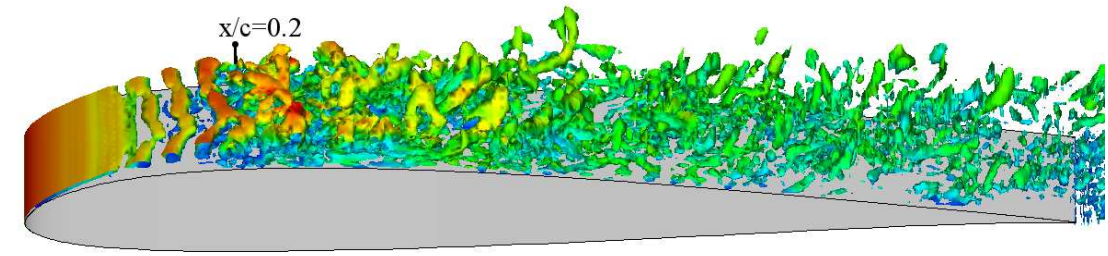

(a): $p = 3$ fine [2M DOFs]

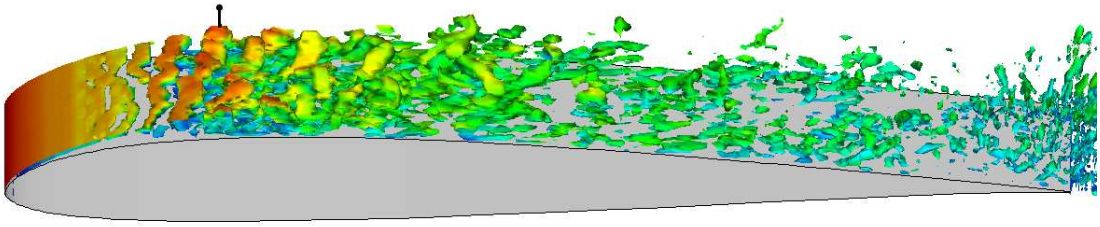

(b): $p = 3$ coarse [1M DOFs]

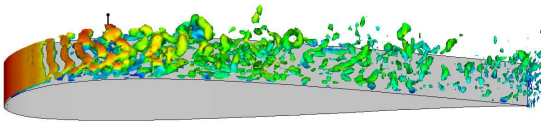

(c): $p = 2$ fine [0.9M DOFs]

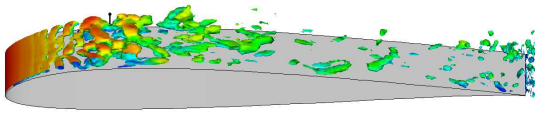

(d): $p = 2$ coarse [0.4M DOFs]

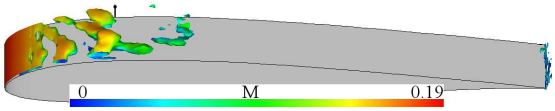

(e): $p = 1$ coarse [0.13M DOFs]

Figure 5.22: Instantaneous iso-surfaces of the Q-criterion colored with the Mach number ($\alpha = 8°$, $Q = 500$, only $p = 1$ $Q = 200$).

The frequency spectra are obtained for the fourth-order ($p = 3$) simulation on the fine mesh for $\alpha = 8°$ in the same manner as at $\alpha = 4°$. The procedure is described in the previous Section 5.3.2. At $\alpha = 8°$, the breakdown of the shear layer occurs at about 0.15 x/c, and the spectrum at $x/c = 0.1$ shows a distinguishable peak frequency $f^* = 22.5$. This indicates that vortex shedding is faster at a higher angle of attack. A corresponding frequency is not recognizable further downstream at stations 0.5 and 0.95 x/c.

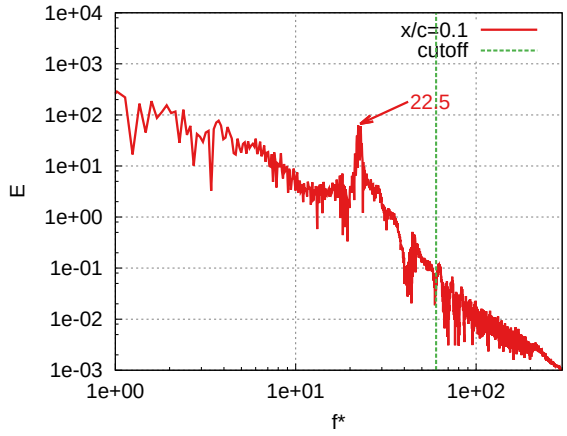

(a): $x/c = 0.1$

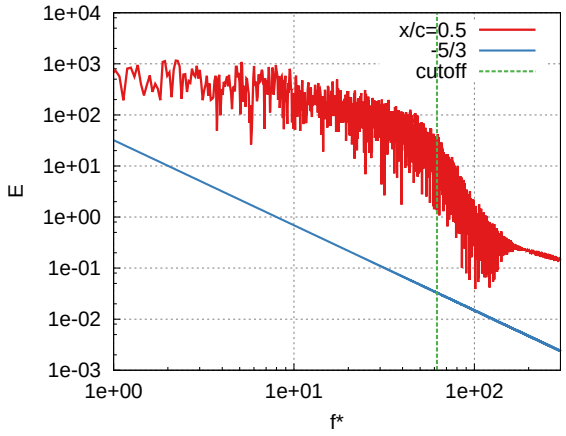

(b): $x/c = 0.5$

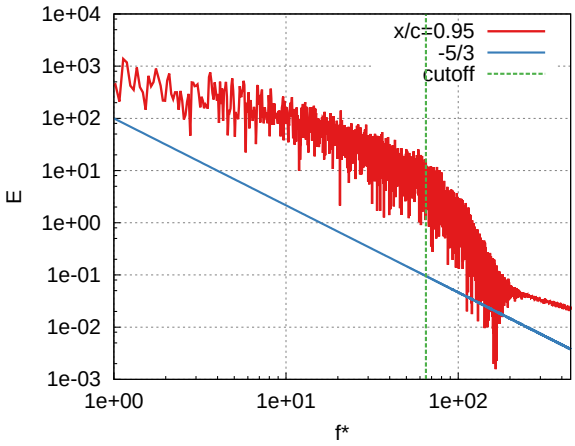

(c): $x/c = 0.95$

Figure 5.23: Frequency spectra of u-velocity. Three probes were placed in the BL on the upper surface of the wing. Obtained from $p = 3$ fine simulation at $\alpha = 8°$.

Figures 5.24a and 5.24b compare the mean boundary layer velocity profiles and mean-squared fluctuations of the u-velocity with those in the literature [16, 13, 109, 117] for $\alpha = 8°$. On the coarse grid, there are slightly overpredicted velocities along the whole upper surface. Also, the mean-squared fluctuations of the u-velocity at $x/c = 0.2$ deviate from the profiles found in the literature. However, the result from the $p = 3$ fine simulation shows an improvement towards higher mesh resolutions. It seems the BL profiles are in very reasonable agreement with those in the literature with respect to the maximum 2 million DOFs used in our study.

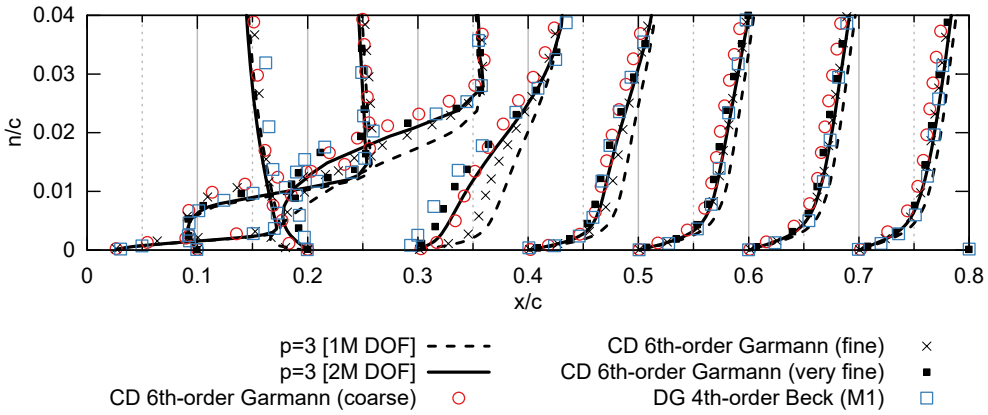

(a): u-velocity at $\alpha = 8°$

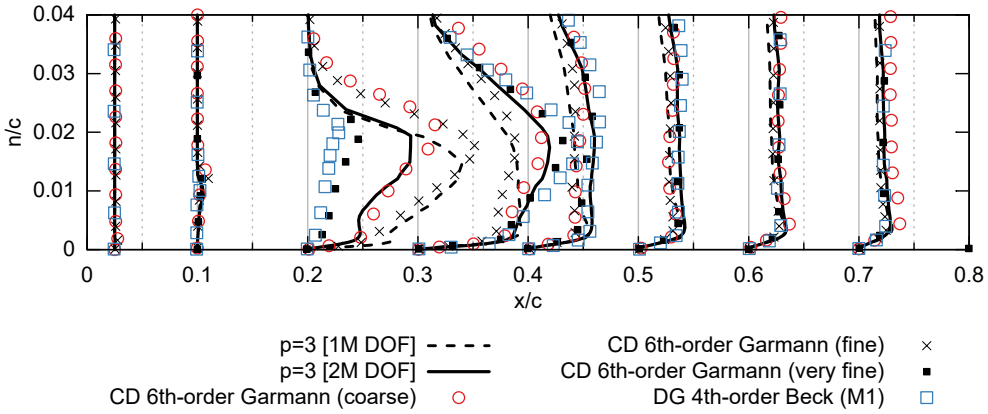

(b): $\overline{u^2}$ at $\alpha = 8°$

Figure 5.24: Boundary layer profiles of u-velocity and mean-squared fluctuations of u-velocity ($\overline{u^2}$) at $\alpha = 8°$

Figures 5.25 and 5.26 plot contours of the turbulent kinetic energy and Reynolds stress component τ_{xy} for $\alpha = 8°$ and $p = 1, 2, 3$ simulations on coarse and fine meshes. Figure 5.25 shows contours from numerical simulations conducted by Galbraith and Visbal [15] and Garmann, Visbal and Orkwis [16] for comparison. In Figure 5.26, coordinates $x\,, y$ are two-dimensional x, y coordinates rotated about the origin $(0, 0)$ by an angle α to match the style used by Galbraith in Figure 5.25. The contours in Figure 5.26 show a continuous improvement towards higher DOFs, which is natural and can be expected. The $p = 3$ simulations on coarse and fine domains agree to a reasonable degree with respect to the shape and magnitude to each other. However, the $p = 3$ fine contours reveal that the core is predicted slightly downstream compared to $p = 3$ coarse results. This is not so obvious, but still visible between the fine and coarse domains at $\alpha = 4°$ in Figure 5.16. The fine domain has double the resolution in the stream-wise direction; thus, it seems that the laminar–turbulent transition and flow reattachment are quite sensitive to the stream-wise resolution. Overall, however, the contours seem to agree to a reasonable degree with respect to the shape, magnitude, and extent with those in the literature.

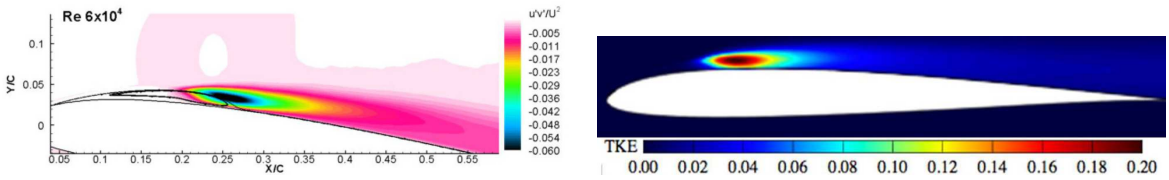

(a): $u\,v\,/U^2$ Galbraith et al. [14] (b): TKE Garmann et al. [16]

Figure 5.25: Reynolds stress ($\overline{u\,v}$) contours at $\alpha = 8°$ taken from Galbraith et al. and Garmann et al. for the purpose of comparison.

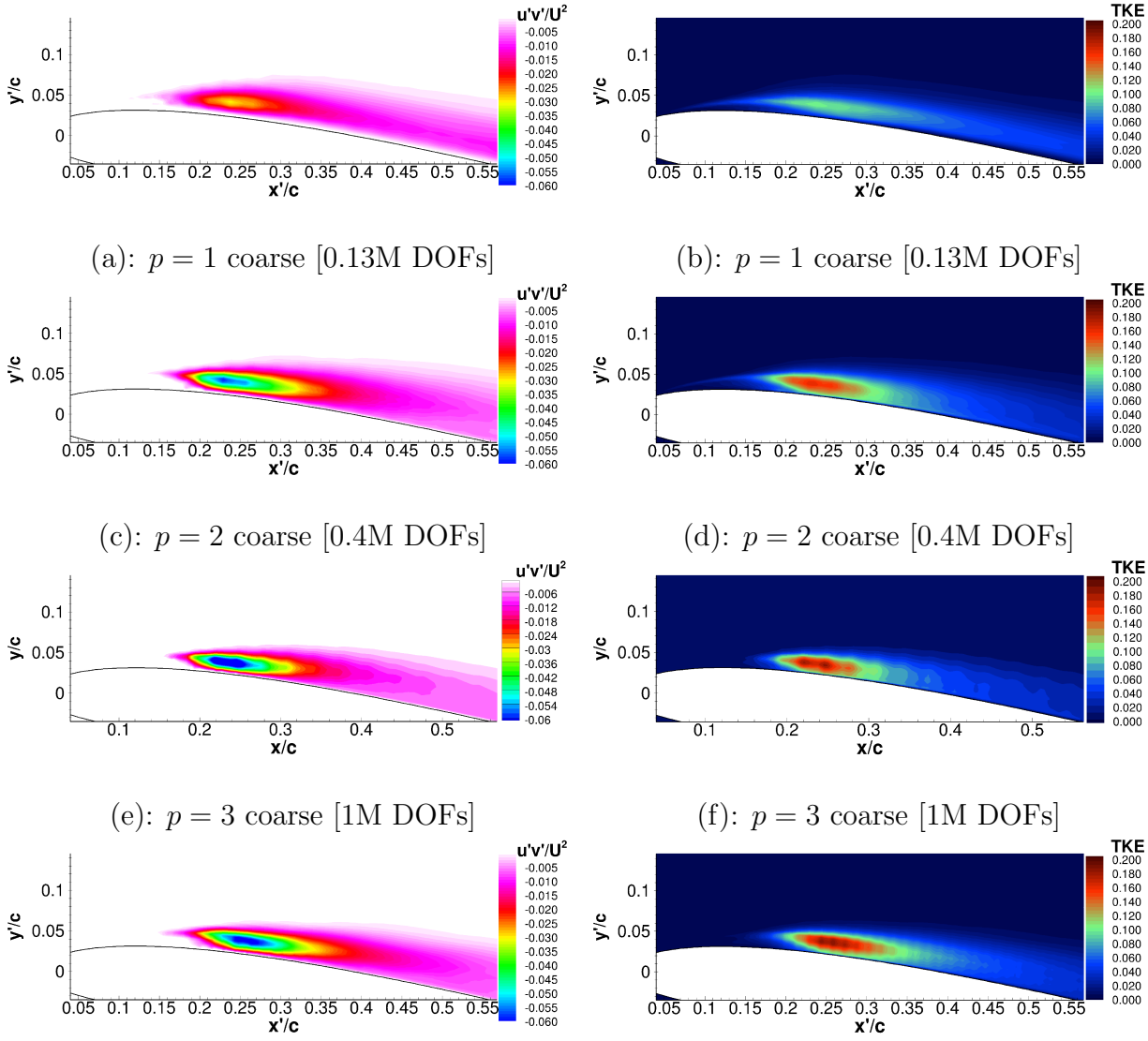

(a): $p = 1$ coarse [0.13M DOFs]

(b): $p = 1$ coarse [0.13M DOFs]

(c): $p = 2$ coarse [0.4M DOFs]

(d): $p = 2$ coarse [0.4M DOFs]

(e): $p = 3$ coarse [1M DOFs]

(f): $p = 3$ coarse [1M DOFs]

(g): $p = 3$ fine [2M DOFs]

(h): $p = 3$ fine [2M DOFs]

Figure 5.26: Reynolds stress ($\overline{u\,v}$) contours and turbulent kinetic energy (TKE) at $\alpha = 8°$. Results are for ILES, $p = 1, 2, 3$ simulations.

5.3.4 Effect of the Polynomial Order on Solution, $\alpha = 4°$

Additional $p = 1, 2, 3$ simulations were conducted on meshes with a comparable distribution and resolution of the solution points in the computational domain. This section discusses the effect of the polynomial order on the solution. Section 5.3.5 compares ILES with traditional subgrid-scale LES, and Section 5.3.6 compares implicit with explicit time stepping. The resolution corresponding to 1 million DOFs is chosen for acceptable results with a reasonable computational cost. Additional simulations were conducted only at $\alpha = 4°$ due to the larger difference between the coarse and fine simulations at $\alpha = 8°$.

Figure 5.27 plots mean C_p and C_f distributions for degree $p = 1, 2, 3$. Figure 5.28 shows instantaneous iso-surfaces of the Q-criterion ($Q = 500$) colored with the Mach number. Figure 5.29 plots contours of the turbulent kinetic energy and Reynolds stress component τ_{xy}. These results illustrate the positive effect of a higher polynomial degree on the under-resolved turbulence as excessive dissipation is associated with the lower polynomial degrees. The second-order ($p = 1$) simulation shows poor performance. The separation and transition point seem to be predicted well, but the $p = 1$ simulation fails in predicting the turbulent reattachment. It seems that as the flow enters into turbulent regime, the two- and three-dimensional instabilities are smoothed out due to the excessive dissipation of the scheme. The breakdown of the span-wise vortex is suppressed, and strong vortices are present further downstream as visible in Figure 5.28c. On the other hand, the third-order ($p = 2$) and fourth-order ($p = 3$) schemes show very similar results. The shrinking difference between the C_f distributions of the $p = 2$ and $p = 3$ simulations in Figure 5.27b indicates the solution tends to converge quickly to some specific value with higher polynomial orders. Despite our effort to present $p = 4$ (fifth-order) simulations for comparison, the $p = 4$ simulations are numerically unstable, which is in accordance with the observed instability of higher-order polynomials for the TGV simulations in Section 4.3.

Figure 5.12a,b compares the mean boundary layer (BL) velocity profiles and mean-squared fluctuations of u-velocity with the literature [102, 109, 116]. The BL profiles are obtained from $p = 1, 2, 3$ simulations on grid with 1 million DOFs at $\alpha = 4°$.

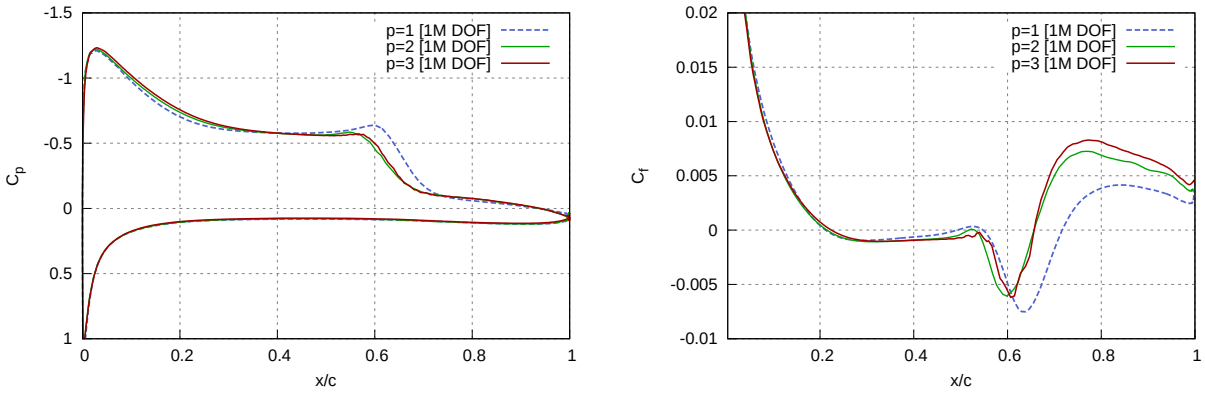

(a): C_p (b): C_f

Figure 5.27: Effect of the polynomial order on C_p and C_f. Meshes have comparable distribution and resolution of the SP. Results are for $\alpha = 4°$, 1M DOFs, $p = 1, 2, 3$ simulations.

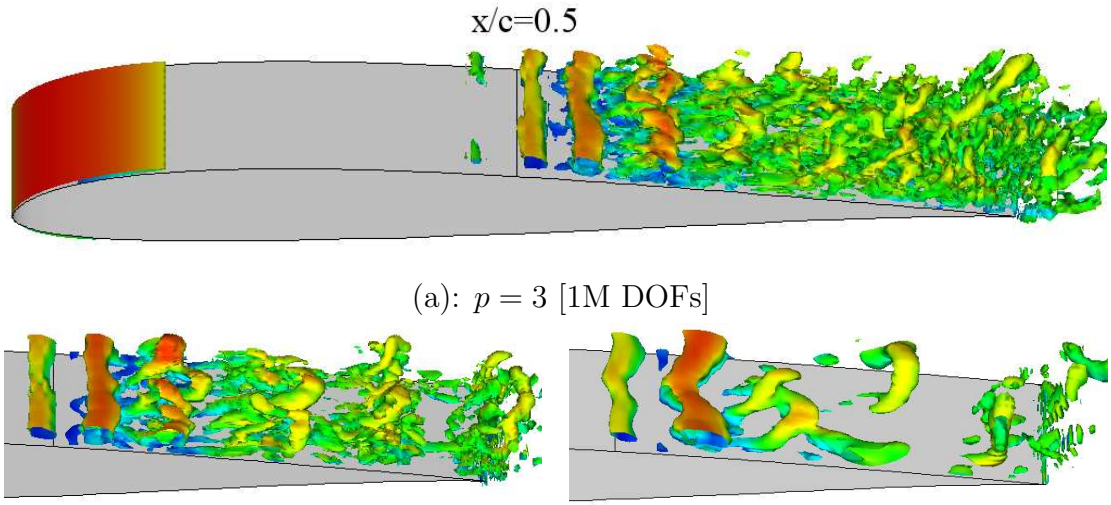

(a): $p = 3$ [1M DOFs]

(b): $p = 2$ [1M DOFs] (c): $p = 1$ [1M DOFs]

Figure 5.28: Instantaneous iso-surfaces of Q-criterion ($Q = 500$) colored with the Mach number. Results are for $\alpha = 4°$, 1M DOFs, $p = 1, 2, 3$ simulations.

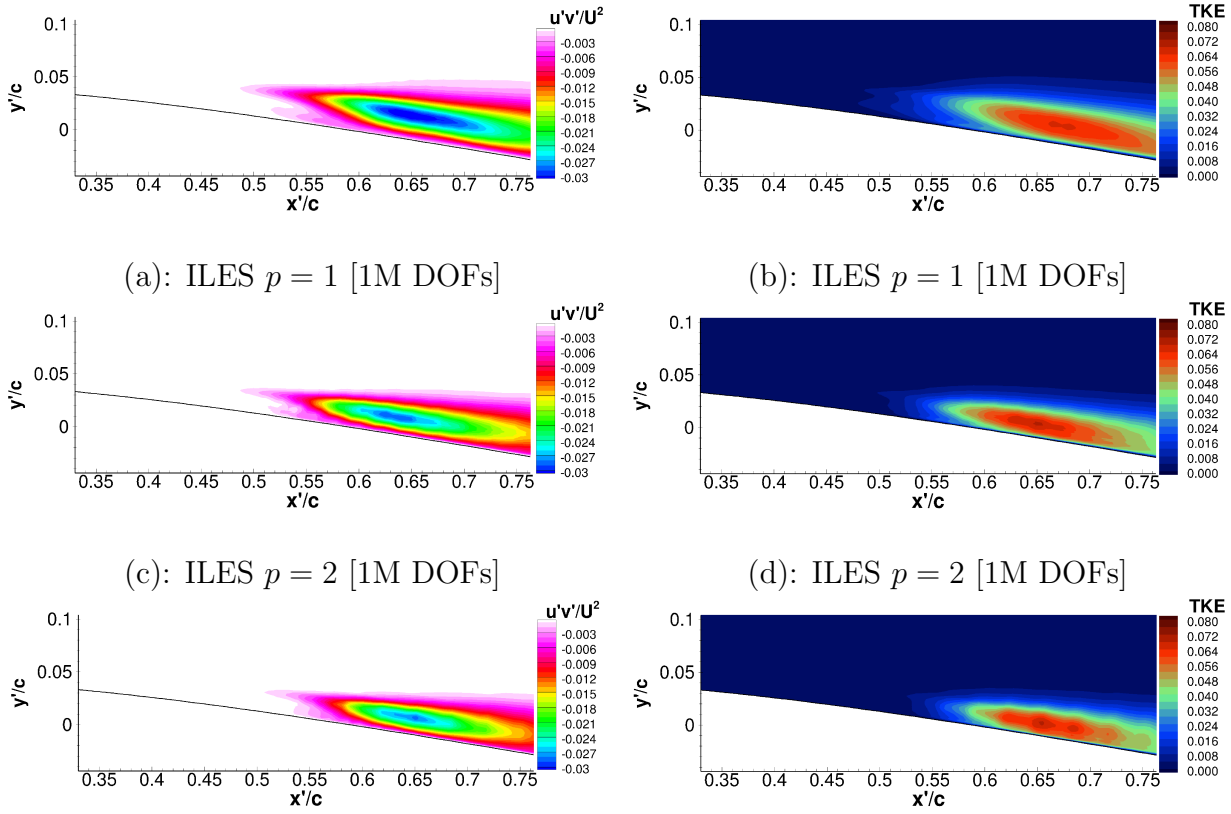

(a): ILES $p = 1$ [1M DOFs]

(b): ILES $p = 1$ [1M DOFs]

(c): ILES $p = 2$ [1M DOFs]

(d): ILES $p = 2$ [1M DOFs]

(e): ILES $p = 3$ [1M DOFs]

(f): ILES $p = 3$ [1M DOFs]

Figure 5.29: Reynolds stress ($\overline{u\,v}$) contours and turbulent kinetic energy (TKE) at $\alpha = 4°$. Results are for ILES, 1M DOFs, $p = 1, 2, 3$ simulations. Coordinates $x\,, y$ are 2D x, y coordinates rotated about the origin $(0, 0)$ by an angle α. Compare with LES in Figure 5.33.

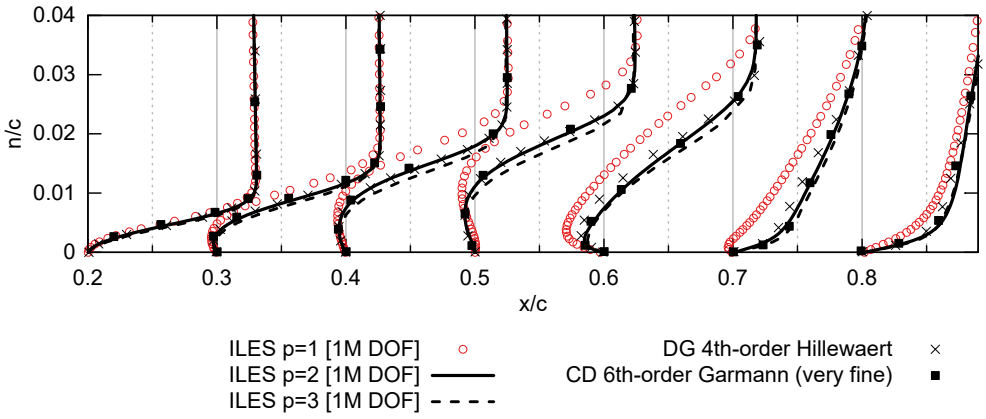

(a): u-velocity at $\alpha = 4°$

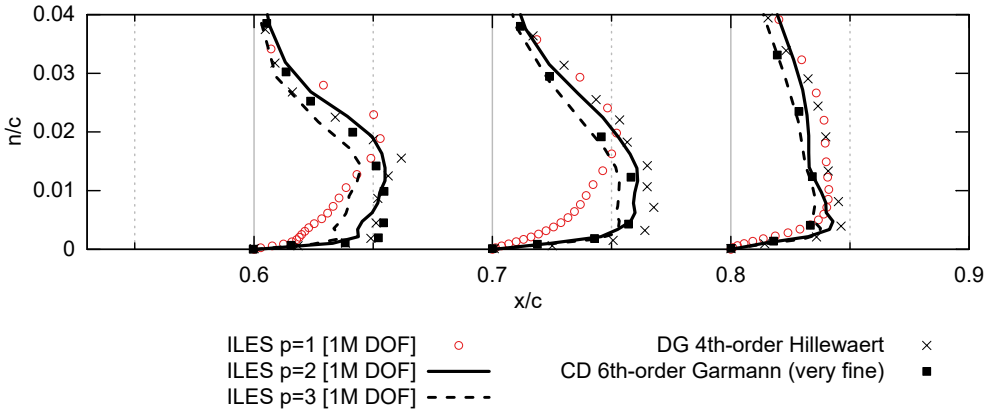

(b): $\overline{u'^2}$ at $\alpha = 4°$

Figure 5.30: Boundary layer profiles of u-velocity and mean-squared fluctuations of u-velocity ($\overline{u'^2}$) obtained from $p = 1, 2, 3$ simulations at $\alpha = 4°$.

5.3.5 Comparison of LES and ILES, $\alpha = 4°$

Since there is only a limited insight into how well the intrinsic numerical dissipation—functioning as an implicit SGS model—in FR behaves for a wider spectrum of flows, the effect of explicit modeling of unresolved scales on the solution is investigated by the LES technique based on an explicit SGS model. The employed SGS model is the wall-adapting local eddy-viscosity (WALE) model as described earlier in Section 3.4. Simulations in the ILES and LES frameworks are conducted for $p = 1, 2, 3$ polynomial orders at $\alpha = 4°$ with the identical computational set-up for LES and ILES, as in Section 5.3.4.

Figure 5.31 plots mean C_p and C_f distributions for degree $p = 1, 2, 3$. Figure 5.32 shows instantaneous iso-surfaces of the Q-criterion ($Q = 500$) colored with the Mach number. Figure 5.33 plots contours of the turbulent kinetic energy and Reynolds stress component τ_{xy}. No significant differences between ILES and LES are clearly visible for the C_p and C_f profiles in Figure 5.31. The three-dimensional vortical structures shown in Figure 5.32 seem likely to be identical to those obtained using the ILES technique shown in Figure 5.28. Like the ILES results, the LES results show the positive effect of a higher polynomial degree on the solution, and it seems that for the flow at these conditions, excessive dissipation of resolved scales—associated with the lower polynomial degrees—has a greater effect than the effects of the unresolved scales.

The contours of the turbulent kinetic energy and Reynolds stress component τ_{xy} obtained using a LES method, shown in Figure 5.33, seem to agree to a reasonable degree with respect to the shape, extent, and magnitude to contours obtained by ILES, shown in Figure 5.29. The boundary layer profiles from the $p = 3$ simulation in Figure 5.34 reveal that explicit subgrid-scale modeling has little effect, and the resulting BL profiles are similar for both approaches.

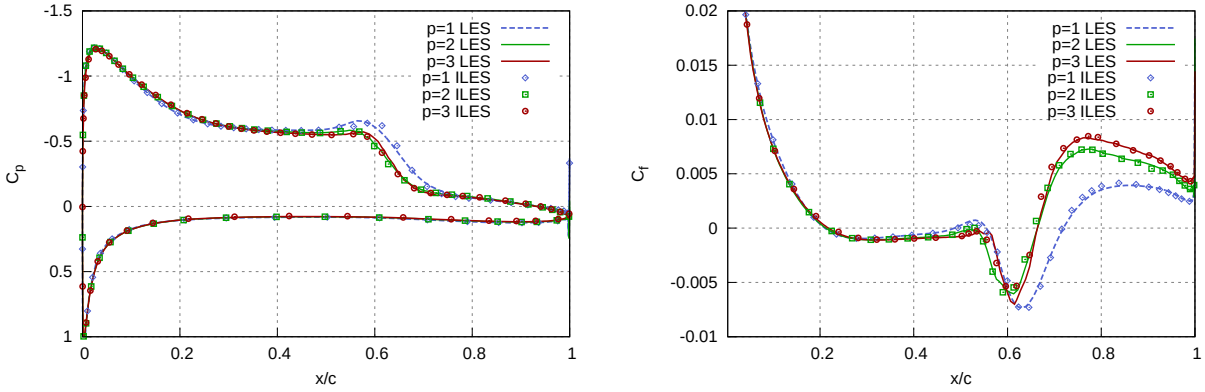

(a): C_p (b): C_f

Figure 5.31: Comparison of ILES and LES approaches shown on C_p and C_f. Meshes have comparable distribution and resolution of the SP. Results are for $\alpha = 4°$, 1M DOFs, $p = 1, 2, 3$ simulations.

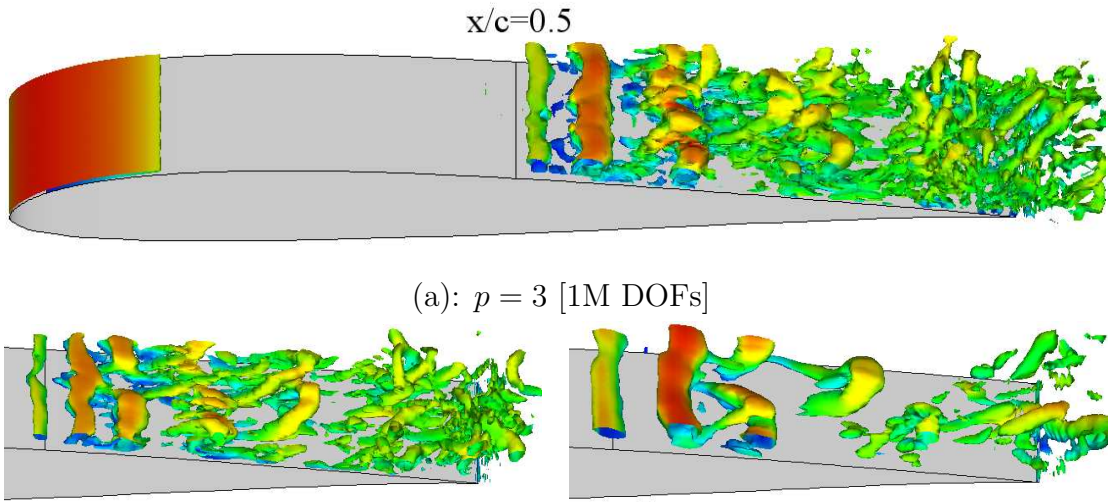

(a): $p = 3$ [1M DOFs]

(b): $p = 2$ [1M DOFs] (c): $p = 1$ [1M DOFs]

Figure 5.32: Instantaneous iso-surfaces of Q-criterion ($Q = 500$) colored with the Mach number. Results are for LES (WALE model), $\alpha = 4°$, 1M DOFs, $p = 1, 2, 3$ simulations. Compare with ILES in Figure 5.28.

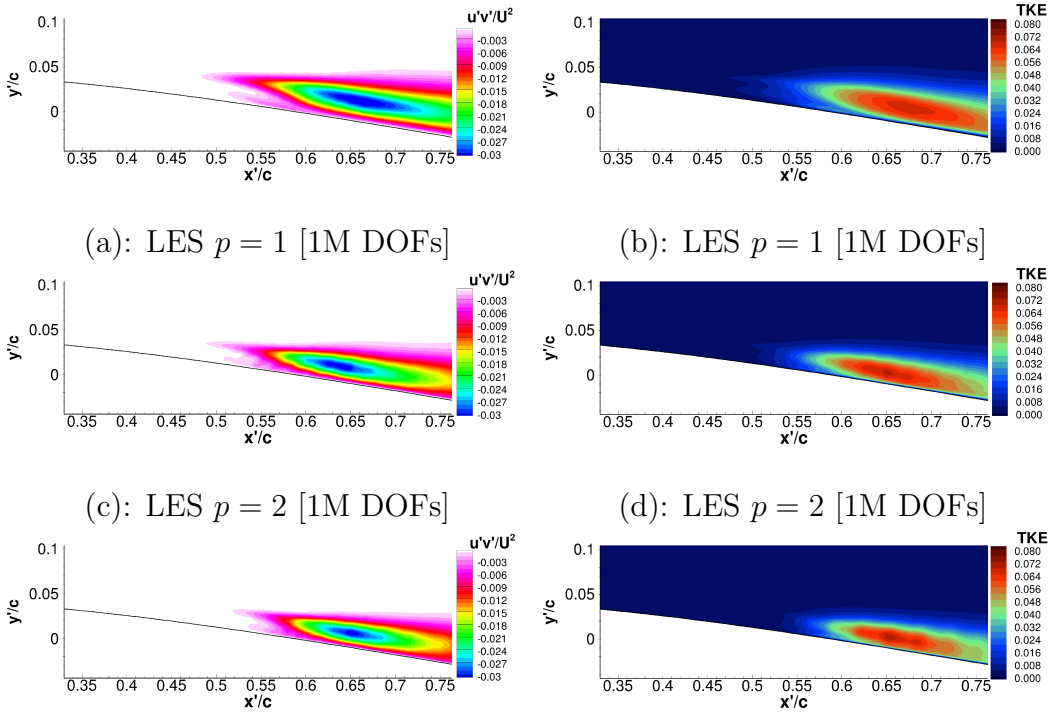

(a): LES $p = 1$ [1M DOFs] (b): LES $p = 1$ [1M DOFs]

(c): LES $p = 2$ [1M DOFs] (d): LES $p = 2$ [1M DOFs]

(e): LES $p = 3$ [1M DOFs] (f): LES $p = 3$ [1M DOFs]

Figure 5.33: Reynolds stress ($\overline{u\,v}$) contours and turbulent kinetic energy (TKE) at $\alpha = 4°$. Results are for LES (WALE model), 1M DOFs, $p = 1, 2, 3$ simulations. Compare with ILES in Figure 5.29.

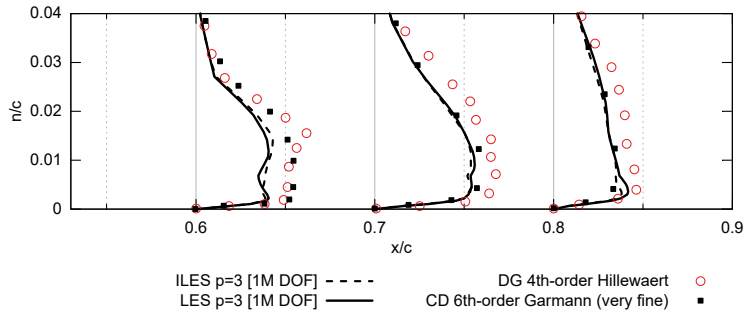

(a): $\overline{u}^2$ at $\alpha = 4°$

Figure 5.34: Boundary layer profiles of mean-squared fluctuations of u-velocity ($\overline{u}^2$) obtained from ILES and LES are compared with the literature at $\alpha = 4°$.

5.3.6 Comparison of time-stepping approaches, $\alpha = 4°$

This section compares results obtained using the implicit second-order accurate-in-time LU-SGS algorithm with the explicit RK3 scheme. Figure 5.35 plots C_p and C_f for $p = 1, 2, 3$ simulations on a grid with 1 million DOFs for both time-stepping schemes. The time step sizes, Courant–Friedrichs–Lewy (CFL) numbers, and CPU cost can be found in Section 5.3.1 in Table 5.2. The second-order accurate LU-SGS scheme seems to produce equivalent flow solutions compared to the results obtained using the third-order explicit approach. Moreover, it seems that an implicit time step of 0.0002 is adequate, without any effects on the computed turbulence. The explicit time step is 2 orders lower than the implicit time step, and the LU-SGS has shown an average calculation speed-up by a factor of 5 while producing results that agree reasonably well. It is noteworthy that the meshes have not been optimized for the best possible performance with explicit schemes. If explicit schemes have a limitation for the maximum allowable time step due to their low stability, they require special care when generating the mesh for compressible wall-bounded flows, where grids are clustered in the viscous boundary layer. We have used a rather fine mesh near the trailing edge and it is responsible for the smaller explicit time steps than those in the literature. The CFL of 0.45 is a reasonable value for an explicit-time integration and our intention was to confirm the equivalent flow solutions and the amount of speed-up for the explicit and implicit methods with our code.

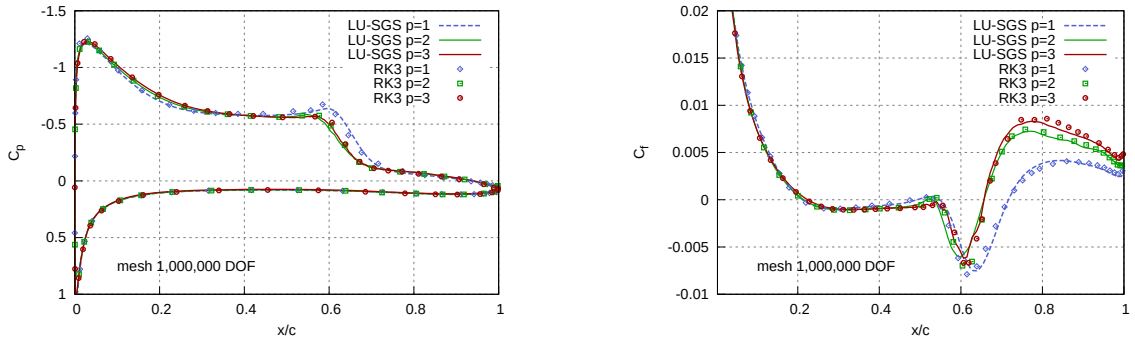

(a): C_p (b): C_f

Figure 5.35: Effect of temporal discretization techniques on C_p and C_f. Results are for $\alpha = 4°$, 1M DOFs, $p = 1, 2, 3$ simulations, second-order LU-SGS and third-order RK3 schemes.

Chapter 6

Conclusions

6.1 Summary

The present thesis contributes to the field of implicit large-eddy simulations (ILESs). The purpose of this research was to examine capabilities of a method developed with a high-order flux reconstruction scheme (FR) for high-fidelity computational fluid dynamics (CFD) simulations of transitional flows at low-Reynolds-numbers.

The method developed with a high-order FR in the ILES framework was applied to two test cases, the compressible Taylor–Green vortex (TGV) problem at a Reynolds number of 1,600, which is a turbulent decaying flow exhibiting homogeneous turbulence, and a low Reynolds number transitional flow over a rectangular infinite SD7003 wing at Reynolds number of 60,000, which represents a realistic aerospace application.

To expand the scope of the present work, a time-accurate implicit lower/upper symmetric Gauss-Seidel solution algorithm for the application of FR to complex unsteady flows was developed. The LU-SGS algorithm was found to produce comparable results to the explicit Runge–Kutta scheme while achieving better computational efficiency. Moreover, several numerical parameters of the LU-SGS scheme were investigated to limit numerical errors and investigate the performance and accuracy of the algorithm. In addition to that, the effects of eddy viscosity on the solution were evaluated and ILES approach validated.

The first case, the compressible TGV problem at $Re = 1{,}600$, was considered for under-resolved to well-resolved scenarios. Low polynomial orders $p = 1, 2$ showed excessive numerical dissipation, which had a significant impact on the accuracy of predictions. On a positive note, the predictions significantly improved as the polynomial order increased. The benefits of the solution approximated by a high-order polynomial were clearly identified. The FR scheme at $p = 4$ with 64^3 degrees of freedom (DOFs) produced quite similar results to $p = 1$ with 192^3 DOFs. The difference of 27 times more DOFs for $p = 1$ has a huge impact on the calculation cost. Despite that low-order schemes were quite inaccurate at low mesh resolutions, they were found stable due to the high numerical dissipation. On the other hand, high-order schemes excelled in accuracy but were unstable, especially at very low mesh resolutions. Medium polynomial orders showed a good balance between accuracy and stability. Furthermore, we found that the TGV simulations without any explicit SGS model outperformed simulations with the SGS turbulence accounted for by the eddy viscosity model. The eddy viscosity sub-grid models are inherently dissipative and our findings are in agreement with those reported in the literature. On the other hand, the added dissipation from the sub-grid scale model seems to have positive effect on the stability of high-order polynomials.

The second case was a transitional flow at low Reynolds number of 60,000 around the SD7003 wing. The flow around the airfoil under this condition is characterized by laminar, transitional, and turbulent flow regions, forming a time-mean laminar-separation bubble (LSB) on the suction side of the SD7003 airfoil. The LSB has noticeable effects-often undesirable-on the airfoil performance. Simulations were carried out at $\alpha = 4^\circ$ and 8°, and $Re = 60{,}000$ with a maximum of 2 million DOFs for the fourth-order ($p = 3$) simulations. Flow solutions were obtained with polynomials of degree $p = 1, 2, 3$, resulting in second-, third-, and fourth-order accurate FR schemes, respectively. Several numerical parameters of the LU-SGS scheme were investigated at $\alpha = 8^\circ$ and $Re = 60{,}000$ to limit numerical errors and highlight performance. The calculation cost with the second-order accurate LU-SGS scheme was about 1.5% higher than the cost with the first-order accurate LU-SGS scheme. The LU-SGS scheme was compared to the explicit Runge–Kutta scheme and the LU-SGS had an average calculation speed-up by a factor of 5 while producing results that agree reasonably well. Simulations on meshes with a constant number of DOFs for polynomial degree $p = 1, 2, 3$ highlighted the positive effect of high-order approximations on the solution. Also, the dissipation added by the sub-grid scale model seemed to have little effect on the solution.

We achieved remarkable agreement with the reference data in the literature, considering that relatively coarse meshes were used in this study. The computed separation, reattachment, and aerodynamic forces (C_L and C_D) agreed reasonably well with many reference data obtained from various high-order schemes using time-accurate explicit/implicit methods.

Based on the results, we can conclude that the developed method with the FR can be a reliable tool of ILES for transitional flows at low Reynolds number flows.

References

[1] G. J. Vachtsevanos and K. P. Valavanis. Military and civilian unmanned aircraft. 2015. Handbook of Unmanned Aerial Vehicles, Springer Netherlands.

[2] B. Abu-Ghannam and R. Shaw. Natural transition of boundary layers- the effect of turbulence, pressure gradient, and flow history. *J. Mech. En. Sci.*, 22(5):213–228, 1980.

[3] J. Slotnick, A. Khodadoust, J. Alonso, D. Darmofal, et al. CFD vision 2030 study: A path to revolutionary computational aeroscience. NASA report NASA/CR–2014-218178, NASA Langley Research Center, Virginia, USA, 2014, http://ntrs.nasa.gov/archive/nasa/casi.ntrs.nasa.gov/20140003093.pdf. Accessed: 2015-12-5.

[4] H. T. Huynh. A flux reconstruction approach to high-order schemes including discontinuous Galerkin methods. *18th AIAA Comput. Fluid Dyn. Conf.*, AIAA 2007-4079, 2007.

[5] H. T. Huynh. A reconstruction approach to high-order schemes including discontinuous Galerkin for diffusion. *47th AIAA Aerosp. Sci. Meeting*, AIAA 2009-403, 2009.

[6] H. T. Huynh. High-order methods including discontinuous Galerkin by reconstructions on triangular meshes. *49th AIAA Aerosp. Sci. Meeting*, AIAA 2011-044, 2011.

[7] J. P. Boris, F. F. Grinstein, E. S. Oran, and R. L. Kolbe. New insights into large eddy simulation. *Fluid Dyn. Res.*, 10:199–228, 1992.

[8] J. Boris. More for les: A brief historical perspective of miles. *ILES: comput. turbul. flow dyn.*, Cambridge University Press, 2007.

[9] J. R. Bull and A. Jameson. Simulation of the Taylor–Green vortex using high-order flux reconstruction schemes. *AIAA J.*, 53(9):2750–2761, 2015.

[10] P. E. Vincent, P. Castonguay, and A. Jameson. A new class of high-order stable flux reconstruction schemes. *J. Sci. Comput.*, 47(1):50–72, 2011.

[11] C. Carton de Wiart and K. Hillewaert. DNS and ILES of transitional flows around a SD7003 using a high-order discontinuous Galerkin method. *7th Int. Conf. Comput. Fluid Dyn.* ICCFD7-3604, 2012.

[12] A. Uranga, P.-O. Persson, M. Drela, et al. Implicit large-eddy simulation of transitional flows over airfoils and wings. *19th AIAA Comput. Fluid Dyn.* AIAA 2009-4131, 2009.

[13] A. D. Beck, T. Bolemann, D. Flad, et al. High-order discontinuous Galerkin spectral element methods for transitional and turbulent flow simulations. *Int. J. Numer. Meth. Fluids*, 76, No. 8, 2014.

[14] M. Galbraith. Implicit large-eddy simulation of low-reynolds-number transitional flow past the SD7003 airfoil. master's thesis, University of Cincinnati, 2009.

[15] M. Galbraith and M. R. Visbal. Implicit large-eddy simulation of low-reynolds-number flow past the SD7003 airfoil. *40th AIAA Fluid Dyn. Conf.* AIAA 2010-4737, 2010.

[16] D. J. Garmann, M. R. Visbal, and P. D. Orkwis. Comparative study of implicit and subgrid-scale model large-eddy simulation techniques for low-reynolds number airfoil applications. *Int. J. Numer. Meth. Fluids*, 71, No. 12, 2012.

[17] A. Uranga. Investigation of transition to turbulence at low reynolds numbers using implicit large-eddy simulations with a discontinuous Galerkin method. Phd thesis, M.I.T, 2011.

[18] Y. Zhou and Z. J. Wang. Implicit large-eddy simulation of transitional flow over a SD7003 wing using high-order spectral difference method. *40th AIAA Fluid Dyn. Conf.* AIAA 2010-4442, 2010.

[19] P. Castonguay, C. Liang, and A. Jameson. Simulation of transitional flow over airfoils using the spectral difference method. *40th Fluid Dyn. Conf.* AIAA 2010-4626, 2010.

[20] J. Smagorinsky. General circulation experiments with the primitive equations. *Month. Weath. Rev.*, 93(3):99–164, 1963.

[21] D. K. Lilly. The representation of small-scale turbulence in numerical simulation experiments. *Proceed. IBM Scient. Comput Symp. Envi. Sci.*, Yorktown Heights, USA, 1967.

[22] J. Deardorff. A numerical study of three-dimensional turbulent channel flow at large Reynolds numbers. *J. Fluid Mech.*, 41:453–480, 1970.

[23] U. Schumann. Subgrid-scale model for finite difference simulation of turbulent flows in plane channels and annuli. *J. Comput. Phys.*, 18(4):376–404, 1975.

[24] H. Tinoco, H. Lindqvist, and W. Frid. Numerical simulation of industrial flows, numerical simulations – examples and applications in computational fluid dynamics. In: Lutz Angermann, editor, ISBN: 978-953-307-153-4, InTech, 2010, http://www.intechopen.com/books/numerical-simulations-examples-and-applications-in-computational-fluid\-dynamics/numerical-simulation-ofindustrial-flows. Accessed: 2014-7-9.

[25] A.G. Hutton. The emerging role of large eddy simulation in industrial practice: challenges and opportunities. *Philos. Trans. A. Math. Phys. Eng. Sci.*, 367(1899), 2009.

[26] U Piomelli. Large eddy simulations in 2030 and beyond. *Philos. Trans. A. Math. Phys. Eng. Sci.*, 372(2022), 2014.

[27] P. Sagaut. *Large-eddy simulation for incompressible flows.* Springer, 3rd edition, 2006.

[28] C. A. Kennedy and M. H. Carpenter. Several new numerical-methods for compressible shear-layer simulations. *Appl. Numer. Math.*, 14(397), 1994.

[29] O. V. Vasilyev, T. S. Lund, and P. Moin. A general class of commutative filters for LES in complex geometries. *J. Comput. Phys.*, 146:82–104, 1998.

[30] U. Piomelli. Large-eddy simulation: achievements and challenges. *Prog. Aeros. Sc.*, 35:335–362, 1999.

[31] M. Lesieur and O. Metais. New trends in large eddy simulations of turbulence. *Annu. Rev. Fluid Mech.*, 28(1):45–82, 1996.

[32] M. Lesieur and O. Metais. One-equation sub-grid scale model using dynamic procedure for the energy production. *J. Appl. Mech.*, 73(3):368–373, 1996.

[33] I. Veloudis, Z. Yang, and J.J McGuirk. Les of wall-bounded flows using a new subgrid scale model based on energy spectrum dissipation. *J. Appl. Mech.*, 75(2), 2008.

[34] S. B. Pope. *Turbulent flows*. Cambridge University Press, 1st edition, 2000.

[35] J. Boussinesq. Essai sur la théorie des eaux courantes. *Acad. Sci. Paris*, 26, 1877.

[36] J. P. Boris. On large eddy simulation using subgrid turbulence models. *In: Lumley, J., editor, Whither turbulence? Turbulence at the crossroads*, pages 344–353, Springer-Verlag, 1992.

[37] Z. J. Wang, K. Fidkowski, R. Abgrall, et al. High-order CFD methods: current status and perspective. *Int. J. Numer. Meth. Fluids*, 72(8):811–845, 2013.

[38] Z. J. Wang. High-order methods for the Euler and Navier–Stokes equations on unstructured grids. *Prog. Aerosp. Sci.*, 43, No. 1:1–41, 2007.

[39] C. Wagner, T. Huttl, and P. Sagaut. Large-eddy simulation for acoustics. 20, Cambridge University Press, 2007.

[40] S. K. Lele. Compact finite difference schemes with spectral-like resolution. *J. Comput. Phys.*, 103:16–42, 1992.

[41] J. W. Kim and D. J. Lee. Optimized compact finite difference schemes with maximum resolution. *AIAA J.*, 34:887–893, 1996.

[42] A. Harten, B. Engquist, S. Osher, and S.R. Chakravarthy. Uniformly high order accurate essentially non-oscillatory schemes. *J. Comput. Phys.*, 71:231–303, 1987.

[43] C. W. Shu and S. Osher. Efficient implementation of essentially non-oscillatory shock capturing schemes. *J. Comput. Phys.*, 77:439–471, 1988.

[44] C. W. Shu and S. Osher. Efficient implementation of essentially non-oscillatory shock capturing schemes. *J. Comput. Phys.*, 83:32–78, 1989.

[45] X.D. Liu, S. Osher, and T. Chan. Weighted essentially non-oscillatory schemes. *J. Comput. Phys.*, 115:200–212, 1994.

[46] W. H. Reed and T. R. Hill. Triangular mesh methods for the neutron transport equation. *Proceedings of the ANS*. Los Alamos research report LA-UR-73-479, 1973.

[47] B. Cockburn, G. E. Karniadakis, and C. W. Shu. The development of discontinuous Galerkin methods. *Lecture Notes Comput. Sci. Eng.*, 11:3–50, Springer Berlin Heidelberg, 2000.

[48] J. S. Hesthaven and T. Warburton. *Nodal discontinuous Galerkin methods*. Texts Appl. Math., Vol. 54, Springer-Verlag New York, 2008.

[49] D. A. Kopriva and J. H. Kolias. A conservative staggered-grid Chebyshev multidomain method for compressible flows. *J. Comput. Phys.*, 125:244–261, 1996.

[50] Y. Liu, M. Vinokur, and Z. J. Wang. Multi-dimensional spectral difference method for unstructured grids. *43rd AIAA Aerosp. Sci. Meeting*. AIAA 2005-0320, 2005.

[51] Y. Liu, M. Vinokur, and Z. J. Wang. Spectral difference method for unstructured grids i: basic formulation. In *J. Comput. Phys.*, volume 216, pages 780–801. 2006.

[52] Z. J. Wang. High-order computational fluid dynamics tools for aircraft design. *Phil. Trans. R. Soc. A*, 372, Iss. 2022, 2014.

[53] H. T. Huynh, Z. J. Wang, and P. E. Vincent. High-order methods for computational fluid dynamics: a brief review of compact differential formulations on unstructured grids. *Comput. Fluids*, 98, 2014.

[54] A. Jameson. Advances in bringing high-order methods to practical applications in computational fluid dynamics. *20th AIAA CFD Conf.* AIAA 2011-3226, 2011.

[55] M. Gaster. The structure and behaviour of laminar separation bubbles. Reports and Memoranda No. 3595, Aerodyn. Divison N.P.P., London, UK, 1967.

[56] W. Shyy, Y. Lian, T. Jian, D. Viieru, and H. Liu. Aerodynamics of low Reynolds number flyers. 2008. Cambridge University Press.

[57] W. Sutherland. The viscosity of gases and molecular force. *Phil. Mag.*, 5(36):507–531, 1893.

[58] H. Gao, Z. J. Wang, and H. T. Huynh. Differential formulation of discontinuous Galerkin and related methods for the Navier–Stokes equations. *Comm. Comput. Phys.*, 13(4):1013–1044, 2013.

[59] K. Miyaji. On the compressible flow simulations with shocks by a flux reconstruction approach. *20th AIAA Comput. Fluid Dyn. Conf.*, AIAA 2011-3057, 2011.

[60] T. Haga, K. Kuzuu, R. Takaki, and E. Shima. Development of a high-order flux reconstruction scheme for body-fitted Cartesian unstructured grids. *51st AIAA Aerosp. Sci. Meeting*, AIAA 2013-0409, 2013.

[61] K. Miyaji. Vortical flow simulations by a high-order accurate unstructured hexahedral grid method. *Comput. Fluids*, 85:78–84, 2012.

[62] C. Liang, C. Cox, and M. Plesniak. A comparison of computational efficiencies of spectral difference method and correction procedure via reconstruction. *J. Comput. Phys.*, 239:138–146, 2013.

[63] B. C. Vermeire, J. S. Cagnone, and S. Nadarajah. ILES using the correction procedure via reconstruction scheme. *51st AIAA Aerosp. Sci. Meeting.* AIAA 2013-1001, 2013.

[64] B. C. Vermeire, S. Nadarajah, and P. G. Tucker. Canonical test cases for high-order unstructured implicit large-eddy simulation. *52nd AIAA Aerosp. Sci. Meeting.* AIAA 2014-0935, 2014.

[65] Y. Lu, WN. Dawes, and X. Yuan. Investigation of 3D internal flow using new flux reconstruction high order method. *ASME Turbo Expo 2012*, ASME GT2012-69270, 2012.

[66] Y. Lu, K. Liu, and WN. Dawes. Large-eddy simulations for 3D turbine blades using a high order flux reconstruction method. *ASME Turbo Expo 2013*, ASME GT2013-94707, 2013.

[67] V. Skarolek and K. Miyaji. Transitional flow over a SD7003 wing using flux reconstruction scheme. *52nd AIAA Aerosp. Sci. Meeting.* AIAA 2014-0250, 2014.

[68] D. De Grazia et al. Connections between the discontinuous Galerkin method and high-order flux reconstruction schemes. *Int. J. Numer. Meth. Fluids*, 75, No. 12:860–877, 2014.

[69] M. Yu, Z. J. Wang, and Y. Liu. On the accuracy and efficiency of discontinuous Galerkin, spectral difference and correction procedure via reconstruction methods. *J. Comput. Phys.*, 259:70–95, 2014.

[70] J. R. Bull and A. Jameson. Simulation of the compressible Taylor–Green vortex using high-order flux reconstruction schemes. *7th AIAA Theor. Fluid Mech. Conf.* AIAA 2014-3210, 2014.

[71] J. R. Bull and A. Jameson. High-order flux reconstruction schemes for LES on tetrahedral meshes. *Notes on Num. Fluid Mech. Mult. Design*, 130:69–79, 2015. In: Progress in hybrid RANS-LES modelling, Elsevier, DOI: 978-3-319-15141-0.

[72] K. Asthana and A. Jameson. High-order flux reconstruction schemes with minimal dispersion and dissipation. *J. Sci. Comput.*, 62(3):913–944, 2015.

[73] S.C. Spiegel, H.T. Huynh, and J.R. DeBonis. De-aliasing through over-integration applied to the flux reconstruction and discontinuous Galerkin methods. *22nd AIAA Comput. Fluid Dyn. Conf.*, AIAA 2015-2744, 2015.

[74] S.C. Spiegel, H.T. Huynh, and J.R. DeBonis. A survey of the isentropic Euler vortex problem using high-order methods. *22nd AIAA Comput. Fluid Dyn. Conf.*, AIAA 2015-2444, 2015.

[75] V. V. Rusanov. Calculation of interaction of non-steady shock waves with obstacles. *J. Comput. Math Phys. USSR*, 1:261–279, 1961.

[76] F. Bassi and S. Rebay. A high-order accurate discontinuous finite element method for the numerical solution of the compressible Navier-Stokes equations. *J. Comput. Phys.*, 131:267–279, 1997.

[77] C.-W. Shu and S. Osher. Efficient implementation of essentially non-oscillatory shock-capturing schemes. *J. Comput. Phys.*, 77:439–471, 1988.

[78] Y. Sun, Z. J. Wang, and Y. Liu. Efficient implicit non-linear LU-SGS approach for compressible flow computation using high-order spectral difference method. *Comm. Comput. Phys.*, 5(2-4):760–778, 2009.

[79] G. Wang, Y. Jiang, and Z. Ye. An improved LU-SGS implicit scheme for high Reynolds number flow computations on hybrid unstructured mesh. *Chin. J. Aeronaut.*, 25:33–41, 2012.

[80] K. Kitamura, E. Shima, K. Fujimoto, and Z. J. Wang. Performance of low-dissipation Euler fluxes and preconditioned LU-SGS at low speeds. *Comm. Comput. Phys.*, 10:90–119, 2011.

[81] M. Parsani, G. Ghorbaniasl, C. Lacor, and E. Turkel. An implicit high-order spectral difference approach for large-eddy simulation. *J. Comput. Phys.*, 229(14):5373–5393, 2010.

[82] R. Kannan. An implicit LU-SGS spectral volume method for the moment models in device simulations: formulation in 1D and application to a p-multigrid algorithm. *Int. J. Numer. Methods Biomed. Eng.*, 27(9):1362–1375, 2013.

[83] F. Nicoud and F. Ducros. Subgrid-scale stress modelling based on the square of the velocity gradient tensor. *Flow, Turb. Comb.*, 62(3):183–200, 1999.

[84] M. Garmano, U. Piomelli, P. Moin, and W. H. Cabot. A dynamic subgrid-scale eddy viscosity model. *Phys. Fluids*, 3(7):1760–1765, 1991.

[85] L. Berselli, T. Iliescu, and W. J. Layton. *Mathematics of large-eddy simulation of turbulent flows*. Springer-Verlag Berlin Heidelberg, 1st edition, 2006.

[86] G. Lodato, P. Castonguay, and A. Jameson. Discrete filter operators for large-eddy simulation using high-order spectral difference methods. *Int. J. Numer. Meth. Fluids*, 72:231–258, 2012.

[87] G. Erlebacher, M.Y. Hussaini, C.G. Speziale, and T.A. Zang. Toward the large-eddy simulation of compressible turbulent flows. *J. Fluid Mech.*, 238:155–185, 1992.

[88] C.G. Speziale, G. Erlebacher, T.A. Zang, and M.Y. Hussaini. The subgrid-scale modeling of compressible turbulence. *Phys. Fluids*, 31(4):940–942, 1988.

[89] C. Fureby and G. Tabor. Mathematical and physical constraints on large-eddy simulations. *Theoret. Comput. Fluid Dyn.*, 9:85–102, 1997.

[90] J. Dongarra et al. MPI - a message-passing interface standard. *Int. J. Supercomput. Ap.*, 8, No. 3-4:165–416, 1994.

[91] G. Karypis and V. Kumar. METIS - Unstructured graph partitioning and sparse matrix ordering system, version 2.0. *Technical report*, 1995.

[92] M. E. Brachet. Direct simulation of three-dimensional turbulence in the Taylor-Green vortex. *Fluid. Dyn. Res.*, 8:1–8, 1991.

[93] W. M. van Rees, A. Leonard, D. I. Pullin, and P. Koumoutsakos. A comparison of vortex and pseudo-spectral methods for the simulation of periodic vortical flows at high Reynolds numbers. *J. Comput. Phys.*, 230:2794–2805, 2011.

[94] C. Carton de Wiart, K. Hillewaert, M. Duponcheel, and G. Winckelmans. Assessment of a discontinuous Galerkin method for the simulation of vortical flows at high Reynolds number. *Int. J. Numer. Meth. Fluids*, 74(7):469–493, 2013.

[95] A. D. Beck and G. J. Gassner. Numerical simulation of the Taylor–Green vortex at $Re = 1600$ with the discontinuous Galerkin spectral element method for well-resolved and underresolved scenarios. In: 1st International workshop on high-order CFD methods, Nashville, TN, USA, 2012, http://dept.ku.edu/~cfdku/hiocfd/abstracts/C35_Stuttgart.pdf. Accessed: 2014-11-4.

[96] G. J. Gassner and A. D. Beck. On the accuracy of high-order discretizations for underresolved turbulence simulations. *Theor. Comput. Fluid Dyn.*, 27:221–237, 2013.

[97] J. R. DeBonis. Solutions of the Taylor–Green vortex problem using high-resolution explicit finite difference methods. *NASA Glenn Research Center, NASA/TM—2013-217850*, 2013. Prepared for the 51st Aerospace Sciences Meeting sponsored by the American Institute of Aeronautics and Astronautics, Grapevine, Texas, January 7–10, 2013.

[98] T. Haga and Z. J. Wang. Simulation of the Taylor–Green vortex at $Re = 1600$ using the CPR method. In: 1st International workshop on high-order CFD methods,

Nashville, TN, USA, 2012, http://dept.ku.edu/~cfdku/hiocfd/abstracts/C35_ISU.pdf. Accessed: 2015-2-2.

[99] C-W. Shu, W-S. Don, D. Gottlieb, O. Schilling, and L. Jameson. Numerical convergence study of nearly incompressible, inviscid Taylor–Green vortex flow. *J. Sci. Comput.*, 24(1):1–27, 2005.

[100] J. Jeong and F. Hussain. On the identification of a vortex. *J. Fluid Mech.*, 285:69–94, 1995.

[101] M. Lesieur, O. Métais, and P. Comte. *Large-eddy simulations of turbulence*. Cambridge University Press, 1st edition, 2005.

[102] M. R. Visbal. Case 3.3 Summary: transitional flow over the SD7003 airfoil. In: 1st International workshop on high-order CFD methods, Nashville, Tennessee, 2012, http://dept.ku.edu/~cfdku/hiocfd/summary/C3.3_summary.pptx. Accessed: 2014-10-15.

[103] F. Bassi, L. Botti, A. Colombo, et al. Linearly implicit Rosenbrock-type Runge–Kutta schemes applied to the discontinuous Galerkin solution of compressible and incompressible unsteady flows. *Comput. Fluids*, 118:305–320, 2015.

[104] P. D. Boom and D. W. Zingg. Time-accurate flow simulations using an efficient Newton–Krylov–Schur approach with high-order temporal and spatial discretization. *51st AIAA Aerosp. Sci. Meeting*. AIAA 2013-0383, 2013.

[105] E. Weide, G. Giangaspero, and M. Svärd. Efficiency benchmarking of an energy stable high-order finite difference discretization. *AIAA J.*, 53, No. 7:1845–1860, 2015.

[106] P. Catalano and R. Tognaccini. Numerical analysis of the flow around the SD7003 airfoil. *48th AIAA Aero. Sci. Meeting*. AIAA 2010-68, 2010.

[107] P. Catalano and R. Tognaccini. Influence of free-stream turbulence on simulations of laminar separation bubbles. *47th AIAA Aero. Sci. Meeting*. AIAA 2009-1471, 2009.

[108] P. Catalano and R. Tognaccini. Turbulence modelling for low Reynolds number flows. *AIAA J.*, 48(8):1673–1685, 2010.

[109] D. J. Garmann and M. R. Visbal. Implicit large-eddy simulations of transitional flow over the SD7003 airfoil using compact finite differencing and filtering. In: 2nd International workshop on high-order CFD methods, Cologne, Germany, 2013, http://www.dlr.de/as/Portaldata/5/Resources/dokumente/veranstaltungen/2013_05-hiocfd/contrib/C33_Garmann.pdf. Accessed: 2015-09-5.

[110] B. C. Vermeire and S. Nadarajah. Adaptive IMEX schemes for high-order unstructured methods. *J. Comput. Phys.*, 280:261–286, 2015.

[111] H. Choi and P. Moin. Effects of the computational time step on numerical solutions of turbulent flow. *J. Comput. Phys.*, 113(1):1–4, 1994.

[112] M. S. Selig, J. Donovan, and D. Fraser. Airfoils at low speed. 8, SoarTech Publications, 1989.

[113] M. S. Selig, J. J. Guglielmo, A. P. Broeren, et al. Summary of low-speed airfoil data. 1, SoarTech Publications, 1995.

[114] R. E. Radespiel, J. Windte, and U. Scholz. Numerical and experimental flow analysis of moving airfoils with laminar separation bubbles. *44th AIAA Aerosp. Sci. Meeting.* AIAA 2006-501, 2006.

[115] M. V. Ol, B. R. McAuliffe, E. S. Hanff, et al. Comparison of laminar separation bubbles measurements on a low reynolds number airfoil in three facilities. *35th AIAA Fluid Dyn. Conf.* AIAA 2005-5149, 2005.

[116] K. Hillewaert. Transitional flow over a SD7003 wing. In: 1st International workshop on high-order CFD methods, Nashville, Tennessee, 2012, http://dept.ku.edu/~cfdku/hiocfd/abstracts/C33_cenaero.pdf. Accessed: 2014-10-15.

[117] H. Frank, A. Beck, T. Bolemann, et al. High-order simulation of transitional flow over the SD7003 airfoil with the discontinuous Galerkin spectral element method. In: 2nd International workshop on high-order CFD methods, Koln, Germany, 2013, http://nrg.iag.uni-stuttgart.de/wp-content/uploads/2014/01/2013_05_28_HOWorkshop.pdf. Accessed: 2014-10-15.